

Tracer Populations in the Local Group

This dissertation is submitted for the degree of

Doctor of Philosophy

by

Laura Louise Watkins

Institute of Astronomy
& Gonville and Caius College

University of Cambridge



31st January 2011

*For Mum and Dad,
who gave me wings so I could fly
and a nest to come home to*

Contents

Declaration	ix
Acknowledgments	xi
Summary	xiii
1 Introduction	1
1.1 Structure formation	3
1.1.1 Dark matter	3
1.1.2 Overview of current structure formation theory	4
1.1.3 Overmerging and the missing satellite problem	6
1.1.4 Dominance and survivability of structure	7
1.2 The Milky Way	8
1.2.1 The bulge	8
1.2.2 The thin disk	9
1.2.3 The thick disk	10
1.2.4 The halo	11
1.3 The Andromeda galaxy	18
1.4 Dwarf spheroidal galaxies	22
1.4.1 Milky Way dwarfs	22
1.4.2 M31 dwarfs	23
1.4.3 Comparison with star clusters	24
1.4.4 Dwarf properties	26
1.5 Tracer Populations in the Local Group	28
2 Variable stars in SDSS Stripe 82	31
2.1 The Sloan Digital Sky Survey	32
2.1.1 SDSS Stripe 82	34
2.2 Variable Stars in Stripe 82	35
2.2.1 Variable Selection	35
2.2.2 Variable Properties	37
2.2.3 The Proper Motions	38
2.3 Comparison with other variability surveys in Stripe 82	39
2.4 Summary	40

3	Substructure revealed by RR Lyraes in SDSS Stripe 82	43
3.1	Overview of RR Lyraes	43
3.2	Selection of the RR Lyrae sample	45
3.2.1	Identification of RR Lyraes	45
3.2.2	RR Lyrae Periods	46
3.2.3	RR Lyrae Classification	48
3.2.4	The R Rab types	50
3.2.5	The R Rc types	51
3.3	Substructure revealed by the RR Lyraes	52
3.3.1	RR Lyrae Distances	52
3.3.2	The Sagittarius Stream, the Hercules-Aquila Cloud and the Pisces Overdensity	53
3.4	Summary	60
4	Masses of the Milky Way and Andromeda Galaxies	63
4.1	Mass estimators	64
4.1.1	Tracer Mass Estimator	65
4.1.2	A Family of Estimators	68
4.2	Checks with Monte Carlo Simulations	70
4.3	Mass Estimates for Andromeda and the Milky Way	72
4.3.1	Choice of Power-Law Index Parameters	72
4.3.2	Radial Velocity Datasets	75
4.3.3	Simultaneous Solution for Mass and Anisotropy	81
4.3.4	Radial and Proper Motion Datasets	82
4.4	Discussion	85
4.5	Summary	86
5	Application of the Timing Argument to host-satellite systems	89
5.1	Timing Argument	91
5.2	The Data	93
5.3	M31 mass and orbit parameters	94
5.3.1	M31 - And XII orbit	94
5.3.2	M31 - And XIV orbit	97
5.4	Modelling	98
5.5	The Milky Way	102
5.5.1	MW - Leo I orbit	102
5.6	Discussion	103
6	Discussion & Conclusions	107
6.1	Chapter Summaries	107
6.1.1	Variable stars in SDSS Stripe 82	107
6.1.2	Substructure revealed by RR Lyraes in SDSS Stripe 82	108
6.1.3	Masses of the Milky Way and Andromeda Galaxies	109
6.1.4	Application of the Timing Argument to host-satellite systems	111

6.2	Prospects for the Future	112
6.2.1	The Pisces Overdensity	112
6.2.2	Surveys	113
A	Coordinate and velocity calculations	117
A.1	Converting from equatorial to Galactic coordinates	117
A.2	Galactocentric spatial velocities	118
A.3	M31-centric spatial velocities	119
	Bibliography	131
	Nomenclature	134
	List of tables	135
	List of figures	138

Declaration

I hereby declare that my thesis entitled *Tracer Populations in the Local Group* is not substantially the same as any that I have submitted for a degree or diploma or other qualification at any other University. I further state that no part of my thesis has already been or is being concurrently submitted for any such degree, diploma or other qualification. This dissertation is the result of my own work and includes nothing which is the outcome of work done in collaboration except where specifically indicated in the text. Those parts of this thesis which have been published or accepted for publication are as follows:

- The work presented in Chapters 2 and 3 has been completed in collaboration with N. W. Evans and V. Belokurov and is published as: Watkins, L.L. et al (2009) 'Substructure revealed by RR Lyraes in SDSS Stripe 82', *Monthly Notices of the Royal Astronomical Society*, **398**, 1757-1770.
- The work presented in Chapter 4 has been completed in collaboration with N. W. Evans and J. An and is published as: Watkins, L.L., Evans, N.W. & An, J. (2010) 'The masses of the Milky Way and the Andromeda galaxies', *Monthly Notices of the Royal Astronomical Society*, **406**, 264-278.

This thesis contains fewer than 60,000 words.

Laura L. Watkins

Cambridge, 31st January 2011

Acknowledgments

There are so many people to whom I owe my thanks.

Firstly, to my supervisors, Wyn Evans and Vasily Belokurov for their support, guidance and patience throughout the course of my PhD - I could not have done any of this without them.

To Helen and Sarah, for being the best flatmates I could ever have hoped for.

To Martin, for sharing an office with me for four years and for keeping me company in the burrito queue. And to Richard, Berkeley, Sarah, Marcus, Shoko and Richard: for their friendship, their company over coffee and numerous pub trips and for making my time at the IoA so special.

To everyone in the CDC for giving me the opportunity to dance; especially everyone in CUDT who made my final year so fantastic. And most of all, thank you, Ben, for dancing with me.

To Tash, my best friend, for always being there.

And last, but my no means least, I would like to thank my family; their unfailing love and support has put me where I am today and I would be nothing without them.

Laura L. Watkins

Cambridge, 31st January 2011

Summary

Tracer Populations in the Local Group

Laura L. Watkins

So often in astronomy, an object is not considered for its individual merits, but for what we may learn from its properties regarding some larger population. The existence of dark matter is a prime example of this; we cannot see it directly but we can infer its presence by noting its effects on the stars orbiting within its potential. This thesis describes how various sets of tracer populations can be used to probe the properties of a variety of galaxies in the Local Group.

I begin by describing the extraction of a variable catalogue from the Sloan Digital Sky Survey Stripe 82 dataset and then use the catalogue to select a high-quality set of RR Lyrae stars. Analysing the distribution of the RR Lyraes reveals three significant substructures in the Milky Way halo: the Hercules-Aquila Cloud and the Sagittarius Stream, which were already known to exist, and the Pisces Overdensity, which was previously undetected. It is a faint, extended structure found at ~ 80 kpc and is of unknown origin. Altogether, I find that nearly 80% of the RR Lyraes are associated with substructures, consistent with the theory that galaxy halos are predominantly, or even entirely, made up from disrupted satellites. I also investigate the density distribution of RR Lyraes in the halo, finding that it is best fit by a broken-power-law model, in good agreement with previous work.

I go on to develop a set of tracer mass estimators that build on previous work which make use of actual (and not projected) distance and proper motion data, reflecting the amount and quality of data now available to us. I show that proper motion data is, in theory, very useful and can greatly increase the accuracy of the mass estimates; in practice, however, current analysis is hampered by the large errors inherent in the proper motion data. The results are also subject to mass-anisotropy degeneracy, which current data is not yet able to break. Nevertheless, I am able to estimate the mass of the Milky Way to be $M = 2.7 \pm 0.5 \times 10^{12} M_{\odot}$ and the mass of M31 to be $M = 1.5 \pm 0.4 \times 10^{12} M_{\odot}$.

Andromeda XII and Andromeda XIV are two M31 satellites that have been dubbed "extreme" and are thought to be on first infall into the M31 system. I modify the classical Timing Argument so that it can be applied to two external galaxies and then apply it to M31 and each of And XII and And XIV in turn to investigate the properties of their orbits. I then run a series of Monte Carlo simulations to investigate how likely such satellites are to exist and conclude that they are not as unusual as previously believed.

Finally, I discuss three upcoming wide-field, all-sky surveys and their implications for the future of the study of the Local Group.

1

Introduction

In my youth I regarded the universe as an open book, printed in the language of equations, whereas now it appears to me as a text written in invisible ink, of which in our rare moments of grace we are able to decipher a small segment.

- Arthur Koestler (1905-1983)

The Local Group (LG) of galaxies is literally just that: a group of galaxies local to our own; the neighbourhood. The term "Local Group" was first used by Hubble (1936) with the accompanying description of "a typical small group of nebulae which is isolated in the general field". Of course, we now know that the constituents of the LG are galaxies and not nebulae, as he believed, but the principle is true enough; it is a group of galaxies close to one another and isolated from other galaxies in this part of the universe.

The LG is dominated by two grand design spiral galaxies - our own Milky Way (MW) and the Andromeda galaxy (commonly referred to by its designation in the Messier catalogue: M31). The question of which of these two galaxies is predominant is unclear; recent work seems to suggest that M31 is the larger and the MW the more massive, but this is by no means certain. Regardless of the finer details, their sizes and masses are comparable, certainly with respect to the other inhabitants of the neighbourhood. There are a great many similarities and differences between the two galaxies: the overall structure and formation histories of the two are largely the same, however the details of that structure are particular to each galaxy. Both have an extended satellite population and we see evidence of tidal streams around both galaxies which may be attributed to the tidal disruption of such satellites as they fall into the dark matter potential.

The known satellite populations have swelled in the past decade thanks to the Sloan Digital Sky Survey (SDSS) data for the MW and extensive Canada-France-Hawaii Telescope (CFHT) data for M31. These surveys have been both wide and deep, allowing astronomers to probe the halos of both galaxies in unprecedented detail and with exceptional resolution. A host of dwarf spheroidal (dSph) galaxies have been found that were simply too faint and too diffuse to have been found by previous studies. However, the census of LG galaxies is by no means complete. The SDSS only covered a quarter

1 Introduction

of the sky and so there remains a vast swathe of the MW halo which has yet to be explored in such detail; undoubtedly there are a great many hidden dSph waiting to be discovered in these areas. M31, while having a more even coverage by virtue of the fact that it is an external galaxy, has also not been fully probed; there remain parts of the halo that have not been fully analysed and there are parts of the halo in which light from M31 itself will mask any fainter signal.

In addition to the two big spirals and their satellite populations, there are also a handful of isolated dwarf galaxies in the LG. While, at present, they appear to be much less common than the dwarfs that are part of a larger host system, they have been far less well studied than the dwarf satellites and it stands to reason that if there are faint satellites around the MW and M31, there are faint isolated dwarfs that we have yet to discover.

Dwarf satellites are apparently the smallest scales on which dark matter is found. Globular clusters (GCs) and dSph galaxies are very similar if we only consider their baryonic matter, with the dSphs being scaled-up versions of the GCs; however their masses and potentials tell a very different story. GCs are formed purely of baryonic matter with no evidence for any dark matter profile, however dSph galaxies must necessarily be highly dark-matter dominated if we are to explain their properties. Indeed, it is believed that they are the most dark-matter-dominated objects in the universe. This makes them a very important and very exciting laboratory in which to test fundamental dark matter physics.

Further, it is believed that structure forms hierarchically, with small objects forming first and then coalescing to form larger and larger objects. As the smallest scale on which dark matter is found, dSph galaxies are both the building blocks of all the structure that we see, which makes them very important for study, and it also means that they are very old and must have formed very early on in the history of the universe. As such, if we can understand these objects, we are probing back to the very origins of structure formation in the galaxy and their stellar populations will give us clues about the very first stars to have formed.

Of course, dSph galaxies are not only found in the LG; however it is only those in the LG that are near enough that we are able to resolve individual stars and so we are able to study them in far greater detail than any others. So too, are we able to study the structures and substructures in the MW and M31. While there is evidence for tidal streams in distant galaxies, the only data that exists is for integrated light; whereas for the MW and M31 we have resolved stellar populations and we can probe their halos and tidal streams in far greater detail and see much more substructure as we are able to look with much higher resolution.

The LG is a treasure trove of information for many aspects of astronomy and cosmology, as I will explain throughout this introduction. In Section 1.1, I discuss the formation and subsequent evolution of structure and substructure in the universe; giving particular consideration to what we can learn about the early universe from the present day configuration of galaxies like our own MW and its satellites. In Section 1.2, I review the properties of the major components of the MW, paying particular attention to the structure and substructure in the halo and the surveys that have provided so much of the data. In Section 1.3, I discuss the M31, its similarities and differences when compared with the MW and recent surveys that have greatly improved our knowledge of the galaxy and its environs. I continue in Section 1.4, with a discussion of the dSph galaxies found in the LG and explain why they are so important to study for our understanding, not only of the local astrophysics, but of the universe. Finally, in Section 1.5, I introduce the chapters of this thesis.

1.1 Structure formation

Any discussion on the structure and formation history of the MW's stellar halo or that of its satellites must necessarily start with a discussion of dark matter and of the formation and subsequent evolution of structure and substructure in the Universe as a whole as the topics are intimately and inextricably linked: the properties of the galaxies that we see today are greatly influenced by the conditions of the very early universe. In this Section, I will discuss the evidence for the existence of dark matter and why it is so important for structure formation theory, and I will then go on to describe a history of structure formation paradigms and summarise the current preferred theory (as much as one can exist in such a dynamic and evolving field). Finally, I will review some of the discrepancies that exist between theory and observation and discuss the prevalence of structure and substructure in galaxies like our own MW.

1.1.1 Dark matter

Zwicky (1937) observed that the mass estimated for galaxy clusters, such as the Coma Cluster, based on the number of observed stars was wildly discrepant to estimates based on the kinematics of the cluster galaxies. For the clusters to be bound, the cluster mass would have to be significantly larger than estimated from star counts alone, thus hinting at the existence of some massive, non-luminous matter in the universe.

Subsequent studies confirmed the analysis and the predictions therein; not only is the missing mass non-luminous, it is non-baryonic and there is a lot of it. Indeed, of all the matter in the universe, only 15% is familiar, baryonic matter, with the remaining 85% being dark matter. It later became apparent that all of this matter could only account for just over a quarter of the energy in the universe, with dark energy being responsible for the rest. While the census of these different components is now known to high accuracy thanks to the Wilkinson Microwave Anisotropy Probe (WMAP; Larson et al., 2010), their nature is less certain; the preferred dark matter particles are long-lived, cold and collisionless and are believed to be weakly-interacting subatomic particles, but these theories remain only theories and the search for the nature of dark matter continues. Ostriker & Steinhardt (2003) present a good review on the favoured dark matter candidates and how they might be confirmed or proved incorrect; they also discuss current problems between current observations and the theoretical predictions.

Dark matter is undeniably interesting in its own right; it is far more prevalent than baryonic matter, it accounts for more than a fifth of the total energy in the universe and the search for dark matter particles has particle physicists aquiver. But there is more; dark matter is the component of the universe that is responsible for the growth of structure in the universe and, as such, it underpins everything we see.

Primordial fluctuations in the density distribution of the early universe increased in size under the influence of gravity, with overdensities becoming more dense and underdensities becoming less so, in a runaway reaction that resulted in great, barren voids, threaded by complex networks of filaments, along which matter could flow and clump and form stars. Without dark matter, gravity would still exist and this behaviour would still have occurred, but on a far lesser scale; ordinary matter de-

1 Introduction

coupled from the radiation too late to explain the sizes of the structures that we see, whereas the dark matter decoupled earlier and so could interact under gravity entirely unchecked. And as the dark matter clumped, gravitational attraction brought the baryonic matter along with it.

Theory and observation are well matched on large scales as gravity dominates and only the primordial matter fluctuations need to be considered in a theory elegant in its simplicity. At smaller scales, however, the baryonic matter can interact with the radiation and there is a lot of complex physics that cannot be ignored; theory and observations do not yet agree, as I discuss in more detail in Section 1.1.3.

1.1.2 Overview of current structure formation theory

Eggen et al. (1962) (ELS) analysed properties derived from the velocity vectors of dwarf stars in the halo and found a strong correlation between the eccentricity of the orbit of these stars and their ultraviolet excess (which they used as a proxy for metallicity). They further argued that ultraviolet excess can be used as a proxy for age, such that a low UV excess (high metallicity) indicates a young star and a high UV excess (low metallicity) indicates an old star. This makes sense if we consider that the first generation of stars to form in the galaxy would be metal-poor but would enrich the ISM as they evolved; subsequent generations of stars would, therefore, have a higher metal abundance. Stars with highly eccentric orbits were found to have the lowest metal abundance and so are thought to be the oldest stars, low eccentricity stars had higher metal abundances and so are thought to be the youngest stars.

Comparison of the W -velocity vectors, which approximately indicates how high above the plane a star will travel, and their UV excess/metallicity/age revealed that the youngest stars must have formed near the plane but that the oldest objects could have formed at any height above the plane. From these correlations, they determined that the galaxy was not in equilibrium when the first stars formed but was instead contracting from a larger proto-galaxy. They predict that our galaxy formed 10 Gyr ago in a rapid, monolithic collapse of gas and the predicted a timescale for collapse of the order of 10^8 years; the gas was either rotating or was spun up during contraction. The radial collapse was halted by this rotation early but the z -collapse continued, resulting in a disk structure for the MW. The gas was heated in the contraction and radiated away some of this energy; as a result the gas and stars separated. The old, metal poor stars formed during the collapse remained on highly eccentric orbits, but the gas circularized in the plane so that any subsequent generations of stars formed close to the plane and on roughly circular, low eccentricity orbits.

This remained the standard picture of galaxy formation until work by Searle & Zinn (1978); they argued that for the pressure-supported slow collapse of a proto-galaxy with active star-formation and chemical enrichment, it is natural that a stellar abundance gradient will be set up, with both mean metal abundance and the range of metallicities falling off with distance from the galactic centre. Such a gradient is not seen in MW data and so a pressure-supported slow collapse model of galaxy formation is rejected in favour of a freefall collapse model, in line with the predictions by ELS. However, they suggest that the ELS model is too specific to fit the observed data; all that is required is that the outer halo GCs had uncorrelated kinematics and metallicities by the time they came into dynamical equilibrium with the galaxy.

In place of a monolithic collapse, they suggest a model whereby a number of small protogalaxies merge with the MW and slowly build up the stellar halo. In this model, the central regions of the galaxy form as in the ELS picture however the gas which forms the stars and clusters of the stellar halo continues to fall into the galaxy long after the collapse of the central regions has been halted. The infalling gas loses kinetic energy to become transient high density regions of star formation; these regions then disperse as they undergo chemical evolution and the stars and clusters formed therein come into dynamical equilibrium with the galaxy. The gas from these protogalaxies, however, is caught up into the galactic disk. The collapse of the central regions is still rapid but the accretion of the satellites that build up the stellar halo is slow - so slow that we can still see these accretion events happening today, 10 Gyr after the formation of the galaxy.

In reality, it appears that both the monolithic collapse and slow accretion formation mechanisms have contributed to the formation of the MW, although the latter is far more dominant, particularly for the outer parts of the halo, as I will discuss.

This model fits nicely into the lambda cold dark matter (Λ CDM) paradigm, which favours hierarchical structure formation and evolution (whereby small objects form first and then merge to form bigger objects) over top-down evolution (whereby large objects form first and then fragment or collapse to give rise to smaller objects).

It is not my intention here to delve into the intricacies of the cosmology of the early universe. The important point for the discussion that follows is that it is the growth of primordial density fluctuations in the very early universe that gives rise to the structures that we see today. Slight overdensities continue to grow in size through a gradual, hierarchical process of mergers and accretions, as was discussed in more detail in Section 1.1.1. For a more complete and in-depth review of the astrophysics of early galaxy formation and the tools that have been developed to study this topic, a recent review by Madau (2007) is an excellent place to start.

Simulating hierarchical structure formation is non-trivial. Ideally, we require exceptionally high resolution, which is, of course, extremely computationally expensive. Advances in the detail of the simulations reflect the advances that have been made in computer technology and the current state-of-the-art simulations are invaluable, however they still do not reach the resolutions that we need.

There are two ways in which astronomers attempt to simulate the merging and accretion of halos and subhalos. The first examines two halos in isolation in order to better understand the precise details of an accretion event; with only two objects to model, the resolution that can be achieved is very high. Although even in such a case as this, the host halo is often modelled as a fixed potential and it is only the satellite halo that is "live", which is clearly a gross oversimplification as the host halo potential will be changed by the very accretion events that are being modelled. The second method simulates the birth and evolution of structure on universal scales; starting with primordial fluctuations and the current cosmological paradigm, these simulations grow thousands of halos, built up by the continual accretion of small subhalos. The resolution that can be achieved for these simulations is, understandably, much lower, although the scope is much wider. Both techniques are vital to our understanding of galaxy formation, and indeed, recent studies have attempted to combine the two, however both have their drawbacks and there is much that remains poorly understood.

1.1.3 Overmerging and the missing satellite problem

Early N-body simulations of dark matter halo mergers suggested that the process was more efficient than observed (see e.g. White, 1976; White & Rees, 1978; Summers et al., 1995); that is, that no dark matter halo would survive once it had fallen into a larger halo, which is obviously not true, given the satellite galaxies that we see around our own MW. Later work revealed that this so-called “overmerging problem” was simply a consequence of the low resolution of the simulations and that subhalos could indeed survive inside the virial radius of the host halo (Moore et al., 1996; Klypin et al., 1999). This discovery, however, led to what remains one of the biggest stumbling blocks in the current galaxy formation paradigm; known as the “missing satellite problem”, it highlights, as the name suggests, a discrepancy between the number of satellites that we observe and the number of satellites predicted from theoretical simulations.

Kauffmann et al. (1993) used semi-analytic models of hierarchical structure formation to investigate merger histories for a range of dark matter halos and to study their satellite populations at the present day. They found that the standard CDM scenario overpredicts the number of satellites we should expect to see around galaxies like the MW. Dynamical friction was left as a free parameter in their simulations and they were able to fix the behaviour of dynamical friction to be such that the theory and observations agreed in number of satellites; as a consequence, however, they found that only lower mass systems survived mergers events and that LMC-mass objects were completely destroyed. The presence of the LMC orbiting the MW, and M33 in the M31 system, neatly disproves that solution. Finally, they concluded that the only apparent solution was to assume that there are many halos present in the MW that are, at present, undetectable.

Klypin et al. (1999) studied the circular velocity distribution of galaxy satellites in the LG and compared it to the results of numerical simulations of hierarchical structure formation. Once again, they found that the models predicted too many halos, regardless of the details of the model they assumed; thus implying that either the models were very wrong or that a large fraction of LG satellites has been “missed” by observations.

At around the same time, Moore et al. (1999) presented the results of a set of numerical simulations to study the hierarchical growth of structure on both cluster and galaxy scales. They found that they were easily able to reproduce clusters that closely resembled observations, such as the Virgo Cluster, and predicted that galaxy halos should appear simply as scaled version of cluster halos. However, this would result in a population of ~ 500 satellites around the MW, vastly discrepant to the handful of satellites then known. They too concluded that either the hierarchical paradigm was in error, or that there was more substructure in the MW halo that contained too few baryons to be observed with current equipment.

Recent dSph discoveries have gone a long way to alleviating this problem; the numbers of satellites observed (or at least assumed to exist, given the different depths to which various parts of the sky have been examined) and those predicted are still discrepant, though the difference is less than it once was. It is also worth noting that the sky has not been evenly surveyed and the new ultra-faint dwarfs have only been discovered in the $\sim 20\%$ covered by deep observations so the number of satellites is expected to increase further; this is discussed in more detail in Section 1.4.1.

1.1.4 Dominance and survivability of structure

So far I have discussed the subhalos that exist in and around their parent halos at the present day, but, of course, this is only half of the story. We have learned that subhalos do survive once they enter the parent halo, however, they will not survive forever; they will be tidal stripped of their material as they continue to orbit in the host potential, eventually being pulled apart entirely.

It is interesting, then, to consider what signatures these accretion events might leave behind and the survivability of structure in galaxy halos; how much substructure is there and how significant is it? For how long does the accreted material remain coherent, in both spatial and kinematic data? How much are we able to learn from the present stellar distribution about the properties of the accreted satellites and their orbits (which has implications for the properties of the Universe as a whole at the time of accretion)?

Helmi & White (1999) endeavoured to address such questions by running numerical simulations of the disruption of satellite galaxies in a MW-like potential and analysing properties of the resulting debris. The simulations spanned a long time frame to ensure that the debris had time to complete many orbits after disruption. They found that the debris disperses quickly spatially so that after 10 Gyr, there were no strong spatial correlations remaining in the debris from which separate accretion events could be identified, thus resulting in a reasonably smooth halo. This is because debris stars have completed sufficient orbits to visit all parts of phase space available to them. Conversely, they found that velocity signatures persist long after the progenitor satellite has been entirely torn apart by the host potential. Conservation of phase space density also means that the velocity dispersions of the accreted material decrease along a stream, so not only are the streams detectable in velocity space, but they are cold.

Bullock & Johnston (2005) also modelled the hierarchical formation of a MW-like potential, using a hybrid N-body and semi-analytic approach that allowed them to distinguish between light and dark matter. Their aim, to determine how much of the stellar halo could have been built up by accretion events (similar to the Searle & Zinn (1978) paradigm) and how much was formed in situ (possibly via an a mechanism similar to that described by Eggen et al. (1962)). Their simulated halos were formed purely from accreted satellites, with no underlying smooth component, however they also assume only a slowly growing host potential that does not account for major mergers.

They concluded that stellar halos assemble from the inside out (as expected in a hierarchical scenario) with nearly 80% of the halo mass being deposited by the ~ 15 most massive progenitors and with a median accretion time of ~ 9 Gyr ago. The outer halo and the existing satellites that we see in the MW today were accreted more recently (median time ~ 5 Gyr ago), thus, they should be chemically distinct from the inner halo of the MW (as is indeed the case, as I will discuss later). They also noticed that the stellar distribution of the debris was more centrally concentrated than the dark matter since the stars are more tightly bound to their progenitors. Finally, they concluded that substructure in the halo should be abundant and visible and that it is possible that galaxy halos are built up almost entirely from disrupted satellites.

This conclusion was supported by Bell et al. (2008) who tried fitting smooth prolate, oblate and triaxial halo models to the SDSS DR5 colour-selected main sequence turn off (MSTO) stars and found poor fits in every case because the halo is highly structured and the assumption of a smooth profile is

1 Introduction

a bad one. They went on to compare their distribution of halo stars to the Bullock & Johnston (2005) simulations. They found the simulation output to be a good match to the MW data, both in terms of the amount of substructure and its nature, thus concluding that the dominant formation mechanism of galaxy halos (at the very least of the MW halo) is the accretion of subhalos. They cannot entirely rule out the possibility of an underlying smooth component also being present, however it is certainly not dominant.

1.2 The Milky Way

In a very broad sense, the main components of our galaxy are understood: the MW is made up from a central, flattened spheroidal bulge; an exponential disk, which can be further split into a thin disk and a thick disk and which has logarithmic spiral arms; all surrounded by an old, metal-poor, extended, spherical halo. However the mechanisms by which these components formed and their evolution history is less clear and is an exciting area of current research. Dark matter is the dominant mass component of the galaxy with an order of magnitude more mass in dark matter than there is in luminous matter; from galaxy rotation curves, for example, we know that dark matter must be present, but the shape and substructure of the density profiles is not known.

In this section, I discuss the structure of each component of the Galaxy in more detail, paying special attention to the halo and what it can tell us about its formation history. I will also discuss some recent surveys that have been so important to our understanding.

1.2.1 The bulge

Galactic bulges are the flattened spheroidal systems found at the centres of most of the spiral galaxies that we can see in the universe; their populations are chemically, photometrically and kinematically distinct from disk populations. The MW is a typical spiral galaxy and does itself contain a bulge; being the closest bulge to us it is the one that has been the most extensively studied and is very important for our general picture of galaxy structure and formation. Further, Jablonka et al. (1996) showed that bulges and elliptical galaxies occupy the same region of the fundamental plane, so understanding the bulge of our galaxy will have implications for our understanding of ellipticals as well. At the very centre of our galaxy lies Sagittarius A*, a very massive compact object which is now generally accepted to be a supermassive black hole; indeed, it is now believed that all spiral galaxies, all such bulges, harbour a supermassive black hole in their cores.

Spiral galaxies display a range of morphologies, the two main differences we see from one galaxy to the next are how tightly the spiral arms are wound and the shape of the bulge in the centre; some spirals have spherical cores while some are very strongly barred. The exact shape of the MW bulge is still a subject of some debate, that the MW bulge is not spherical is largely agreed upon, but whether the bulge is simply barred or is highly triaxial is a topic of ongoing research. From our position in the MW, we are looking almost straight down one axis of the bulge and it is difficult to distinguish between these two models.

Observations of the bulge are somewhat difficult in that there is a lot of contamination from foreground disk stars. Kuijken & Rich (2002) collected HST photometry and proper motions in two

fields towards to the bulge and separated the disk and bulge populations using kinematic data alone. They found that the Hertzsprung-Russell diagram for the bulge shows an old turn-off population with no evidence of blue stragglers or an intermediate age population. This results in a population that is nearly identical to those found in old, metal-rich GCs, although the bulge has a much broader giant branch indicating a wider range in metallicities given that the position of the giant branch is very sensitive to metal abundance. This confirmed work done by Terndrup (1988), who first argued for a bulge with properties similar to GCs, Ortolani et al. (1995), who carried out a similar analysis using different data in only one of the fields, and Feltzing & Gilmore (2000), who used star counts of stars brighter and fainter than the turn off to reach the same conclusion.

Their analysis of the HST data also found direct evidence for the rotation of the bulge population. They found a line-of-sight gradient in the rotation velocity, which explains the observed proper motion anisotropy, and when this gradient is removed from the data, the resulting velocity distribution is nearly isotropic. Chemically, the MW bulge has a wide-range of $[\text{Fe}/\text{H}]$ and an enhancement of α -elements.

The mechanism by which the bulge was formed is still not well understood and whether the bar formed with the bulge or formed later is also unclear. However there is increasing evidence supporting fast formation with a timescale of around 1 Gyr; chemical analysis and stellar ages require that stars were formed early and self-enriched their surroundings rapidly. This picture does not favour accretion models where the bulge is built up over a long period of time after a series of small accretion events. Spectroscopic analysis supports a fast formation time for the bulge, as do theoretical considerations by Elmegreen (1999), who states that gas-to-star conversion must have happened over a few dynamical timescales because the potential well of the bulge is too deep to allow for self regulation. Comparisons of the metallicity distributions for the MW and near neighbour M31 by Sarajedini & Jablonka (2005) also favour fast formation: the two halos have very different metallicity distributions but this is not so for the bulges, this implies that the stars were formed before any significant accretion had taken place and that the two galaxies share a common mechanism of bulge formation.

To summarize, the bulge is a high-density region dominated by Population II stars, with no evidence for stars younger than 10 Gyr, and it probably formed over a short time, around 1 Gyr. The MW bulge is a flattened spheroid, possibly highly triaxial, it is rotating and it hides a supermassive black hole at its centre.

1.2.2 The thin disk

The thin disk of our galaxy is best represented by an exponential disk model with logarithmic spiral arms. The thin disk is estimated to be around 10 Gyr old and has sustained star formation at a steady rate since its formation; as a result, the stellar content of the thin disk has a large range of ages. As well as stars, the thin disk contains a lot of gas and dust out of which the stars form. The dust obscures our view at optical wavelengths but recent near-infrared and far-infrared studies have been able to see through the dust and greatly increase our understanding of previously hidden parts of the galaxy. Both the stellar population and the dust content show a definite galactic warp; the amplitude of the warp is different for the two populations.

The spiral arms contain the youngest stars in the disk and are the site of a lot of active star

1 Introduction

formation. Their population is concentrated very close to the plane of the disk with a scale height of just 100 pc. HI clouds, HII regions, molecular clouds, protostars, O stars, B stars, supergiants and Cepheid variables are all found in the spiral arms, however, the stellar density inside 3 kpc is very much less than the HI density, indicating that the disk has a central HI hole. The steady star formation history over the past 10 Gyr has resulted in a lot of supernovae enrichment and so the spiral arm population is found to have supersolar metallicity.

Georgelin & Georgelin (1976) used optical observations of young stars and radio observations of HII regions to map the spiral structure of the MW, they proposed that the galaxy has four spiral arms, to which we now add the local Orion arm as well, in which our Sun resides. There are a number of uncertainties inherent in the analysis due to the kinematic distances used, but the work is still taken as the standard model for the spiral structure of the galaxy. However, the number of spiral arms that the MW possesses remains a topic of debate.

The disk population has a very much smoother distribution than that of the spiral arms, there is no trace of spiral structure. The stellar ages range from 1-10 Gyr; the scale height of the population increases with age from 200 kpc to around 700 kpc and the metallicity decreases with age to around 20% solar. The typical content of this disk population are A stars, planetary nebulae and white dwarfs.

Drimmel & Spergel (2001) fit joint models for the stellar and dust content of the galaxy to COBE near- and far-infrared data. They estimate a scale-length of $\sim 0.3 R_{\odot}$; this is smaller than expected given some previous NIR estimates, which are still subject to some amount of obscuration by dust, but in line with more recent data. This value is also in good agreement with local kinematic analysis using Hipparcos data by Dehnen & Binney (1998). Visual wavelength analysis was previously heavily affected by dust obscuration but new techniques are bringing the estimates more into line with small scale-length values, although this is not true in all cases. Overall, the smaller scale-length estimates do seem to be robust.

The small scale-length results have important implications for the mass distribution in the galaxy: the galactic rotation curve is best fit by maximal disk models (Dehnen & Binney, 1998), which implies a low central density for the dark matter halo, contradicting some CDM simulations.

Further, they found that the amplitude of the galactic warp is different for the stellar and dust components, hinting at the importance of hydrodynamic or magnetohydrodynamic effects in the study of the warp. This also suggests that the warp may be only a short-lived feature, perhaps induced by interaction with a nearby galaxy (the Magellanic Clouds and the Sagittarius dwarf galaxy have both been proposed); such an interaction would affect the stars and dust differently, giving rise to different warp amplitudes.

1.2.3 The thick disk

Burstein (1979) and Tsikoudi (1979) found evidence that the vertical light distribution in some edge-on galaxies was best fit by two exponential density laws instead of just one: a thin disk and a thick disk, with smaller scale-heights and larger scale-heights respectively.

Gilmore & Reid (1983) first established the existence of a thick disk in the MW. They used apparent magnitudes and absolute magnitudes derived from photometric parallaxes to investigate the luminosity function and the density distribution of stars in a region near the South Galactic Pole.

They found that the luminosity function steepens significantly at a distance of ~ 1 kpc from the plane of the disk, indicating that there is a significant change in the dominant population at this distance. Further, they found that two density laws were needed to fit the data, indicating that there are two distinct populations present. The first they associate with the thin disk and is best fit by an exponential model with a scale-height ~ 300 pc, as was previously known; this population dominates for heights 100 pc - 1 kpc above and below the disk. The second population was found to fit an exponential law and a power law equally well; the exponential model, with a scale-height of 1450 pc, is favoured after consideration of other galaxies that also show evidence for two disk structure. This population dominates for heights 1 kpc - 5 kpc from the plane of the disk and is recognised as the thick disk.

The thick disk was found to be metal-deficient compared with the thin disk; this, along with the steepening of the luminosity function between the thin disk and the thick disk, implies that the thick disk population is older than that of the thin disk. The luminosity function steepens for older stars and an older population will be more metal-poor because there has been less time for significant enrichment when it forms.

Thick disk structure is only seen in galaxies with a discernible bulge (van der Kruit & Searle, 1981), indicating that the thick disk and the bulge are related, which in turn implies that the thick disk stars are rotating rapidly about the Galactic centre. However, Gilmore et al. (2002) used a spectroscopic study of F/G stars in the Galactic plane to study the rotation velocity of the thick disk; they found that it was much slower than expected and so they suggest that the thick disk was formed as the result of significant (though not major) merger between the MW and a satellite galaxy, which would then “puff up” a thin disk population already in place.

1.2.4 The halo

It is clear from the earlier discussion of structure formation (see Section 1.1), that the stellar halos of galaxies contain extensive fossil records of their own formation history, spatially, kinematically and chemically. This property arises solely from the merger mechanisms that build-up the halos and, as such, is true for galaxies of all Hubble types. If we are to truly understand the formation of galaxies then an understanding of the properties of stellar halos is vital.

The MW halo is, of course, the closest halo to us and it therefore provides the best dataset that we have at our disposal; indeed, it is one of the only halo datasets at our disposal as galaxy halos have low surface brightness and so they are very difficult to detect around external galaxies - even the stellar halo around M31 was only detected very recently (Chapman et al., 2006; Kalirai et al., 2006). Further, because of the ubiquity of structure formation, in studying the MW halo, we are not only gaining a deeper appreciation of its own formation history, but of the formation histories of every galaxy in the universe. There will be peculiarities and idiosyncrasies unique to every galaxy, but the general properties will be principally the same.

The halo can be explored using a plethora of different objects on a number of different scales; variable stars are popular tracers as they generally make good standard candles. RR Lyraes (see Section 3.1) in particular are excellent standard candles thanks to their narrow range of absolute magnitudes; the fact that they are reasonably common so can be expected to be found throughout the halo and in any substructure means that they are widely used as a tracer population. Blue horizontal

1 Introduction

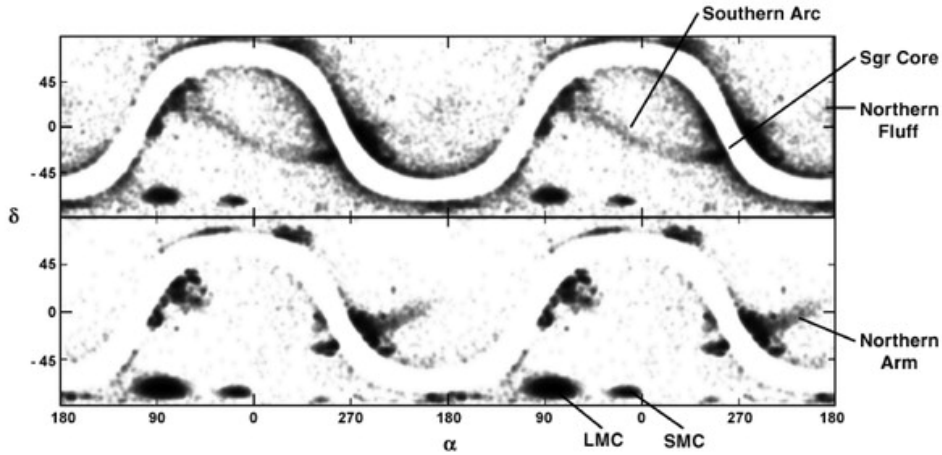


Figure 1.1: The view of the Sgr dSph and its tidal stream from 2MASS (Majewski et al., 2003). The stream can be traced through a full 360°

branch (BHB) stars, blue straggler (BS) stars and M-giant stars are also commonly used as tracers as they are, again, reasonably common and can be selected simply with judicious colour cuts or simple spectroscopic analysis. GCs and dSph galaxies are also important and frequently-used tracers; their populations are smaller than stars, of course, but we are able to probe the halo out to a far greater extent with these objects as the dark matter potential of the host galaxy extends out beyond the radii reached by the outermost stars. High velocity clouds (HVCs) have also proved useful in studies of the halo. All of these methods offer complementary view points on what we now believe is a very complex system and so it is not enough to study only one tracer population to truly understand the nature of the halo or its substructure; this point is well illustrated by a recent survey of RR Lyraes and BHB stars near the NGP by Kinman et al. (2007) who found different kinematic properties for the two populations.

Streams and other substructure

Sparse and with a stellar mass of $\sim 10^9 M_{\odot}$, only 1% of the total stellar mass of the galaxy, the MW halo was once thought to be rather uninteresting. It contained very few stars, compared with the other components of the galaxy, and those stars were thought to be evenly distributed throughout the halo. As a result of the hierarchical regime under which the halo has been formed, the reality is very different.

Streams of stars, torn from tidally disrupted galaxies as they fall into the MW, are seen across the sky with kinematics and metallicities that are distinct from their surroundings; as instrument sensitivity increases, so more and more streams come to light. The best-known and most impressive example of a tidal stream is that left behind by the Sagittarius (Sgr) dSph on its journey around the Galaxy; the stream can be traced through a full 360° (see Figure 1.1, Majewski et al., 2003) and has been studied using a variety of tracer objects, yielding much information for inquisitive astronomers. But it is by no means the only stream identifiable in the halo.

Belokurov et al. (2006) used SDSS DR5 data in the North Galactic Cap to search for substructure in the halo by applying a colour-cut to the data and then overlaying maps for three different magni-

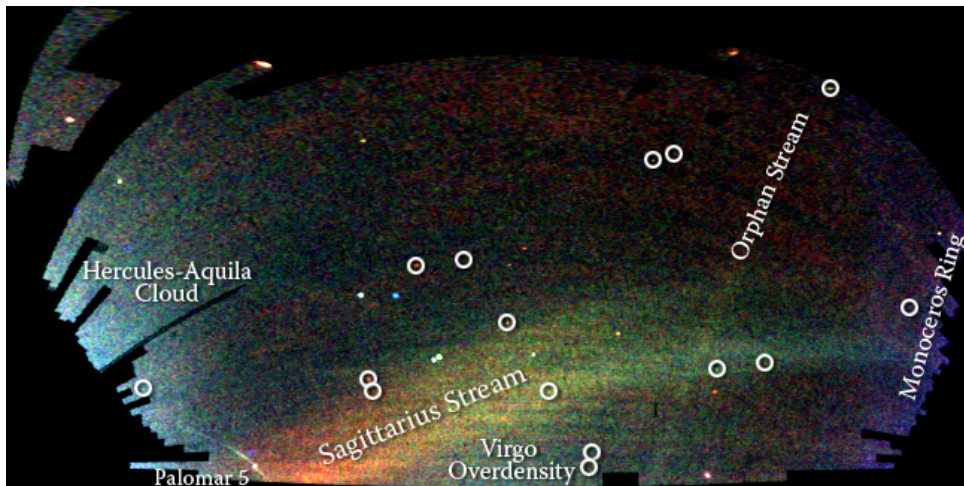


Figure 1.2: The “field of streams” (Belokurov et al., 2006). The bifurcated Sagittarius tidal stream dominates the field, but we also see the Orphan and the Monoceros streams, the edge of the Hercules-Aquila Cloud, the edge of the Virgo Overdensity and the Palomar 5 GC stream. A number of satellite galaxies are also highlighted.

tude bins; the resulting graph is shown in Figure 1.2. This analysis revealed a number of streams in excellent detail and, so busy is that section of the sky, that it has been dubbed the “Field of Streams” (although it should also be noted that a number of dSph galaxies are clearly visible in the image as well along with the edges of two substructures whose natures are unclear).

The most prominent stream is the Sgr stream which dominates the field plotted; it appears to bifurcate and there is further evidence for another wrap behind the lower branch as well, thus providing data for multiple orbits of the progenitor galaxy. By modelling the stream and fitting the bifurcation, Fellhauer et al. (2006) concluded that the halo must be close to spherical; in disagreement with Helmi (2004) who found evidence favouring a prolate halo shape, Johnston et al. (2005) who prefer an oblate halo and Law et al. (2009) who determine a triaxial halo. The Fellhauer et al. (2006) analysis also predicts that the two forks in the bifurcation are from different parts of the stream with the upper portion being from the old trailing arm and the lower being from the young leading arm, however subsequent analysis (Yanny et al., 2009; Niederste-Ostholt et al., 2010) has shown that both arms are composed of leading debris, which calls their predictions of halo shape into question.

Also visible are the Orphan and Monoceros streams. The Orphan Stream (Belokurov et al., 2007) is so named because its progenitor is not known; a number of attempts have been made to find a progenitor among the known consensus of satellites but none have, thus far, been successful. Fellhauer et al. (2007) suggested the dSph Ursa Major II (UMaII) and Jin & Lynden-Bell (2007) considered Complex A, however these were both ruled out by Sales et al. (2008) in an analysis of the properties the progenitor might have had; their simulations suggest that a dSph similar to the “classical” dSphs would be a most probable candidate. Recently, Newberg et al. (2010) also disfavour UMaII and Complex A as possible progenitors; they do find Segue 1 to be a possible progenitor but the results are not conclusive. The progenitor of the Monoceros Stream (Newberg et al., 2002; Yanny et al., 2003, also known as the Monoceros Ring or the Anticenter Stream) has also not yet been identified; Canis Major has been put forth as a candidate (Martin et al., 2004) but more reliable kinematic data is needed before this can be confirmed or disproved (Peñarrubia et al., 2005).

1 Introduction

Of the other streams found in the halo, some are believed to be left by disrupting GCs and not by dSphs (e.g. Palomar 5 (Odenkirchen et al., 2002), GD-1 (Grillmair, 2006), the Cetus Polar Stream (Newberg et al., 2009), Acheron, Cocytos, Lethe (Grillmair, 2009)). Palomar 5 is also visible in the bottom left of Figure 1.2 - as is typical for GCs due their smaller size, this stream is much narrower than those left by disrupted dSphs.

And it is not just streams that can be identified in the halo: Figure 1.2 also shows parts of the Virgo Overdensity (Juric et al., 2008) and the Hercules-Aquila Cloud (Belokurov et al., 2007), two very large overdensities of stars that span large areas of the sky. They are believed to be the remnants of disrupted satellites, but whether they are sections of streams or the destroyed remains of progenitor cores is not yet known. I describe the discovery of a third overdensity, the *Pisces Overdensity* in Chapter 3.

The halo is clearly not quiescent and there is a lot of material there that has come from accreted objects, in line with the predictions that the halo is composed primarily, if not entirely, via mergers (Bullock & Johnston, 2005; Bell et al., 2008).

Halo properties

As instrumentation becomes more sensitive, we are able to see further out into the halo and to see the stars and structure there in more detail. However, we still lack the tools necessary to directly see the dark matter - which is not to say that we know nothing about it, simply that we are only able to infer its properties (indeed, its existence) indirectly. The circular velocity curve of the MW stays flat out to radii far beyond that at which we cease to detect stars, indicating that there must be mass that we are unable to see that extends beyond the limits of the stellar halo.

This broad picture is generally agreed upon but the exact shape of the dark matter halo is still unclear. As I have already discussed in the previous section, different analyses of Sgr stream data indicate spherical (Fellhauer et al., 2006), prolate (Helmi, 2004), oblate (Johnston et al., 2005) and triaxial (Law et al., 2009) halos and a number of different halo models can be found to fit various data, though none fit perfectly. Logarithmic halos with variable flattening, Navarro-Frenk-White (NFW, Navarro et al., 1996) profiles with parameters concentration $c \sim 12$ and virial radius $r_{\text{vir}} \sim 258$ kpc (Klypin et al., 2002) are most commonly adopted for the dark matter; truncated flat models (Wilkinson & Evans, 1999) also fit the data. The baryonic component is then embedded within the dark matter halo; the stars do not follow the dark matter profile though, they are more centrally concentrated than the dark matter with an effective radius inside the solar circle (Frenk & White, 1982).

The stellar halo contains old, metal-poor Population II stars and there is increasing evidence that these may be divided into multiple components. Using SDSS data, Carollo et al. (2007) showed that the MW halo is clearly divisible into two components that are spatially, chemically and kinematically distinct. The inner halo is the dominant component out to ~ 10 kpc and is filled with stars on highly eccentric orbits that describe a flattened density distribution and have zero or a very small net prograde motion. The metallicity of the inner halo peaks at $[\text{Fe}/\text{H}] \sim -1.6$. The outer halo, on the other hand, dominates beyond ~ 20 kpc and is filled with stars that describe orbits with a wide range of eccentricities, both low and high. The outer halo is spherical in shape and shows a significant net prograde motion with a metallicity peak of $[\text{Fe}/\text{H}] \sim -2.2$. The quality and quantity of the SDSS data

used for this study, highlighted this dichotomy beautifully and in more detail than ever before, but this dual nature of the halo was not a new concept.

Hartwick (1987) analysed the spatial distribution of metal-poor RR Lyraes and found that within the solar circle they described a flattened distribution and that outside they were spherically distributed, Sommer-Larsen & Zhen (1990) also found evidence for a two-component halo, with the inner component being flattened and (Chiba & Beers, 2001) confirmed these findings with a large sample of local halo stars. With regard to kinematics, Carney et al. (1996) found that stars close to the Galactic plane showed a small net prograde motion while those that reached large distance from the plane had a net retrograde motion; a result confirmed by Morrison et al. (2009) in a study of metal-poor halo stars with excellent 6D kinematic data. These distribution and kinematic differences can also be seen in the MW GC populations, which can thus be split into inner and outer halo members Zinn (1993).

Simulations, too, demonstrate that a two-component halo is a natural result of galaxy formation. Bekki & Chiba (2001) found that they were able to reproduce a two-component halo in simulations with the outer halo forming by the dissipationless merging of subhalos and the inner halo forming via dissipative merging between clumps, adiabatic contraction due to the disk and accretion of gas onto the equatorial plane. The formation mechanisms involved naturally explain the sphericity of the outer halo and the flattening of the inner. They also find that only minor mergers can take place after disk formation or the disk would be destroyed, which places limits upon the size of any merger that would form the inner halo. This scenario seems to indicate that part of the inner halo forms in situ, and that it accretes more matter as the Galaxy evolves. Simulations by Abadi et al. (2006) favour a paradigm whereby the inner halo is formed in situ (with the outer halo forming via mergers). Whereas, as I have already discussed in more detail in Section 1.1.4, Bullock & Johnston (2005) concluded from their simulations that it is possible for the entire halo to be formed entirely via accretion mechanisms. They suggest that destroyed satellites accreted 9 Gyrs ago make up the inner halo and that the outer halo and the present-day satellite populations consists of subhalos accreted much more recently, only 5 Gyr ago. The different accretion times account for the difference in spatial and kinematic properties, as the structure of the MW will have changed in the intervening few Gyr, thanks to the accreted material itself; further, the satellites will have had different properties at the time of infall and so will be chemically distinct.

Halo surveys

Courtesy of recent medium- and large-scale surveys, parts of the MW stellar halo have been studied in unprecedented detail; some by design and some by happy coincidence. Survey coverage, however, is uneven and other parts have only been very poorly studied. As such, our knowledge of the MW halo is erratic - limited by the extents of surveys and further complicated by the superposition of much brighter components (the disks and the bulge) and by the extremely low density of halo stars. Yet, patchy though the coverage may be, recent surveys have been instrumental in increasing our knowledge of the halo.

One such survey that has recently been completed is The Two-Micron All-Sky Survey (2MASS, Skrutskie et al., 2006), which, as the name suggests, was a near-infrared (NIR) survey in three pass-

1 Introduction

bands that uniformly scanned the whole sky, aiming to explore large-scale structure in the MW and in the local universe. They were able to achieve excellent signal-to-noise ratios, and thus the sensitivity of the data is far greater than any previous NIR study. The principle advantage of this survey is that the whole of the MW is suddenly available to study as the NIR wavelengths are able to penetrate the dust that obscures much of the central parts of the MW from our view. The survey has had its uses in many areas of astronomy; I shall concentrate here on those studies applicable to the MW halo and simply note that this is but one small use of such a magnificent data set.

Majewski et al. (2003) extracted M-giant stars from the 2MASS dataset and were able to trace the Sagittarius (Sgr) dwarf galaxy and its tidal stream through a full 360° (this was the first study to do so, all previous studies were only able to study sections of the stream), finding that both the leading and trailing tails describe a well-defined orbital plane about the Galactic centre. They followed up on this study by obtaining spectroscopic data for several hundred of their M giant candidates (Majewski et al., 2004); enabling them to get much tighter constraints on the velocity dispersion of the stream than had previously been achieved.

Johnston et al. (2005) went on to use the Sgr M-giant data to investigate the precession of the Sgr orbit by measuring the offset between the poles of the great circles described by the leading and trailing debris. Comparing their results to simulations that assume a variety of halo shapes, they strongly favour oblate halos with only a moderate degree of flattening, over prolate halos or extremely flattened systems. Unfortunately, the results from this analysis are not consistent with the results from the other Sgr data (which, it should be noted, are also not consistent with each other), although this is arguably due to the models and methods employed in the analysis and not the data itself. Law et al. (2005) also compared M-giant data for the stream to the results of both test-particle orbits and N-body simulations in order to probe the Galactic halo. From the velocity gradient of the trailing stream and the apocenter of the leading stream they were able to estimate the mass of the MW within 50 kpc and using the velocity dispersion and width of the young trailing stream, they were able to estimate the present-day bound mass of the Sgr dSph. They also considered the precession of the orbital pole of the young debris and velocities of the leading debris, and surmised that the orbit of Sgr has evolved over in its recent past.

More recently, Chou et al. (2007) used the 2MASS data for Sgr to study the metallicity distribution function (MDF) in the core of the progenitor and along the stream. They found evidence for a significant gradient in metallicity, hinting that there was such a gradient in the progenitor before it began to be tidally disrupted; further, the Sgr core and its stream is generally more metal-rich than the halo, providing direct evidence that the present-day dSphs are chemically different from those which made up the bulk of the stellar halo.

Another survey that has provided insights into the stellar halo in the past decade is the Quasar Equatorial Survey Team (QUEST) RR Lyrae Survey (Vivas et al., 2004), which scanned 380 deg^2 of the sky in V-band magnitudes corresponding to a heliocentric distance range of 4 - 60 kpc. The primary focus of the original QUEST survey, as the name suggests, was to study quasars, however the coverage and depth achievable with the QUEST camera made it an ideal resource for the study of RR Lyraes as well and so it was also put to this use. RR Lyraes are a type of variable star commonly found in all components of our Galaxy; their regular periodicity and distinctive lightcurves make them easy to identify and their narrow range of absolute magnitudes make them excellent standard candles and so

they have been widely used to study the structure of the MW. I will not go into detail here as I describe RR Lyraes, their particular properties and their suitability for halo studies in some detail in Chapter 3; I then go on to explain how I have used RR Lyraes to probe the Galactic halo.

Vivas & Zinn (2006) describe the identification of halo substructures using the QUEST RR Lyraes; the most significant detections were of the northern part of the Sgr tidal stream and of the Virgo Stellar Stream (Duffau et al., 2006), although they also found overdensities near the Monoceros Stream and the Palomar 5 GC and there was further evidence for some less significant overdensities. This degree of substructure over a range of different scales indicates that the halo is highly structured (a conclusion which I will confirm in Chapter 3); however, away from the major overdensities, they found the distribution of RR Lyraes to be well modelled by a smooth halo with variable flattening, where the flattening decreases with increasing Galactocentric distance, in agreement with Preston et al. (1991).

More recently, Vivas et al. (2008) used QUEST RR Lyraes to study velocity structures towards Virgo and found evidence to suggest that the Virgo Overdensity is, in fact, composed of a number of separate substructures. As predicted by Helmi & White (1999), these substructures were not seen spatially but were clearly identified kinematically, demonstrating once again the persistence of coherent structures in velocity space. And Mateu et al. (2009) used the QUEST camera to survey ~ 20 deg² in the region of the Canis Major (CMa) overdensity, finding only a handful of RR Lyraes, as would be expected of contributions from the halo and thick disk populations, and finding no evidence for an excess that would indicate the dSph galaxy postulated to also reside in that part of the sky.

Archival data for the Southern Edgeworth-Kuiper Belt Objects (SEKBO, Moody et al., 2003) survey has also been searched for RR Lyraes, finding significant populations coincident with both the Sgr stream and the Virgo overdensity. Like many datasets used to study the halo, this survey was not designed for the purpose but the coverage and nature of the observations made it ideal for such a study anyway. As is the case for the 2dF Quasar Redshift Survey (2Qz, Croom et al., 2004); the name gives a clear indication of the original purpose of the study, yet De Propris et al. (2010) have studied the halo using BHB stars, another common tracer population used to study the halo (see also Yanny et al., 2000; Xue et al., 2008). This study has detected the stellar halo out to a radius of ~ 100 kpc, confirming the study by Starkenburg et al. (2009) who used the Spaghetti survey Morrison et al. (2000) to find a similar result. Such a distance is further than previously assumed for the extent of the MW - Xue et al. (2008) were only able to detect the halo out to ~ 60 kpc using BHBs and Brown et al. (2010) detected the halo slightly further out to ~ 75 kpc with hypervelocity stars (HVS) and Robin et al. (2007) used the COSMOS survey to probe the halo out to ~ 80 kpc - however, it is much more in line with M31, which has been traced out as far as ~ 165 kpc (Guhathakurta et al., 2005).

However the biggest contribution to our halo archaeology has undoubtedly come from the SDSS. The SDSS underpins much of the work described in Chapters 2 and 3 and is, therefore, discussed in great detail in Section 2.1. Here I shall simply give an overview of some of the fantastic science in the field of Galactic archaeology that has resulted from the survey. A large number of new dSph galaxies have been discovered inside the survey's limits, smaller, fainter and more diffuse than the previously-known, "classical" dwarfs. The Sgr stream has been traced in both the Northern and Southern hemispheres - with a bifurcation clearly seen in the Northern data (although, as I have already discussed, the origin of the bifurcation remains unclear and it a topic of extensive current research). As I have already discussed earlier in this section, a host of other known streams have also been detected in the

1 Introduction

SDSS and yet more have been discovered along with the identification of a number of unquantified substructures, one of which, the Pisces Overdensity, I describe in Chapter 3.

The success of the SDSS for studying the Galaxy is remarkable because the survey was not originally conceived as Galactic survey, it was designed principally with extragalactic targets in mind, and yet has been tremendously useful for Galactic archaeologists; indeed, the benefit to LG science was recognised in follow-up programs SDSS-II and SDSS-III, with projects focused on answering questions about the Galaxy.

1.3 The Andromeda galaxy

M31 plays an incredibly important rôle in our understanding of the structure and formation history of galaxies. Its existence was first recorded as “small cloud” by Persian astronomer al-Sufi in 964 CE in his “Book of Fixed Stars” and since then it has appeared on star charts of the sky, with its name evolving to reflect the increasing knowledge of the universe. One of the brightest objects in the Messier Catalogue, it was long believed to be a nebula in our own Galaxy, indeed, in 1785, Herschel declared it to be the nearest of the all the great nebulae, and for a long time it was known as the “Andromeda Nebula”, named for the constellation in which it is found. Its spiral structure was first observed by Roberts in 1887, but it was not until Hubble’s discovery of extragalactic Cepheid variable stars in 1925 that it was understood to reside outside of the MW.

As the nearest spiral galaxy to the MW - a mere 785 kpc away - we are able to resolve individual stars within it and to take deep photometry and high-resolution spectroscopy of those stars. Stars in the MW are even closer, of course, and can be studied in even greater detail, however we are sitting in the middle of the MW and this has some disadvantageous effects on our observations. We are unable to see through the optically-bright bulge and disk so there is a swathe of the Galactic halo on the other side of the Galactic Centre that we cannot study optically; NIR wavelengths are able to penetrate the dust, but, as in all things, multi-wavelength analyses are a great advantage when studying such a complex system. Added to this, the MW observations suffer from selection effects as a result of our unique viewpoint inside the Galaxy and yet offset from the Galactic Centre; a problem that we do not have for M31. So observations of M31 give us a detailed, external view of a galaxy like our own.

And M31 is indeed a galaxy very like our own. The MW and M31 are both grand design spiral galaxies; like the MW, M31 contains a central spheroidal bulge, an exponential disk with logarithmic spiral arms and an old, metal-poor, extended, spherical halo. There is also evidence for a thick disk component to M31’s disk, separate from the well-studied thin disk that has been long-known. Both galaxies contain streams and coherent overdensities in their halos, telling stories of their cannibalistic history, and both are surrounded by populations of satellite galaxies and GCs. Both galaxies are believed to be of similar mass, although the finer details of this statement are debated, with works claiming both the MW and M31 as the more massive galaxy, and further works estimating their masses to be equal - indeed, it is these discrepancies that, in part, gave rise to Chapter 4.

Guhathakurta et al. (2005) found the first evidence for an extended metal-poor halo in M31. While studying the spheroid component, they found metal-rich stars within a radius of ~ 30 kpc with a density that fell off exponentially as $r^{-\frac{1}{4}}$, typical of a bulge population. However they also found

a clearly distinct metal-poor population extending out to ~ 165 kpc. Kalirai et al. (2006) confirmed the discovery by studying RGB stars in 12 fields in M31 halo spanning radii from 12 kpc out to 165 kpc. They found the metallicity of the spheroid component to decrease with radius; consistent with the presence of a metal-rich central bulge and a more extended metal-poor halo component with a surface brightness profile that falls off like R^{-2} . They also found the mean metallicity and metallicity spread of the M31 halo to be similar to those of the MW halo.

Of course, while the basic galaxy structure of M31 is the same as the MW, there are a great many differences between the two galaxies that emerge when we begin to look at both in more detail: the largest M31 satellite Triangulum (M33) is larger and more massive than the MW's largest (the Large Magellanic Cloud (LMC)); the Giant Southern Stream (GSS) in M31 is also broader than the best that the MW has to offer (the Sgr Stream); and, in a recent study of HST photometry, Richardson et al. (2009) concluded that the halo of M31 is more metal rich than that of the MW out to a radius of at least 60 kpc. Although, while there appears to be some difference between the inner halos of the two galaxies, the outer halos are quite similar; a result that is not too surprising if you consider that a single significant-but-not-major merger is thought to be responsible for the some properties of the inner halo while the outer halo is believed to be formed from the continual accretion of many smaller objects. Differences in the inner halo progenitors could greatly influence the properties of the inner halo, while we expect the average properties of the outer halo accretions to be consistent.

In general, the satellite populations of the two galaxies appear to be broadly similar (van den Bergh, 2006); both have large "classical" dSphs in orbit as well as a population of recently-discovered ultra-faint dSphs and a number of dwarf elliptical (dE) and dwarf irregular (dIrr) galaxies. And indeed, it has been suggested that some of the M31 satellites are associated with others and are orbiting in groups; just as we believe to be the case for certain MW satellites. NGC 147 and NGC 185, two dEs in the M31 satellite population, are falling in as a binary pair (van den Bergh, 1998); mirrored by the two dIrr Large and Small Magellanic Clouds (LMC and SMC respectively) which are in orbit around the MW. There is further evidence that Draco and Ursa Minor are also associated with the LMC/SMC system, as their elongations lie along the Magellanic Stream (Lynden-Bell & Lynden-Bell, 1995; Palma et al., 2002), and it appears that Fornax, Leo I, Leo II and Sculptor are also falling in as a group (Lynden-Bell, 1982), with Sextans also possibly associated with the group (Majewski, 1994). Further, Kroupa et al. (2005) found that the then-known innermost 11 satellites were all orbiting approximately in the same plane; Piatek et al. (2007) later showed that their proper motion measurements for Fornax took it out of this plane, similar data for the other satellites will confirm or disprove their associations.

In their discovery of Andromeda XXII (And XXII), Martin et al. (2009) noted that it lies closer in projection to M33 than M31 and suggested that it could be a satellite of M33 and de Jong et al. (2010) recently presented evidence that Leo IV and Leo V could be a bound "tumbling pair" falling into the MW. Such behaviour is not unexpected; Sales et al. (2007) postulate that outlying satellites on extreme orbits may have been part of an infalling pair; under certain conditions, when the pair interacts with the host, the heavier member of the pair maintains a bound orbit about the host but the lighter satellite is kicked out onto a high-energy orbit. And, in a dynamical analysis of galaxy formation, Li & Helmi (2008) found that nearly a third of the dark matter subhalos in their simulations were accreted in groups.

1 Introduction

A few years ago, there was also a suggestion that the M31 satellites showed a significant offset in that a good many of the then-known M31 satellites (McConnachie & Irwin, 2006b) appeared to be “on our side” (Trimble et al., 2007). However, subsequent satellite discoveries (of which there have been many) since then have redressed the balance and there are presently roughly equal numbers of satellites in front and behind M31 from our perspective so there does not appear to be any peculiarity there after all.

The GC populations of both galaxies however show some differences; as well as playing host to a considerable GC population much like that found in the MW, M31 also contains a small number of extended clusters (ECs, Huxor et al., 2005; Mackey et al., 2006) that are unlike any object found in the MW. These ECs are similar to GCs at first glance, they have similar colours and luminosities, however they are unusually extended (hence the name) with half-light radii of ~ 30 pc (instead of the $\lesssim 10$ pc expected for typical GCs). That no ECs have been found anywhere else outside of the MW is not very surprising as they are very sparse objects thanks to their large size - and, thus, difficult to detect - however it is curious that no such objects have yet been found in the MW. It is possible that Galactic surveys have simply missed those present in the MW as they are too close to the disks or bulge to be identified, or it could be that their presence indicates a difference in the formation history of the MW and M31. The nature of these objects is also a puzzle; their half-light radii place them neatly in the gap that separate the dark-matter-free GCs and dark-matter-dominated dSphs (see Section 1.4.3). Whether or not they contain dark matter will prove very interesting in determining what these objects are and may have implications for the theory of structure formation and our understanding of the nature of dark matter on these smallest scales.

The halo of M31 contains significant stellar substructure (see e.g. Ferguson et al., 2002) and has been very well studied in recent years in a series of projects. The newest of these is the Pan-Andromeda Archaeological Survey (PAndAS) study which is currently being conducted on the CFHT. The project will take data down to a surface brightness limit of 32 mags/sq.arcsec over three years and, at its completion, will have mapped the halo of M31 out to a projected radius of 150 kpc and the halo of M33 out to a projected radius of 50 kpc, covering over 320 deg² of sky in total, which corresponds to a volume of over 1.5×10^7 kpc³ (McConnachie et al., 2009). The map of the PAndAS first-year footprint is shown in Figure 1.3. With only one year of data, the full stretch of sky between M33 and M31 has been covered by the survey, revealing tidal distortions around M31 and M33; the most prominent is the GSS that protrudes from the bottom-left corner of M31 in the image. A number of satellite galaxies are also visible in the image, including two previously-undetected dSphs (Martin et al., 2009).

The metal-rich GSS was first detected by Ibata et al. (2001); M32 and NGC 205 were put forward as possible progenitors, however both candidates were later rejected. Instead the GSS progenitor is thought to have been a $\sim 10^9 M_{\odot}$ galaxy (Fardal et al., 2006) accreted in the last Gyr and completely destroyed by its passage through the M31 halo, leaving behind not only the GSS but also the north-eastern and western shelves as testament of its rather messy disruption (Fardal et al., 2007). Further simulations by Fardal et al. (2008) went on to show that a progenitor with a cold, rotating disk can best describe the observations, with a number of minor-axis streams, previously thought to be from an separate accretion event, now attributed to that disruption as well. Certainly the accretion of a single object can reproduced many substructure features of the M31 halo with remarkable accuracy.

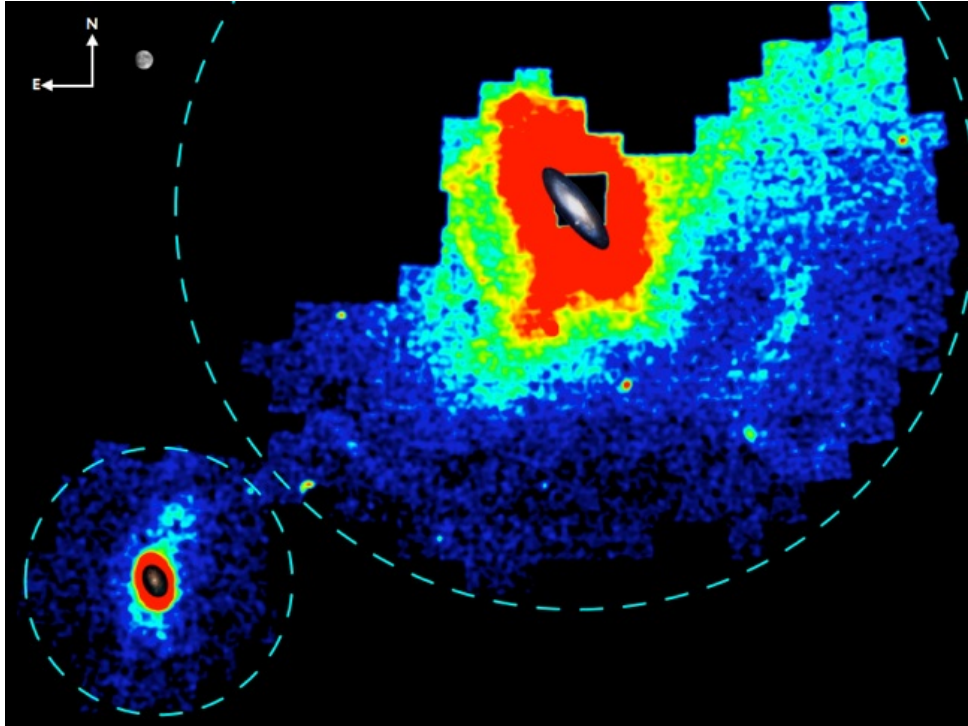


Figure 1.3: The halos of M31 and M33 as mapped by the The Pan-Andromeda Archaeological Survey (McConnachie et al., 2009). Only the first year of data is plotted here; by the end of the survey, the entire halo of M31 will be mapped out to 150 kpc, and that of M33 out to 50 kpc. Tidal distortion features are clear around both galaxies, the most prominent is the Giant Southern Stream that protrudes from the bottom left corner of M31 in this image. It is believed that M33 is the progenitor of this stream, and that the plume of stars extending out in the opposite direction can also be attributed to a recent passage of M33. Also visible in this image are a number of satellite galaxies.

The Spectroscopic and Photometric Landscape of Andromeda’s Stellar Halo (SPLASH) survey has also mapped parts of the M31 system by identifying and studying red giant branch (RGB) stars in fields scattered throughout the halo. Some of the fields have targeted structures of interest, such as the GSS (Gilbert et al., 2009), while some others have targeted M31 satellites (Kalirai et al., 2010). Determining whether an RGB star is bona fide member of M31 or whether it is a foreground contaminant in the MW requires a sensitive and sophisticated approach and the survey has been able to detect RGB stars out to a radius of ~ 165 kpc from the centre of M31 (Gilbert et al., 2006). With both spectroscopy and photometry they are able to study the kinematics and chemical abundances of the stars that they find, information that is vital if we are to understand the merger history and the evolution of M31’s halo.

Chapman et al. (2006) used data from the CFHT/MegaCam survey of M31 to show that most of its halo is formed from multiple kinematically-cold streams. Gilbert et al. (2009) then went on to use SPLASH RGB stars to identify cold kinematic substructure. They found that high-surface-brightness features are generally more metal rich than those of low surface brightness and they suggest that this is a natural consequence of the observed dwarf galaxy mass-metallicity relation (see e.g. Mateo, 1998) as large galaxies tend to be brighter and more metal rich. They also find a significant metallicity spread for a given surface brightness, which they suggest is due to the accretion time of progenitors and suggest that alpha enrichment, metallicity and surface brightness may be used to estimate the

1 Introduction

luminosity and time of accretion of the progenitor.

It is clear that M31 has a lot to tell us about the formation and evolution of structure in the Universe; both in its own right and when the results are used in concert with and in contrast to results from the MW.

1.4 Dwarf spheroidal galaxies

DSph galaxies are believed to be the most dark-matter dominated objects in the Universe and they are the smallest scales on which dark matter is found. GCs are apparently similar at first glance however closer study reveals that they are purely baryonic in nature. As dSphs are so dark-matter dominated, dark matter has heavily influenced their formation and evolution and, as such, they are an ideal test-bed for dark matter theories. If we can understand dark matter on these scales, then we can extend that knowledge to larger objects, this makes them incredibly valuable to study.

Furthermore, as structure formation in the universe is hierarchical, this makes dSphs the dark-matter building blocks of the universe and, thus, they are the first objects to form. This makes them some of the oldest systems in the Universe and host to some of the oldest stars. These primordial stars are essential for investigating the first stars that formed and reionized the Universe.

DSphs also contain some of the most metal-poor stars ($[Fe/H] \sim -5$) found in the LG; the Galactic halo also contains such stars but with far greater frequency, which is rather puzzling. That the dSphs should contain metal-poor stars is not surprising as they are very old systems that contain very old stars; these stars will have formed before any significant chemical enrichment of the interstellar medium (ISM) could have taken place and so they will be of very low metallicity. Given that the halo of the Galaxy has been formed from the continual accretion of dSph systems, we would expect to see a similar fraction of these stars in the halo as we do in the dSphs, brought in by accreted satellites. That this is not the case could indicate some fundamental difference between the early-accreted satellites that have built up the halo and those that are only now infalling into the MW.

1.4.1 Milky Way dwarfs

The study of MW dSph galaxies has increased dramatically over the past few years with the advent of the SDSS survey. Prior to 1990, there were seven MW dwarf galaxies known: Draco, Ursa Minor, Fornax, Carina, Sculptor, Leo I and Leo II. All of these were found by eye using photographic plates. In the next decade, two more dwarfs were added to the list: Sextans was found by automated search of photographic plates (Irwin et al., 1990) and Sagittarius was found kinematically from study of radial velocity data (Ibata et al., 1995). Before SDSS there were nine dwarf galaxies and the rate of discovery was one or two per decade.

These numbers were puzzling because CDM cosmology simulations (Klypin et al., 1999; Moore et al., 1999) predicted significant amounts of non-linear substructure and an order of magnitude more dark matter halos surrounding the Galaxy than were known to exist at that time (this is discussed in more detail in Section 1.1.3).

SDSS data paved the way for a wealth of new discoveries: Willman 1, Ursa Major I (both Willman et al., 2005), Canes Venatici I (Zucker et al., 2006), Boötes I (Belokurov et al., 2006), Ursa Major II

(Zucker et al., 2006; Grillmair, 2006), Coma Bernices, Canes Venatici II, Hercules, Leo IV, Segue 1 (all Belokurov et al., 2007), Leo T (Irwin et al., 2007), Boötes II (Walsh et al., 2007), Leo V (Belokurov et al., 2008), Segue 2 (Belokurov et al., 2009), Boötes III (Grillmair, 2009), Pisces I (or the Pisces Overdensity Watkins et al., 2009, see also Chapter 3), Pisces II and Segue 3 (both Belokurov et al., 2010). All of these objects have a low surface brightness that pre-SDSS surveys were simply unable to see, which explains why they have only been found now. It is unclear in some cases whether these satellites are dSphs or GCs - analysis is still ongoing to confirm their nature - and some detections are thought to be the unbound remnants of tidally-disrupted dSphs.

As the SDSS surveys covers only $\sim 20\%$ of the sky in total and most of the area covered is in the North Galactic Cap, it stands to reason then that there are many more dwarf galaxies out there which we are unable to see because we lack the resources to look as deep as the SDSS over the whole sky.¹

In an attempt to estimate the completeness of our MW satellite sample, Koposov et al. (2008) developed a satellite detection algorithm, which, when tested on a large set of mock SDSS Data Release 5 (DR5) data, returns the probability of finding a satellite of given surface brightness, size and heliocentric distance at any point on the sky. They find that all of the new discoveries lie close to the SDSS detection limit, explaining why they have been found now and not before. The results also suggest that the complement of satellites currently known is complete given the current detection limitations. There are regions of the sky where we should be able to see satellites; that there are no satellites known in these regions indicates that there are none to be found, not that we have missed them. They have also calculated the luminosity function for the MW satellite galaxies, accounting consistently and algorithmically for their detection biases.

The SDSS dwarfs are very metal-poor, like a lot of stars found in the halo, however the classical, pre-SDSS dwarfs lack any really metal-poor stars. This would imply that the new discoveries are a part of the old dwarf population from which the MW halo was first formed. The new dwarfs are less regular in shape than those previously known, indicating that tidal forces are at work and are an important consideration in any further study. It has also been found that there is a loose correlation between irregularity and distance.

1.4.2 M31 dwarfs

The story of the M31 satellite population is very similar to that of the MW. The past few years has seen a flurry of new dSph discoveries around M31², thanks to a number of surveys designed map the entire stellar halo of M31 in great detail. Before these surveys came along, the known dSphs were few and they were all similar to the MW classical dSphs. And, again like the MW, many (though not all) of the new dSphs have been small and faint.

¹This will soon change; there are a number of exciting programs coming online soon that will allow us to look at the whole sky with the same depth as the SDSS, and deeper in some cases; these are discussed in more detail in Section 6.2.2.

²It is worth noting here that naming conventions can sometimes be misleading when it comes to collating lists of M31 satellites. The galaxies are named for the constellation in which they are found and not the host galaxy; in most cases, these naming conventions would be one and the same, but for Andromeda IV and Andromeda VIII this is not true; both galaxies were originally thought to be dSphs in the vicinity of M31, however further study has showed that they lie outside the LG.

1 Introduction

van den Bergh (2006) compared the satellite populations of the MW and M31, concluding that they are statistically similar, however there are a couple of inconsistencies worth mentioning. All of M31's inner satellites are early-type objects, whereas the LMC and SMC, which exist in the inner parts of the MW halo, are late-type objects; they are predicted to have been formed outside of the MW and to have fallen in relatively recently. There is also some small difference in the dSph populations in that the M31 dSphs have half-light radii larger than their MW counterparts, an observation also made by McConnachie & Irwin (2006a), who noted that the M31 dSphs are larger than those of the MW for all absolute magnitudes by at least a factor of two. Whether this is due to observational bias affecting the sizes of galaxies we are able to detect or whether it hints that the MW dSphs have experienced greater tidal stripping is unclear; if it is due to differences in environment or orbit, then this could suggest that the tidal forces from the MW exceed those felt by a dSph in orbit of M31 at the same distance. The cumulative radial distribution of the combined satellite populations also shows a sharp drop at ~ 25 kpc, suggesting that the very innermost satellites might belong to a different population. This comes as no surprise given that the halo is very clearly a two-component system with the inner parts believed to have been formed by the rapid accretion of satellites and/or in situ processes and the outer part forming from the slow, continual merging of satellites; as has already been discussed at various points throughout this section. This is one piece of further evidence that appears to support this hypothesis.

Other results from the study by McConnachie & Irwin (2006a) include an apparent offset in the central surface brightness - luminosity relation for the two dSph populations, which is likely as a result of the size differences previously noted; and a correlation between central surface brightness and distance from the host for both populations, with brighter dSphs orbiting at larger radii. This latter point highlights the importance of environment in the evolution of dSphs, although the nature of the influence environment has is not clear. McConnachie & Irwin (2006b) also compared the MW and M31 satellite populations, finding the radial distribution of the M31 satellites to be more extended than those around the MW, with half of the MW satellites found within ~ 100 kpc, while for the M31 the corresponding median is ~ 200 kpc.

We can learn a lot about both dSphs and their host galaxies through the similarities and differences in the two populations. All of the differences appear to be due to environment and so investigating these will help us to better understand the hosts and how their properties affect their satellites. That the populations are in other ways so similar, gives us a large sample size to study and we can be confident that any conclusions we draw about dSphs are indeed universal, and not just a peculiarity of the MW population.

1.4.3 Comparison with star clusters

DSphs are often discussed along with star clusters and they are, superficially, very similar, with the star clusters simply being smaller versions of the dwarfs. However, when we look more closely, we discover that these objects are not so similar at all.

Together, they describe a bimodal distribution in half-light radius with stable clusters typically found with $r_h < 30$ pc and stable dwarfs having $r_h > 120$ pc (see e.g. Gilmore et al., 2007). However, despite this clear dichotomy in size, their luminosities are remarkably similar with both dSphs and

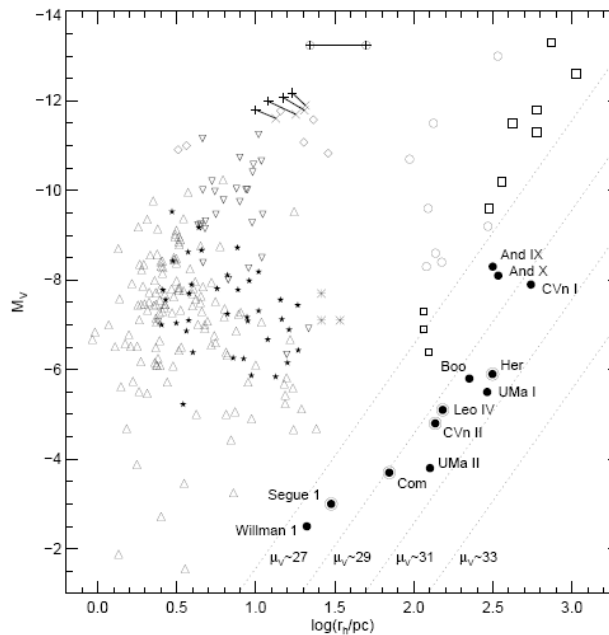


Figure 1.4: Location of different classes of object in the plane of absolute magnitude versus half-light radius (from Belokurov et al., 2007).

GCs spanning over six orders of magnitude in stellar luminosity, from the brightest objects with $L \sim 10^9 L_\odot$ ($M_V \sim -15$) to the faintest with $L \sim 10^3 L_\odot$ ($M_V \sim -4$). This is illustrated clearly in Figure 1.4, which shows dSphs and GCs in the plane of absolute magnitude and half-light radius (Belokurov et al., 2007). With each new dwarf discovered it is becoming increasingly apparent that there is a gap between $30 < r_h < 120$ pc which remains largely unpopulated, even as the numbers of known clusters and dwarfs continue to increase. It is not uncommon for some of the new, ultra-faint discoveries to sit in the gap when a preliminary analysis is performed, however more detailed investigation with improved data has always, thus far, corrected the half-light radius estimate to shift the object to one side or the other. The only exception to this is a handful of curious objects discovered in recent surveys of M31's stellar halo; called extended clusters, by virtue of the fact that they are very similar to GCs in everything but their larger size, they fit nearly into the gap. Perhaps most intriguingly of all, they have no known analogue in the MW.

For dwarfs and clusters with the same velocity dispersion and luminosity, the dwarfs are considerably larger than the clusters; the virial theorem then implies that there must be an extra massive component to the dwarfs that we can't see: dark matter. This was first noted by (Aaronson, 1983) in a study of the internal kinematics of Draco; he found the mass-to-light ratio to be much bigger than would have been expected if the dSphs were simply scaled-up versions of the GCs. Subsequent observations of other dSphs have gone on to strengthen this result. Indeed, it appears that, dSphs are the most dark-matter-dominated objects in the universe. It should be noted that the presence of dark matter in these objects is not wholly agreed upon. For example, Kroupa et al. (2005) argue that the shape of the observed distribution of MW satellites is inconsistent, at the $3\text{-}\sigma$ confidence level, with models for a cosmological substructure population. They conclude that most of the MW satellites cannot be related to dark-matter-dominated satellites. However, it is generally believed that these

1 Introduction

objects do contain dark matter (and a lot of it). Whether or not the ECs contain dark matter is a topic of some debate.

There are further differences between dSphs and GCs. van den Bergh (2008) showed that, on average, dSphs are flatter than GCs, with GCs suspected to be dSph cores having an intermediate flattening; they suggest that this may be an alternative way of distinguishing between the two classes of object.³

1.4.4 Dwarf properties

DSphs are believed to be the building blocks of structure in the universe, the basic elements from which larger structures are formed. It would be natural, then, to assume that they are simple systems, however, this is certainly not the case. They are complex systems with complex and varied SF and chemical enrichment histories governed by processes that we do not yet fully understand; what is certain, though, is that SFH and chemical evolution are inextricably linked (Hodge, 1989).

Section 1.4.3 has already touched on the fact that dSphs span over six orders of magnitude in stellar luminosity, this makes them incredibly useful in the study of how fundamental parameters (such as DM content, ISM properties and SFH) change with luminosity. It is also apparent that metallicity changes with luminosity, with the more luminous dSphs being more metal rich than those of low luminosity (Aaronson, 1986); another consequence of this is that the low-luminosity dSphs contain a lot of primordial material that is essential if we are to study the early universe.

Star formation in dSphs is believed to take place in a series of short-period bursts; the exact details are governed by feedback and cooling processes, which are topics of active research and are still not fully understood. There is also evidence that pericentric passage of dwarf around its host can trigger a star formation episode. It is apparent that every dwarf has a unique SFH as each has a unique orbit and will have unique internal properties that drive SF. Some dwarfs show periods of SF throughout their lifetimes, from very early times right up until the last Gyr or so, while some appear to have had very little recent SF, making all of their stars at ancient times.

For example, Aparicio et al. (2001) found the stellar population of Draco to be primarily made up of old stars, with a small intermediate age population also present. They concluded that as much as 90% of the SF in Draco occurred more than 10 Gyr ago, with no SF in the last ~ 2 Gyr. Ursa Minor appears even older still, with more than 90% of its SF happening more than 13 Gyr ago, and with no SF in the last 10 Gyr (Carrera et al., 2002). Fornax, however, has the most complex SFH yet seen in a dSph, with multiple bursts of SF throughout its lifetime; while an old population is present, it contains a significant intermediate-age population and appears to have experienced an episode of SF $\sim 3 - 4$ Gyr ago (Coleman & de Jong, 2008). Carina too, has shows multiple SF bursts with a dominant intermediate-age population; Hurley-Keller et al. (1998) concluded that Carina formed over 50% of its stars ~ 7 Gyr ago and 30% ~ 3 Gyr ago, thus forming only 10%-20% of its stars at early times.⁴

And yet, despite the variety shown in their SFHs, their metallicities and their luminosities, dSphs share a remarkable feature: they all inhabit dark halos of the equal mass. In a study of the kinematics

³In the same paper, they also show that the flattening of the MW and the M31 dSph populations are statistically similar.

⁴Somewhat curiously, despite a number of dSphs showing clear indications of recent SF, there is little gas present that could fuel such episodes (Mateo, 1998).

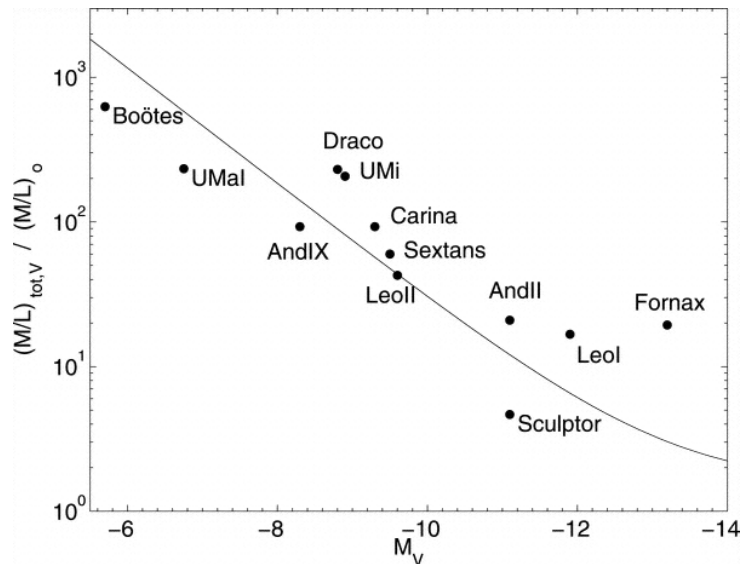


Figure 1.5: The graph shows mass-to-light ratios versus absolute magnitudes for a number of LG dSphs. The solid line describes a constant dark-halo mass (from Gilmore et al., 2007).

of Carina, Mateo et al. (1993) compared their results to those of the other then-known MW dSphs and observed that the absolute magnitudes and mass-to-light ratios implied a common dark matter halo mass of $\sim 2 \times 10^7 M_\odot$. Cote et al. (1999) demonstrated that this result also applied to M31 satellites in a study of Andromeda II (And II). In the intervening decade, many more dSphs have been discovered and a number of those have had mass-to-light ratios determined, enabling their dark halo mass to be deduced. Despite extending the ranges of both the absolute magnitudes and the mass-to-light ratios by at least an order of magnitude, the dSphs continue to show the same trend. Such analyses as these are generally done assuming that the dSph is in dynamical equilibrium, which is certainly not the case for dSphs that are being tidally disrupted; however, Cote et al. (1999) also show this to be a sound assumption as they find that the tidal field from the host galaxy does not upset the internal equilibrium.

Perhaps, even more remarkable than the existence of a common halo mass, are the recent results suggesting that the dSph mass profiles are identical also. Gilmore et al. (2007) suggested that dark matter forms cored mass distributions with core scale lengths of ~ 100 pc and that their maximum central mass density falls within a narrow range. In an analysis of the resilience of dSph galaxies to tides, Peñarrubia et al. (2008) found that, despite a large range in luminosity, the halos of dSphs span a very narrow range in peak circular velocity (or mass). They estimated that dSph halos may be universally well-approximated by an NFW profile with parameters $r_s = 2.0$ kpc and $v_{\max} = 28.6$ kms^{-1} . Strigari et al. (2008) showed that the mass enclosed within 300pc (M_{300}) is the same for all dSphs. This result is certainly noteworthy for the larger, classical dSphs that extend out to 300 pc and beyond but seems somewhat nonsensical, for the smaller, ultra-faint dSphs; they have half-light radii only a fraction of this size and thus their masses at 300pc must be extrapolated and, in some cases, the extrapolation is quite large. Walker et al. (2009) found a much stronger result, finding that the mass enclosed is the same at *all* radii, not only as this somewhat arbitrary distance of 300 pc. This strongly suggests that not only are the total masses of the dSphs universal, their mass profiles are as

1 Introduction

well.

The form of that profile is harder to pin down. They tried fitting four different halo models, including both cored and cusped profiles and were able to find adequate fits in each case. However, they also found that for all well-observed dSph galaxies, the possible mass profiles intersect near the half-light radius regardless of the assumed velocity anisotropy β . Thus, they conclude that the mass at r_h is insensitive to β , a conclusion supported by the results from Wolf et al. (2010), who first argued that there should be a radius at which the mass estimated is independent of the assumed velocity anisotropy β and then went on to show that this radius does exist and it is close enough to the half-light radius so that the mass within the half-light radius is very nearly insensitive to the anisotropy. This is very useful, as we can be confident of estimating reasonable estimates if we calculate them in this way, even though we are not yet certain of the exact form of the dark-matter profiles and cannot yet break the mass-anisotropy degeneracy.

Unlike the dark-matter halos, the luminous components of dSphs show great variation, as evidenced by the large range of sizes and surface brightnesses that have been deduced for these objects. It is clear, then, that the luminous profiles are different from the dark matter profiles. King (1962) profiles provide the best fits to data, however exponential and Plummer profiles can also be found to fit the data, if less well (see e.g. McConnachie & Irwin, 2006a). There is also increasing evidence that some dSphs contain a secondary core component: notably Sculptor (Tolstoy et al., 2004) and Sextans (Kleyna et al., 2004) in the MW and And II (McConnachie & Irwin, 2006a) in M31.

This section only touches upon some of the properties of dSphs that make them so intriguing and so valuable to study; although their detection and their study can be difficult, thanks to their low surface brightnesses and their extended nature. For a more in depth discussion, Mateo (1998) presents an excellent review of the topic of LG dwarf galaxies; despite being now 12 years old, and written at a time when only a handful of dSphs were known to exist around the MW and no hint of the UF dSphs had been seen, it remains remarkably relevant.

1.5 Tracer Populations in the Local Group

Many studies of objects in the LG (galaxies, clusters, structures and substructures) are done indirectly using tracer populations. We cannot directly see dark matter, we cannot directly determine where it is or measure how fast it is moving, and we certainly cannot collect up all of the dark matter and put it on an enormous set of scales; instead we can only infer its existence by its influence on objects that we *can* see and we can estimate its properties by quantifying the nature of that influence. The satellite galaxies of the MW and M31 make excellent tracer populations for examining the broader properties of their host galaxies, such as mass or profile shape, as they are found far out beyond the detectable limits of the stellar halos, so we are able to probe the region where dark matter dominates and where no stellar tracers exist. For the study of the galaxy halos, there are a number of widely used tracers, mostly stellar in nature, although the dwarfs and clusters can also be of some use, as can HVCs and planetary nebulae (PNe); tracers should ideally be easily identified and selected photometrically so that samples can be compiled and used without too much effort, and tracers that are bright and reasonably common have the great advantage of being seen out to large distances and being present in

any substructure we might wish to study. Various types of variable star make for excellent tracers as candidates can be selected reasonably straightforwardly using colour cuts and their absolute magnitudes can be determined with reasonable accuracy allowing for reliable distance estimates; popular and bright variables, such as Cepheids and RR Lyraes, are very widely used.

In this thesis, I describe how various tracer populations can be used to probe the structure of the MW halo, determine the masses of the MW and M31 and probe the nature of the MW and M31 satellite populations. The thesis is organised as follows:

- Chapter 2 describes *Variable stars in SDSS Stripe 82*. I begin by describing the SDSS in some detail, then go on to describe the region known as Stripe 82 and why it is so useful for studies of variability. Finally, I describe a catalogue that has recently been compiled by Bramich et al. (2008) in order to best exploit the Stripe 82 data and explain how I used the catalogue to select a subset of variables.
- Chapter 3 concerns *Substructure revealed by RR Lyraes in SDSS Stripe 82*. I use the set of variable stars selected in Chapter 2 to select RR Lyrae candidates and then describe how these candidates were cleaned of contaminants and how periods, absolute magnitudes and metallicities were calculated for the cleaned sample. Finally, I use the RR Lyraes to identify substructures in the Galactic halo, which includes the discovery of a new object in the halo which we call the *Pisces Overdensity*, and I analyse the distribution of RR Lyraes throughout the halo.
- Chapter 4 estimates the *Masses of the Milky Way and Andromeda galaxies*. I use the satellite populations of the MW and M31 in order to estimate the masses of their respective hosts using a tracer mass estimator. This chapter expands on previous work by including the plethora of recent discoveries that were not known when the last study of this type was carried out; further, it also uses a more sophisticated version of the tracer mass estimator which uses actual radii instead of projected radii and allows for the inclusion of proper motion data, where it exists.
- Chapter 5 describes the *Application of the Timing Argument to host-satellite systems*. Previously, the Timing Argument has been widely used to estimate the mass of the LG by considering the common orbit of the MW and M31, and has been recently used to estimate the mass of the MW by analysing the MW-Leo I system. This chapter describes adaptations to the method that enable its application to two external galaxies and I go on to estimate the mass of M31 by applying the adapted method to the M31-Andromeda XII and M31-Andromeda XIV systems. I also discuss the probability of finding satellites with properties similar to And XII and And XIV.
- Chapter 6 presents *Discussion & Conclusions* for the work described in the thesis and looks towards the future.

2

Variable stars in SDSS Stripe 82

In Aristotle's model of the Universe, the stars were fixed on a rotating sphere and eternally invariable. Stellar variability has been known since Fabricius' discovery of Miras in 1596, although the ancient Chinese and Korean astronomers were already familiar with supernovae or "guest stars" (Clark & Stephenson, 1977). Proper motions were discovered in 1718 by Edmund Halley, who noticed that Sirius, Arcturus and Aldebaran had moved from their fixed positions recorded in Aristotelian cosmology.

Despite this long history, our knowledge of both variable stars and high proper motion sources remains very incomplete. As Paczyński (2000) has emphasised, over 90 per cent of variable stars brighter than 12 mag have not been discovered. There are still comparatively few large archives of variable sources and, as a consequence, our knowledge of many classes of object, including novae, supernovae, RR Lyraes (the focus of this chapter) and high proper motion objects remains limited. Indeed, the variable sky remains one of the most unexplored areas in astronomy, with the exciting possibility that even bright variable objects may correspond to completely unknown astronomical phenomena (see e.g., Paczyński, 2001).

The modern era of massive variability searches begins with the microlensing surveys like MACHO (Alcock et al., 1993), EROS (Aubourg et al., 1993) and OGLE (Udalski et al., 1992). Typically, these surveys monitored millions of stars down to $V \sim 21$ a few times every night over several years in the directions of the Galactic Bulge and the Magellanic Clouds. The resulting huge databases of lightcurves yielded information on many rare types of astrophysical variability. They were the first projects that harnessed the power of large format CCD cameras and modern computers to show that the acquisition, processing and archiving of millions of photometric measurements was feasible. The surveys were soon followed by high-redshift supernova surveys (such as High-Z SN Search (Schmidt et al., 1998) and the Supernova Cosmology project (Perlmutter et al., 1999)), which typically had a lower time resolution and smaller area coverage than the microlensing surveys, although much deeper limiting magnitudes.

The Sloan Digital Sky Survey (SDSS; York et al., 2000) came next, providing deep and homogeneous photometry in five bands in a large area around the North Galactic Cap, but with almost no

2 Variable stars in SDSS Stripe 82

variability information. The main exception is the compilation of repeat scans of the ~ 290 square degree area – known as Stripe 82 (see e.g., Adelman-McCarthy et al., 2008). The dataset has allowed the discovery of many new supernovae, which are publicised and followed up spectroscopically with other telescopes (see e.g., Frieman et al., 2008; Dilday et al., 2008). By averaging repeat observations of unresolved sources in Stripe 82, Ivezić et al. (2007) built a catalogue of 1 million standard stars with r magnitudes between 14 and 22. Sesar et al. (2007) then carried out the first analysis of ~ 1.4 million variable stars and quasars using a colour-colour plot to assign variable types.

More recently, Bramich et al. (2008) presented a Light-Motion-Curve Catalogue (LMCC) containing almost four million “light-motion curves” using the data available in Stripe 82, along with a Higher-Level Catalogue (HLC) which is a set of 229 derived quantities for each light-motion-curve. These catalogues are, by design, very well suited to the identification and analysis of variable stars in Stripe 82.

In this chapter, I present work carried out to select and analyse variable stars from the SDSS Stripe 82 data, using the Bramich et al. (2008) catalogues. Section 2.1 describes the SDSS and Stripe 82 in more detail and gives a summary of the Bramich et al. (2008) catalogues that I use for this analysis. In Section 2.2, I discuss the selection of the variable objects and their properties, and Section 2.3 compares the set of variable I extracted with the sample described in Sesar et al. (2007). I summarise in Section 2.4.

2.1 The Sloan Digital Sky Survey

There can be no doubt that the Sloan Digital Sky Survey (SDSS, York et al., 2000) has been one of the most significant and most important in recent years. Remarkable in both depth and extent, it has been an incredibly powerful tool for probing the universe, starting in our own back yard and extending out into the furthest reaches of the cosmos.

The survey is conducted using a dedicated 2.5m telescope at the Apache Point Observatory in New Mexico, which houses two special-purpose instruments: the first, a 120 megapixel optical camera capable of imaging 1.5 square degrees of the sky in a single observation; and the second, a pair of spectrographs fed by optical fibres capable of taking spectra (and hence enabling distance determination) for more than 600 galaxies and QSOs in a single observation. Imaging data are collected simultaneously in each of five photometric bands, u , g , r , i and z (Fukugita et al., 1996; Gunn et al., 1998; Hogg et al., 2001; Gunn et al., 2006; Adelman-McCarthy et al., 2008) and are then processed by a custom-designed software pipeline to measure astrometric and photometric properties (Lupton et al., 1999; Stoughton et al., 2002; Smith et al., 2002; Pier et al., 2003; Ivezić et al., 2004).

This rather clinical description cannot begin to encompass the wealth of data and the incredible impact the survey has contributed to all areas of astronomy and cosmology.

The first phase of the survey, SDSS-I, was completed in June 2005; over the preceding five years the SDSS telescope imaged over 8 000 square degrees (roughly a quarter of the sky), gathering data for more than 200 million objects, including spectra for 675 000 galaxies, 90 000 quasars and 185 000 stars. The data comprises observations of a plethora of different objects, from nearby asteroids to the most distant quasars, and all manner of resolved and unresolved stellar populations in between.

2.1 The Sloan Digital Sky Survey

Following the completion of the first phase of data collection, the second phase, SDSS-II, began; it consisted of three distinct surveys:

1. The *Sloan Legacy Survey* whose primary task was to complete the original SDSS imaging and spectroscopic goals with the hope that the position and distance information obtained would allow researchers to probe the postulated filamentary nature of the large scale structure of the Universe. The final dataset comprised photometry for 230 million objects over 8 400 square degrees of the sky and spectra for 930 000 galaxies, 120 000 quasars and 225 000 stars.
2. The *Sloan Extension for Galactic Understanding and Exploration (SEGUE)* whose driving goal was to map the structure and stellar make-up of our Galaxy with a view to better understanding its formation and subsequent chemical and dynamical evolution. The SDSS was originally designed as an extra-galactic survey, thus the imaging was taken at high latitudes to avoid as much Galactic contamination as possible, particularly contamination from the Galactic plane. Despite this focus, the survey proved to be revolutionary for studies of the local universe as well, in particular in finding new, faint dwarf galaxies in orbit around the MW. In order to better understand the MW itself, SEGUE sought data from previously-avoided parts of the sky, taking 3 500 square degrees of new photometric data and spectra for 240 000 stars - mainly from fields through the Galactic plane but also from fields concentrated on areas of interest, such as the Sagittarius tidal stream.
3. The *Sloan Supernova Survey*, which aimed to find and analyse hundreds of type IA supernovae, and with them to investigate the expansion history of the universe. The survey repeatedly imaged a 300-square-degree field in the South Galactic Cap over the three months for which it was visible; the repeated nature of the data was obviously vital for the identification of variable stars and supernovae. This survey was particularly important because it aimed to find supernova in the redshift range 0.1-0.4, thus bridging the gap between local- and high-redshift surveys.

Now the survey has moved into its third phase, SDSS-III, which will continue until 2014. This phase will pursue three broad themes - dark energy and cosmological parameters; the structure, dynamics, and chemical evolution of the MW; and the architecture of planetary systems - in four distinct projects:

1. The *Baryon Oscillation Spectroscopic Survey (BOSS)* will measure the characteristic length scale of the universe (a result of primordial baryonic acoustic oscillations) by mapping the spatial distribution of luminous galaxies and quasars.
2. *SEGUE-II* aims to extend the SEGUE survey from SDSS-II by doubling the number of targets that survey covered. The combined datasets will be used to probe the structural, kinematical and chemical history of the Galaxy's outer disk and halo and the small-scale distribution of dark matter.
3. The *APO Galactic Evolution Experiment (APOGEE)* will study the chemo-dynamical properties of the innermost parts of our Galaxy that are hidden to optical telescopes; it will require high-resolution, high signal-to-noise infrared spectroscopy in order to penetrate the obscuring dust.

2 Variable stars in SDSS Stripe 82

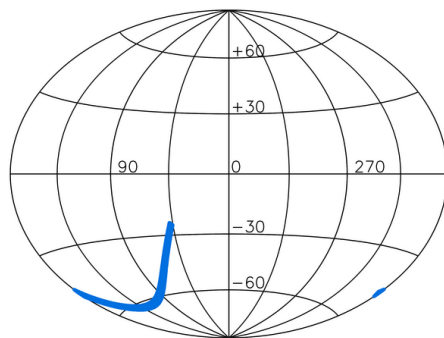


Figure 2.1: SDSS Stripe 82 coverage in Galactic coordinates.

4. *Multi-object APO Radial Velocity Exoplanet Large-area Survey (MARVELS)* aims to detect giant gas planets by monitoring the radial velocities of thousands of stars. Such a sample of planets will be vital for testing theoretical models of planet formation and evolution.

The variety of the second- and third-phase extension surveys highlights just how many fields the SDSS has impacted: for example, many faint new dwarf galaxies have been discovered around the MW, Einstein's prediction of cosmic magnification has been confirmed, the survey has observed the largest known structures in the universe that are more than a billion lightyears across and the survey has also studied multiple galaxy mergers.

The SDSS is unparalleled. Previous surveys of this nature were done photographically, however the SDSS uses electronic detectors which makes it is both more sensitive and more accurate; and the extent of the SDSS is also far greater than any previous survey. Of course, it is inevitable that the SDSS will eventually be superseded and I discuss some upcoming wide-field, all-sky surveys in Section 6.2.2.

2.1.1 SDSS Stripe 82

A survey of such large extent comes at a cost, however; in order to survey such large swathes of the sky, repeat observations are necessarily sacrificed. As a result, there is very little variability information available, making the deduction of proper motions and the determination of variable stars nigh impossible.

The exception to this is Stripe 82: a single strip of data in the Southern hemisphere, spanning from 20^h to 4^h in right ascension and from $-1^\circ.25$ to $1^\circ.25$ in declination (the sky coverage is shown in Galactic coordinates in Figure 2.1). This stripe was repeatedly imaged between June and December from 1998 until 2005; thus providing a dataset for which the number of good observations is high for a large fraction of the data. On average, objects in the Stripe have been observed 20 - 30 times, although some objects have as many as 80 observations recorded. The high number of observations that exist for these objects make the Stripe ideal for the study of variability and proper motions.

In order to better exploit this dataset, Bramich et al. (2008) compiled two catalogues: the first, the Light-Motion-Curve Catalogue (LMCC) which contains light-motion data for all stars and galaxies in the Stripe; the second, the Higher-Level Catalogue (HLC) which is a set of 229 derived-quantities for

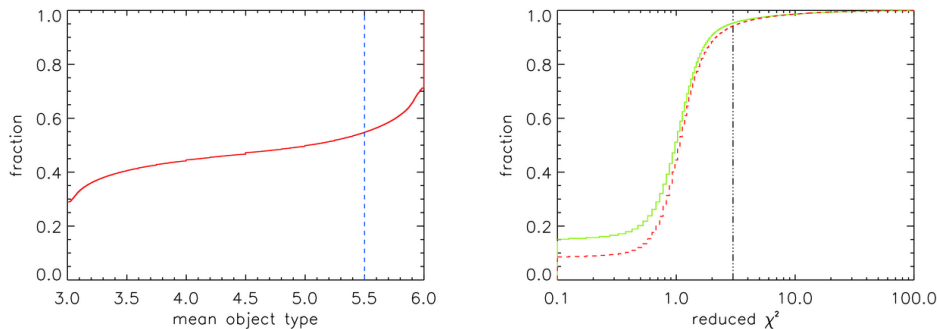


Figure 2.2: Left: Cumulative distribution of mean object type in the HLC. Galaxy-like objects are assigned an object type of 3 and star-like objects are an object type of 6. For multiple observations, the mean indicates whether the object is mostly classified as a star or a galaxy. The cut used to define the stellar sample is shown as a dashed vertical line. Right: Cumulative distribution of reduced χ^2 for g (green, solid) and r (red, dashed) bands for all stellar objects. The slope of the distribution turns over at a reduced χ^2 value of ~ 3 , which is taken as the boundary separating constant and variable stars; this value is marked on the graph as a dash-dot line.

each light-motion-curve in the LMCC. To create the LMCC, objects were matched between successive epochs, taking into account the effects of any proper motion over the eight-year baseline stretching back to the earliest runs in 1998. Thanks to the high quality of the SDSS imaging, excellent astrometric and photometric precision is attainable. The quantities contained within the HLC describe the mean magnitudes, photometric variability and astrometric motion of a subset of objects whose light-motion-curve entries pass certain quality constraints.

As well as having the potential to be an excellent source of variable stars, the Stripe has a further point of interest; two known halo substructures - the Sagittarius Stream (see e.g. Belokurov et al., 2006) and the Hercules-Aquila Cloud (Belokurov et al., 2007) - cross the Stripe. There is much that remains unknown about both of these objects so the Stripe 82 data is a valuable resource if we are to shed some light on their nature and properties.

2.2 Variable Stars in Stripe 82

2.2.1 Variable Selection

The HLC contains 3 700 548 objects. Every object in the survey is assigned an object type each time it is observed: 3 if it is galaxy-like and 6 if it is star-like (see § 3.1 of Bramich et al., 2008). For multi-epoch data, the object type averaged over all the observations provides a relatively reliable indicator of whether the source is star-like or galaxy-like. The cumulative distribution of mean object type in the left panel of Figure 2.2 shows that ~ 55 per cent of objects in the catalogue are purely star-like or purely galaxy-like. To extract a sample of stars with essentially zero contamination from galaxies, we require that the mean object type is 5.5 or greater. This results in a “stellar” sample of 1 671 582 objects.

For the stellar sample, a cumulative distribution of reduced χ^2 (that is, χ^2 per degree of freedom) for the g and r bands is shown in the right panel of Figure 2.2. The value of reduced χ^2 at which the

2 Variable stars in SDSS Stripe 82

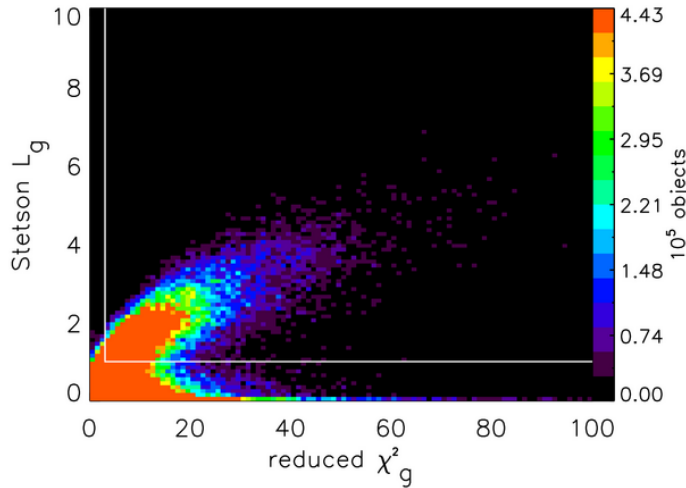


Figure 2.3: Density plot of reduced χ^2_g against Stetson index L_g for the stellar catalogue. Pixel colour represents the number of objects in each pixel bin. The cuts used to extract the high-quality sample of stellar variables are shown as white lines.

distributions turn over is ~ 3 , which is taken as the χ^2 -value below which stars are assumed to be well-modelled by a constant baseline. The number of objects that simultaneously satisfy reduced $\chi^2 > 3$ in both g and r is 41 729.

The stars with reduced $\chi^2 > 3$ in both g and r bands are mainly variables, but still contain some artifacts, typically due to one or two outlying photometric measurements. One way to test for true variability is to look for correlations between different bands; a true variable star will usually have changes in brightness that are correlated in all bands whereas a discordant measurement may exist in one band only. Throughout this analysis, the Stetson index (L_g) is used as a measure for correlated variability between the g and r band data (see Stetson, 1996).

For the stellar sample, a density plot of reduced χ^2 in the g band against the Stetson L_g is shown in Figure 2.3, in which two distinct populations can be discerned. The first has an almost linear correlation between reduced χ^2 and L_g , and are almost all true variable stars. The second has a high reduced χ^2 , but L_g is low, indicating that the brightness changes which give rise to the high reduced χ^2 values are not correlated between bands. To extract a sample of high-quality variable stars, we impose the simultaneous restrictions $L_g > 1$, reduced $\chi^2_r > 3$ and reduced $\chi^2_g > 3$, together with requiring at least 10 good epochs (see Bramich et al., 2008), leaving 21 939 objects. We present a comparison of the content of our variable catalogue with the earlier catalogue of Sesar et al. (2007) in Section 2.3.

To show the quality of the data, a selection of folded light-motion curves are shown in Figure 2.4, from which a variety of periodic phenomena such as stellar variability and eclipses are evident. In particular, the two right-most images in the middle row are very likely RR Lyrae. From the periods and the lightcurve shapes, we might surmise that the first lightcurve is an ab-type RR Lyrae and the second is a c-type RR Lyrae.

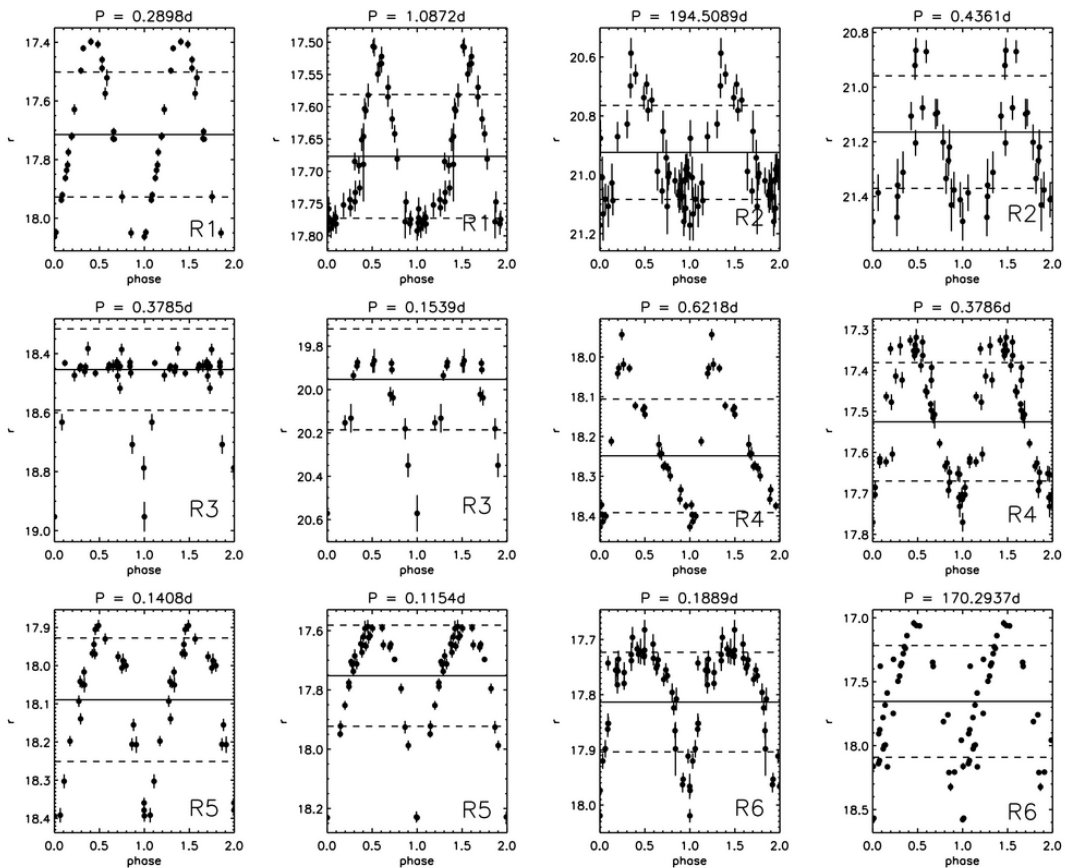


Figure 2.4: A sample of folded lightcurves. The period in days is recorded at the top of each plot. The solid line is the mean magnitude, whilst the dashed lines represent 1σ deviations. In the bottom right corner, the number refers to the region in the colour-colour plot in which the lightcurve lies (see Figure 2.7). The two rightmost lightcurves in the middle row are probable RR Lyraes.

2.2.2 Variable Properties

Colour-magnitude diagrams (g versus $u - g$) are plotted for both the stellar sample with u band data and the subset of variable stars, in Figure 2.5. For the stellar sample, we see three prominent clumps associated with the thin disk, thick disk and halo on moving redwards in colour. For the variables, there is one prominent clump centred on $u - g \approx 0.2$, which is primarily associated with variable quasars. There are less prominent, but still discernible, peaks associated with variable stars in the thin disk, thick disk and halo.

A crude discrimination between different classes of variable objects is possible in $g - r$ versus $u - g$ space. We find that the variable sample is largely comprised of stellar locus stars and low-redshift quasars; stellar locus stars are predominant at bright ($g < 19$) magnitudes while low-redshift quasars dominate at faint ($g < 22$) magnitudes. RR Lyraes also make a significant contribution (see Section 2.3 for more detail on the statistical properties of the variable sample).

2 Variable stars in SDSS Stripe 82

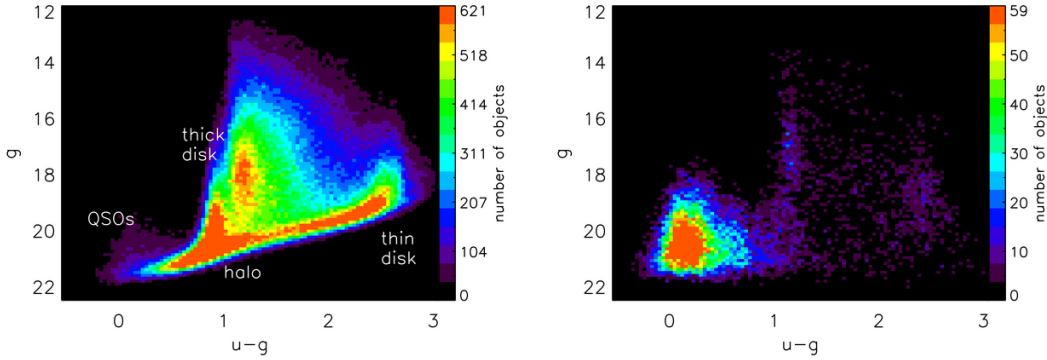


Figure 2.5: Left: Colour-magnitude diagram (g versus $u - g$) for all 527 621 sources in the stellar sample for which high-quality u and g data exist. Right: Colour-magnitude diagram (g versus $u - g$) for the subset of 21 939 variables.

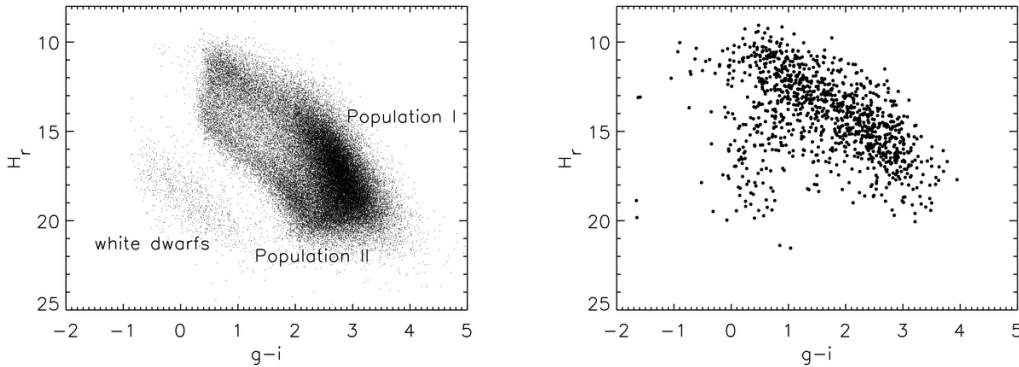


Figure 2.6: Left: Reduced proper motion diagram for all objects in the HLC with proper motion of $S/N > 10$ and $|\mu| > 2 \text{ mas yr}^{-1}$. Right: Reduced proper motion diagram for all objects in the variable subset with $S/N > 5$ and $|\mu| > 2 \text{ mas yr}^{-1}$.

2.2.3 The Proper Motions

The HLC offers an improvement over previous variability work in Stripe 82 through the availability of proper motions. The combination of stellar photometry and proper motions has proved to be a powerful way of classifying stars – in particular, members of elusive populations such as white dwarfs, brown dwarfs and wide binaries. Such combined catalogues, drawn from the intersections of SDSS data with USNO-B data (Monet et al., 2003), have been constructed before (Munn et al., 2004; Gould & Kollmeier, 2004; Kilic et al., 2006). Compared to such catalogues, the HLC is restricted to Stripe 82 and the proper motion sensitivity is poorer, due to the much shorter time baseline. On the other hand, the Stripe 82 photometric catalogue extends approximately 1.5 magnitudes deeper than the limiting magnitude of USNO-B proper motions ($V \sim 21$).

The reduced proper motion is defined as $H = r + 5 \log \mu + 5$, where r is the apparent magnitude and μ the proper motion in arcsec yr^{-1} . The criteria for inclusion in the reduced proper motion diagram in the left panel of Figure 2.6 are that the object lies in our stellar sample, that the proper motion is measured with a signal-to-noise ratio (S/N) > 10 and that the absolute value of the proper

2.3 Comparison with other variability surveys in Stripe 82

motion $|\mu|$ exceeds 2 mas yr^{-1} . The S/N-cut has been chosen primarily to ensure easy visibility of structure on the figure, whilst the proper motion cut enables us to excise quasars. We discern three distinct sequences of stars, namely Population I disk dwarfs, Population II main sequence subdwarfs and disk white dwarfs. Vidrih et al. (2007) have used this reduced proper motion diagram to identify new ultra-cool and halo white dwarfs in Stripe 82, Similarly, Smith et al. (2009) and Smith et al. (2009) have used the same procedure to extract a sample of halo subdwarfs in studies of the velocity ellipsoid and halo substructure. The right panel of Figure 2.6 shows the reduced proper motion diagram just for the subset of variables with proper motion $\text{S/N} > 5$ and $|\mu| > 2 \text{ mas yr}^{-1}$. The variables are disproportionately drawn from the Population I disk dwarfs, although the other two sequences can still be seen.

2.3 Comparison with other variability surveys in Stripe 82

Ivezic et al. (2007) constructed a catalogue of one-million standard stars with r magnitudes 14.0-22.0, by averaging repeated observations of unresolved sources in the 290 deg^2 area of Stripe 82. Sesar et al. (2007) used the catalogue to carry out the first analysis of variability in Stripe 82. In particular, they applied cuts $\chi_r^2 > 3$ and $\chi_g^2 > 3$, followed by the requirement that the root-mean-square scatter exceeded 0.05 mag , to identify variability, obtaining a catalogue of 20 533 variable sources.

The Bramich et al. (2008) light-motion curve catalogue (LMCC) is based on observations of Stripe 82 restricted to a smaller area of 249 deg^2 , extending in right ascension from $20.7^{\text{h}} < \alpha < 3.3^{\text{h}}$ with a width $2^{\circ}52$ in declination from $\delta = -1^{\circ}26$ to $1^{\circ}26$. We extracted a sample of high-quality variable stars from the LMCC by imposing the restrictions that: i) $\chi_r^2 > 3$ and $\chi_g^2 > 3$, ii) a cut on the Stetson index $L_g > 1$, iii) at least 10 good epochs are retained, giving a catalogue of 21 939 variable objects. Applying the cuts from Sesar et al. (2007) to our catalogue gives 22 483 objects, with $\approx 80\%$ in common with our subsample based on Stetson index cuts. Even though the Sesar et al. (2007) cuts give more candidates, the additional objects possess variability in different passbands that is not well-correlated.

Sesar et al. (2007) used a colour-colour plot to discriminate between different classes of variable objects. In Figure 2.7, our stellar subsample is plotted in $g - r$ versus $u - g$ and $r - i$ versus $g - r$. Here, following Sesar et al. (2007), the $g - r$ versus $u - g$ plot is divided into six regions, and labelled according to possible occupants: white dwarfs (the red-coloured Region 1), low-redshift quasars (the orange-coloured Region 2), M dwarf/white dwarf binaries (the green-coloured Region 3), RR Lyraes (the cyan-coloured Region 4), stellar locus stars (the blue-coloured Region 5) and high-redshift quasars (the purple-coloured Region 6). The colour-space divisions provide only very rough classifications. In some cases (such as region 1), the label does not even describe the typical population, and we merely use the labels as a point of comparison to their work.

The percentages of the variable subsample and the whole sample lying in the regions of the colour-colour plots are given in Table 2.1, whilst sample lightcurves have already been shown in Figure 2.4. Almost all (>93 per cent) of the variable objects lie in three regions – namely, low-redshift quasars (53 per cent of the catalogue), stellar locus stars (31.4 per cent), and RR Lyrae stars (9.3 per cent). When split according to magnitude, the bright ($g < 19.0$) variable-sky is dominated by stellar

2 Variable stars in SDSS Stripe 82

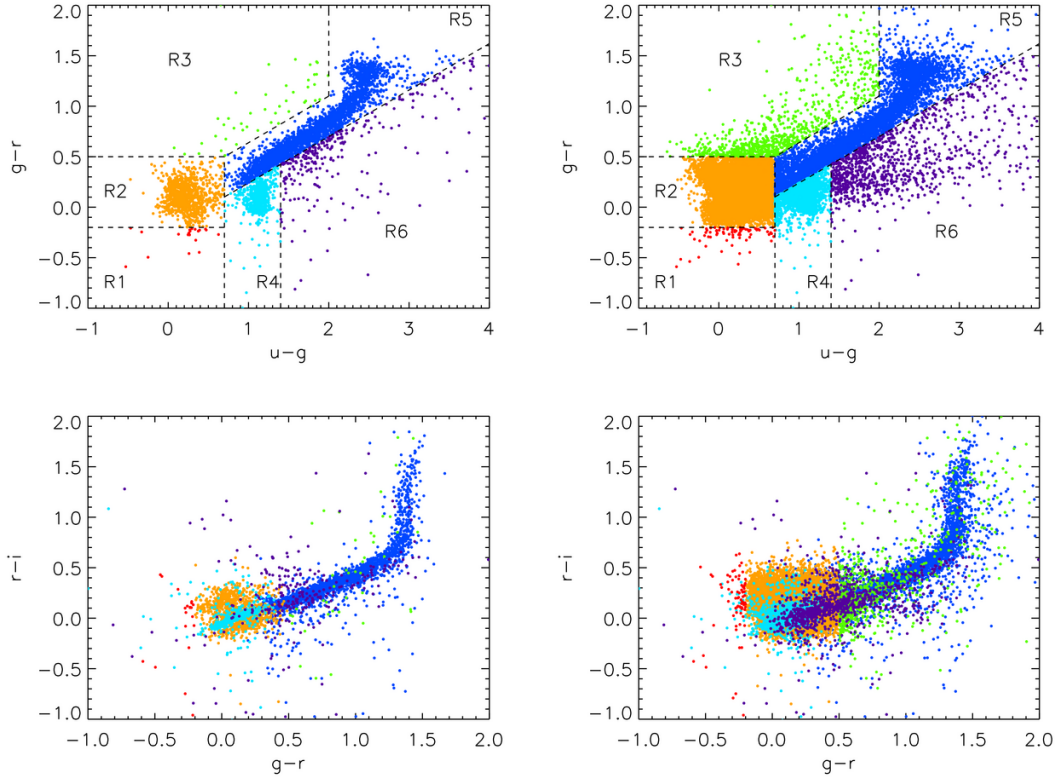


Figure 2.7: Colour-colour plots for 4 648 variables brighter than $g = 19.0$ (left) and 21 789 variables brighter than $g = 22.0$ (right). The upper panels are $g - r$ versus $u - g$, the lower panels are $r - i$ versus $g - r$. Sesar et al. (2007) label these regions as white dwarfs (Region 1, red), low-redshift quasars (Region 2, orange), M dwarf/white dwarf binaries (Region 3, green), RR Lyraes (Region 4, cyan), main stellar locus (Region 5, blue) and high-redshift quasars (Region 6, purple).

locus stars, but the faint ($g < 22.0$) variable-sky is dominated by quasars. We can compare our results to Table 1 of Sesar et al. (2007), which shows the same quantities for their variable subsample. Our variability criteria picks out more variable objects, and in particular more denizens of the main stellar locus.

The spatial distribution of variable objects in Stripe 82 is shown in Figure 2.8. The equatorial stripe reaches down to low Galactic latitudes beyond $\alpha \approx 18^{\text{h}}$ (see e.g. Figure 1 of Belokurov et al., 2007). Variables belonging to Region 4 (RR Lyraes) and Region 5 (the main stellar locus) dominate here, whereas variables belonging to the other Regions are more uniformly dispersed in right ascension.

2.4 Summary

In this chapter, I have described the construction of a catalogue of 21 939 variable objects in SDSS Stripe 82 using the catalogues of Bramich et al. (2008).

A handful of randomly-selected light-motion curves show obvious variation; the nature of the variation is varied, with both RR Lyraes and eclipses easily identified. It is clear, then, that the sample does indeed contain variable stars and the algorithm is sensitive to a variety of different types of

Table 2.1: The distribution of candidate variable sources in the $g - r$ versus $u - g$ diagram. The columns list the fraction of the whole sample and the variable subsample lying in the six regions of the colour-colour plot.

Region	Population	$g < 19$		$g < 20.5$		$g < 22$	
		% all	% var	% all	% var	% all	% var
1 (red)	white dwarfs	0.09	0.43	0.16	0.33	0.20	0.36
2 (orange)	low-redshift QSOs	0.29	21.32	1.20	52.96	5.31	61.05
3 (green)	dM/WD pairs	5.95	1.01	9.51	1.59	11.77	3.65
4 (cyan)	RR Lyrae stars	3.27	15.23	3.62	9.31	3.47	7.85
5 (blue)	stellar locus stars	75.93	56.41	74.62	31.44	69.65	22.48
6 (purple)	high-redshift QSOs	14.47	5.59	10.89	4.37	9.61	4.62
	total count	283,899	4,648	447,800	12,788	518,058	21,789

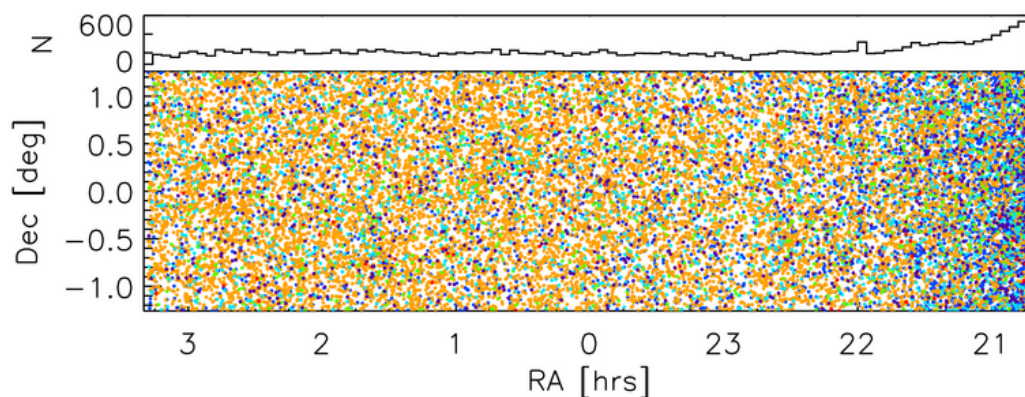


Figure 2.8: The spatial distribution of the variable subsample in Stripe 82. Objects are colour-coded according to the Regions of the colour-colour plot in which they lie (see Figure 2.7). The upper panel shows the number of all the variable objects versus right ascension.

variable object.

Following the work of Sesar et al. (2007), we applied crude colour-colour cuts to our variable selection to distinguish between different types of variable object, finding stellar locus stars to be the dominant population at bright ($g < 19$) magnitudes and low-redshift quasars dominant at faint ($g < 22$) magnitudes. Colour-magnitude diagrams suggest that variable quasars are the most common type of variable object found in the variable catalogue. We also found the RR Lyraes to be significant population across the Stripe.

Of course, the cuts we have applied here are only rough, they enable us to get a feel for what the types of variables the catalogue contains and which populations are most dominant. As we will see in Chapter 3, where I extract a sample of RR Lyraes from the variable catalogue, if we want to obtain a clean sample of a particular type of variable, the colour cuts have to be refined and augmented with extra information.

3

Substructure revealed by RR Lyraes in SDSS Stripe 82

Variable stars of particular interest are RR Lyraes, which have often been used to identify Galactic substructure – for example, in studies of the Sagittarius Stream (Ivezic et al., 2000; Vivas et al., 2004; Keller et al., 2008), and the Monoceros and Virgo Overdensities (Vivas & Zinn, 2006; Keller et al., 2009). RR Lyraes are particularly useful for three reasons. First, they are constituents of the old, metal-poor halo, in which substructure is abundant. Second, they are standard candles, enabling an estimate of their distances to be made. Third, they are bright enough to be detected out to distances of ~ 130 kpc in the SDSS data, giving us an insight into the structure of the remote MW halo.

In Chapter 2, I described the selection of a set of variables in SDSS Stripe 82. In this chapter, I will describe the identification of RR Lyrae stars within that variable sample and what we are able to learn from their properties about the Galactic halo. I begin in Section 3.1 by giving an overview of RR Lyrae stars and the properties that make them so useful for finding and analysing substructure in the Galaxy. Section 3.2 describes the classification of the RR Lyrae stars and properties of the population in some detail, then Section 3.3 discusses substructure seen in the distribution of the RR Lyraes. Finally, I summarise my results in Section 3.4.

3.1 Overview of RR Lyraes

RR Lyraes are regular variables with short periods, usually found in the range 0.2-1.2 days, and moderate amplitudes, around 0.2-2 mag in V. They are also moderately bright and so can be seen out to the edge of our galaxy and in some of our closest neighbours. The regular variation makes them excellent local standard candles: we can determine accurately their absolute magnitudes and hence we can calculate accurate distances to these stars; combined with their position on the sky we can accurately pinpoint their three-dimensional position in space. They also have very distinctive lightcurves, which greatly aids in their classification.

RR Lyraes are low mass A-F horizontal branch stars in the core helium-burning phase of their evolution; low mass stars are very common and are found throughout the galaxy, so we see RR Lyraes

3 Substructure revealed by RR Lyraes in SDSS Stripe 82

throughout the galaxy. This makes them excellent tracers of substructure; for if there is an overdensity of stars in a particular region, there will be an overdensity of low mass stars and hence also of RR Lyraes. Further, they can be used to trace the chemical and dynamical properties of their surroundings.

This class of variables received their name when a 7th magnitude variable in Lyra was found to have a period of 0.56 days (Pickering, 1901); it was given the name RR Lyrae and subsequent variables with similar properties were named for it. RR Lyrae remains the brightest star of the class.

RR Lyrae lightcurves are many and varied. Bailey (1902) divided RR Lyraes into three classes - a, b and c - based on the appearance of their lightcurves. Continued study of Lyraes has altered the classification instead to just ab and c. RR Lyrae variability is a result of radial pulsations of the star and it is believed that RRab stars pulsate in the fundamental mode and RRc stars pulsate in their first overtone; it is clear now why the original a and b classes were redefined into one single subset.

The two classes have different properties: RRab stars generally have relatively large visual magnitudes (of order one magnitude) and they have asymmetric light curves with a steep rising branch and a slow, steady decline. Their periods lie mostly in the range 0.4-1.0 days and studies of RR Lyraes in GCs have shown that the amplitude of RRab stars decreases with increasing period. RRc stars, on the other hand, have smaller visual amplitudes (around half a magnitude) and their lightcurves are nearly sinusoidal, so are much more symmetric. They generally have periods of 0.2 - 0.5 days.

Some RR Lyraes pulsate in both the fundamental mode and their first overtone (with a period ratio of about 0.746); they are called double mode RR Lyraes and are given the designation RRd (in recent literature) or RRb (as they are defined in the General Catalogue of Variable Stars (GCVS, Kholopov et al., 1996)); this simultaneous excitation of two pulsation modes leads to changes in the shape and amplitude of the lightcurves from one cycle to the next. RR Lyraes have also been found that are pulsating in the second overtone as well as the first overtone and the fundamental, but no stars have yet been found that pulsate purely in the second overtone.

Further, many RR Lyraes show long-term modulation in their lightcurves as well; this is known as the Blazhko effect and its origins are not well understood. The Blazhko period is generally in the range 20-200 days and this effect also shows even longer term modulation in some stars with a modulation period of between 4 and 5 years.

The physics and proposed pulsation mechanisms of RR Lyraes is discussed at length in Smith (1995). I do not intend to go into any depth about the origin and nature of the RR Lyrae pulsations and physical processes at work in these stars, but it is worth noting that their lightcurves can be quite complex and there can be a number of different variation frequencies at work.

RR Lyraes make up more than 90% of cluster variables, but they are also well represented among field stars and are found in the thin disk, thick disk and halo. The GCVS classifies more than one fifth of the variables as RR Lyraes, so we know that they are reasonably common. 91% of known RR Lyraes are type RRab and only 9% are type RRc, however this ratio is undoubtedly biased as the RRc variables have smaller amplitudes and so will be harder to detect.

RR Lyraes are old; there is some evidence that they have only been found in GCs with estimates ages older than 12 Gyr, giving us an approximate lower age limit. RR Lyraes are also low mass stars and so they have not burnt significant amounts of heavy elements in their cores; as a result, they contain the same heavy element abundance as the interstellar gas cloud from which they formed. Combined,

these two properties make them excellent tracers of the chemical history of the galaxy.

Another well-known class of variable star used as standard candles are the Cepheids. Like RR Lyraes, Cepheids are also radially pulsating stars. RR Lyraes are not as bright as Cepheids but they do have the advantage of being more populous. Additionally, RR Lyraes are population II stars whereas Cepheids are population I stars, so we can see RR Lyraes in old systems where there are no young (Population I) stars to be found.

Distances to RR Lyraes can be determined using their absolute magnitudes via the distance modulus, however their absolute magnitude is not known exactly which does introduce some uncertainty into the distance estimates. Ideally, the absolute magnitude should be known to within 0.1 mag for accurate distance determination, but that accuracy has not yet been achieved and there is ongoing study to constrain the absolute magnitude further. The absolute magnitude has been shown to correlate linearly with metallicity, but the parameters of this correlation quoted in the literature vary. Further, the absolute magnitude is somewhat dependent on the evolutionary state of the RR Lyrae - all RR Lyraes lie on the zero-age horizontal branch (ZAHB) but they have different positions along this strip according to their state of evolution. The position of the star on the ZAHB will effect the mean apparent magnitude estimate and hence introduce uncertainties into the absolute magnitude. Regardless of all of these considerations, the absolute magnitude range of RR Lyraes is quite restricted, which is one of the reasons why RR Lyraes are good standard candles.

3.2 Selection of the RR Lyrae sample

3.2.1 Identification of RR Lyraes

Here, we develop the tools to extract a high quality sample of RR Lyraes from the variable catalogue. We begin by selecting the 873 candidates that simultaneously satisfy all the following criteria, which are adapted from Ivezić et al. (2005), namely

$$\begin{aligned}
 13.5 < r < 20.7, & & 0.98 < u - g < 1.35, \\
 -0.16 < r - i < 0.22, & & -0.21 < i - z < 0.25, \\
 D_{ug}^{min} < D_{ug} < 0.35, & & D_{gr}^{min} < D_{gr} < 0.55,
 \end{aligned} \tag{3.1}$$

where

$$D_{ug} = (u - g) + 0.67(g - r) - 1.07, \quad D_{gr} = 0.45(u - g) - (g - r) - 0.12. \tag{3.2}$$

The r band magnitudes correspond to distances ~ 5 -130 kpc. D_{ug} and D_{gr} represent slopes in the $u - g$ and $g - r$ colour-colour plane. Combined with the cut on $u - g$, the D_{ug} and D_{gr} criteria constrain the RR Lyraes to a hexagonal box in colour-colour space, optimizing the selection of RR Lyraes. The values D_{ug}^{min} and D_{gr}^{min} can be altered to adjust the completeness and efficiency of the RR Lyrae selection. We chose to use values $D_{ug}^{min} = -0.05$ and $D_{gr}^{min} = 0.06$, which would give a completeness of 100 per cent for the QUEST survey RR Lyraes (Vivas et al., 2004; Ivezić et al., 2005).

3 Substructure revealed by RR Lyraes in SDSS Stripe 82

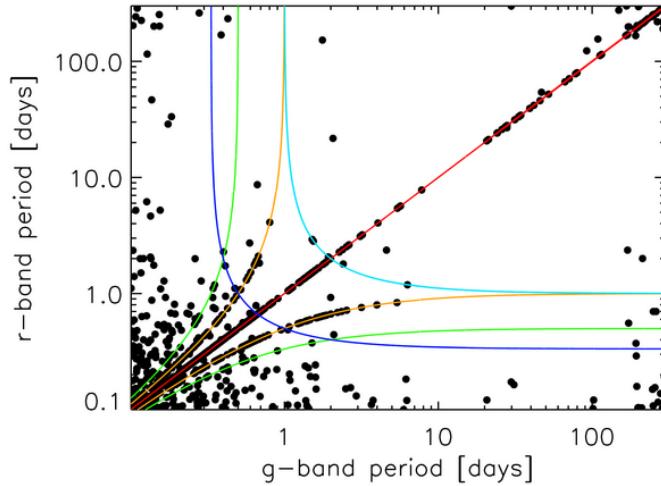


Figure 3.1: Lomb-Scargle period estimates in the g and r bands for the candidate RR Lyraes. The coloured lines represent resonance lines along which one period is a harmonic of the other: $P_r = P_g$ (red), $P_r = P_g / (1 \pm P_g)$ (orange), $P_r = (P_g / 1 \pm 2P_g)$ (green), $P_r = P_g / (P_g - 1)$ (cyan), $P_r = P_g / (2P_g - 1)$ (blue).

3.2.2 RR Lyrae Periods

Determining periods for our RR Lyrae candidates is non-trivial. In general, there are 30 to 40 datapoints in a lightcurve, unevenly sampled over an eight-year baseline. From this sparsely-sampled data, we seek a period that is a fraction of a day. The multi-band nature of the SDSS survey is an advantage here, as we are able to verify that any period estimate we obtain in one band is consistent with the data in additional bands.

The LMCC contains all the data for a given lightcurve. Each datapoint has a flag that is set (or unset) if the datapoint passes (or fails) certain quality requirements (for more details, see Bramich et al., 2008). For period estimation, it is important that we use only the reliable data to minimise errors. In general, the g and r bands have smaller errors and fewer outliers and their clean lightcurves are the best sampled, so these bands are used together to estimate periods for our lightcurves.

As a first pass, we run a Lomb-Scargle periodogram (see e.g., Press, Flannery, Teukolsky & Vetterling, Press et al.) on each of the g and r band lightcurves, taking care to ensure that the frequency range extends to the high frequencies (or low periods) expected for RR Lyrae stars and that the sampling rate is detailed enough to discern individual peaks. The resulting period estimates are plotted in Figure 3.1. First, we note that there are a number of candidates which have matching period estimates. A number of resonance lines – the locations at which one of the period estimates is a harmonic of the other – are plotted as solid lines in the graph.

The resonance lines are well-populated, indicating that the Lomb-Scargle periodogram can return harmonics of the true period as well as the period itself. Hence, we must consider whether the exact period matches are indeed cases where the true period has been recovered, or whether both period estimates are harmonics, and so on. Lightcurves with periods that do not match or do not lie on resonance lines could be objects that are not periodically variable – quasars, for example –

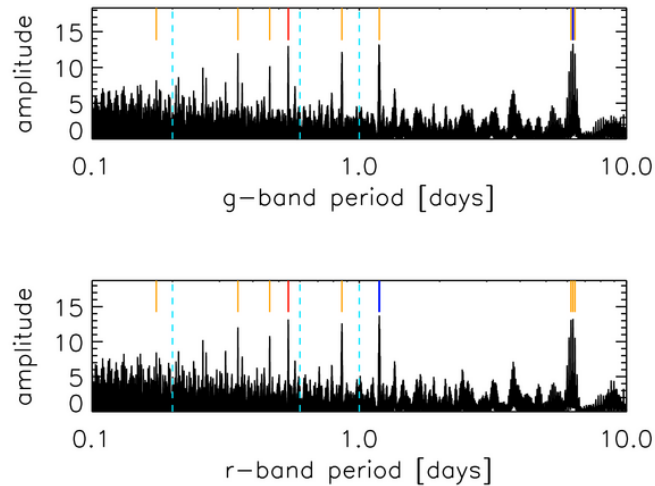


Figure 3.2: A sample periodogram spectrum. The highest peak in each spectrum is indicated by the blue line; the additional peaks selected by the method described in the text are indicated by the orange lines, with the eventual best-fit peak marked with a red line. At least one peak was found in each region delineated by the cyan lines.

or objects for which the periodogram has failed to recover the true period or a harmonic of the period in one or both cases. Not all of the period estimates lie within the range expected for RR Lyraes (0.2 – 0.8 days), which is probably a consequence of contamination in our sample. However, it is unclear whether we can simply reject any objects with period estimates larger than those expected for RR Lyraes. Certainly, some of the larger period estimates could be attributed to the sparse sampling of the lightcurves, which may generate a signal that overwhelms the periodic nature of the RR Lyraes.

Accordingly, we experimented with a number of alternative methods, including binning, smoothing and phase dispersion minimization, before concluding that a string-length technique is the most effective for our dataset. In outline, a string-length method works by phasing a lightcurve with a trial period and calculating the sum of the straight-line distances between consecutive points. The sum of these distances, or the string-length, will be minimised if the trial period is the true period.

We use a variation of the Lafler & Kinman (1965) string-length technique described in Stetson (1996). For each trial period, the string-length is computed for the g and r bands. Their sum is taken as the overall string-length, which is minimised to obtain a period estimate. Running a string-length period finder over a wide and finely-sampled range of trial periods is computationally expensive. However, we can short-cut the process by restricting the string-length period search to a narrow range of periods, centred on a set of the most likely periods identified via the Lomb-Scargle periodogram.

To ensure that the correct RR Lyrae periods are identified, the g and r band Lomb-Scargle periodogram spectra were combined and the highest peaks in each of the ranges $P < 0.2$, $0.2 < P < 0.6$, $0.6 < P < 1.0$ and $P > 1.0$ days were selected. Then, four further peaks were selected from each of the g and r band spectra independently. This was done according to highest amplitude, until four distinct new peaks had been selected in each band. A sample periodogram with the selected peaks highlighted is shown in Figure 3.2 Each peak was then considered in turn: the string-length was calculated for a narrow range of periods spanning the peak, the period for which the string-length was

3 Substructure revealed by RR Lyraes in SDSS Stripe 82

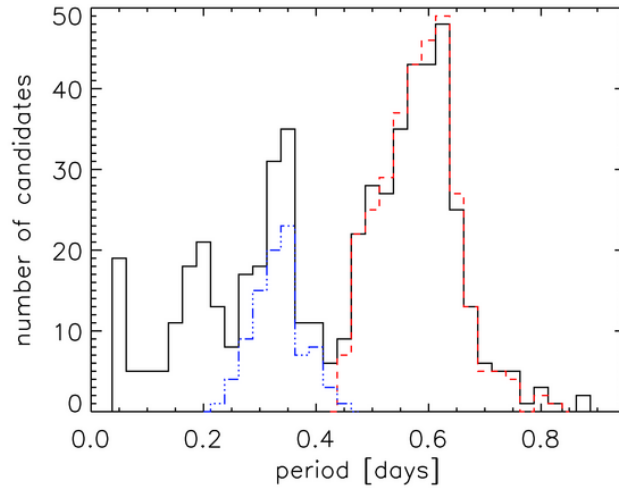


Figure 3.3: The distribution of periods for all RR Lyrae candidates with periods in the expected range for RR Lyraes (black, solid), for the ab-type RR Lyraes (red, dashed) and the c-type RR Lyraes (blue, dot-dashed). The spike at $P < 0.1$ is due in part to δ Scuti and SX Phe stars, and the population with the shortest periods is due mostly to eclipsing variables.

minimised was taken to be the best period in the vicinity of that peak. Finally, the period that returned the shortest string-length overall was adopted as the period estimate for the lightcurve.

In Figure 3.3, the solid black line is the period distribution for all of the RR Lyrae candidates and shows four clear peaks. Moving from high to low periods, these populations are predominantly: ab-type RR Lyraes (peak at ~ 0.6 d), c-type RR Lyraes (peak at ~ 0.35 d), eclipses (peak at ~ 0.18 d) and δ Scuti and SX Phe stars (peak at ~ 0.05 d). Also present in this candidate sample, are a number of non-periodic variables. The red dashed line is the period distribution for only those stars later determined to be ab-type RR Lyraes and the blue dot-dashed line is for those stars we later determine to be c-type RR Lyraes.

Before proceeding any further, we clean the sample of some eclipsing variable stars, δ Scuti stars, SX Phe stars and non-periodic variable contaminants by adopting a stringent cut on Stetson index $L_g > 2.5$. To perform subsequent analysis, we require that objects have a sufficient number of clean data points; that is, we impose further cuts on the number of clean epochs in the g and r bands: $N_g > 5$ and $N_r > 5$, leaving 604 candidates.

Uncertainties in the period estimates may be attributed to two sources. If we assume that the estimate is indeed close to the true period and not a harmonic, then any error is due to the string-length fitting technique, estimated to be $\sim 10^{-5}$ day, from analysis of the phased RR Lyrae lightcurves. However, for a small fraction of the sample, where the period estimate is a harmonic of the true period, the error will be ~ 0.1 - 0.5 day.

3.2.3 RR Lyrae Classification

Bailey (1902) first divided RR Lyraes into three classes - a, b and c - based on the appearance of their lightcurves. Further study of Lyraes has altered the classification instead to just ab and c. It is be-

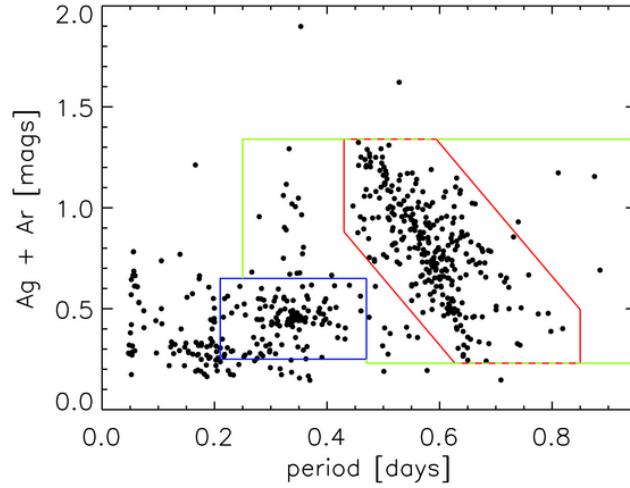


Figure 3.4: Period versus the combined g and r band amplitudes. Three selection boxes are shown: red for candidate RRabs, blue for candidate RRcs, and green for candidates warranting further study.

lieved that RRab stars are pulsating in the fundamental mode and RRc stars are pulsating in their first overtone (e.g., Smith, 1995).

The two classes have somewhat different properties: RRab stars generally have relatively large amplitudes (of order a magnitude) and asymmetric lightcurves with a steep rising branch and a slow, steady decline. Their periods lie mostly in the range 0.4-1.0 day and studies of RR Lyraes in GCs have shown that the amplitude of RRab stars decreases with increasing period. RRc stars have smaller visual amplitudes (around half a magnitude) and their lightcurves are more symmetrical and nearly sinusoidal. They generally have periods of 0.24-0.5 day.

To separate the two classes, we proceed by plotting the candidates in the plane of (P, A) , where P is the period and A is the sum of the amplitudes in the g and r band lightcurves, as shown in Figure 3.4. The red box is defined as the region

$$\begin{aligned} 0.43 < P < 0.85, \quad 0.23 < A < 1.34 \\ 2.3 < A + 3.3P < 3.3 \end{aligned} \quad (3.3)$$

and includes 296 RRab candidates. The blue box is defined as the region

$$0.21 < P < 0.47, \quad 0.25 < A < 0.65 \quad (3.4)$$

and includes 122 RRc candidates. Finally, the green boxes (not fully shown in Figure 3.4 for clarity, but which extend to a period of two days) include a number of further candidates, which we do not want to discard without further investigation. Objects with a period of one day are almost certainly spurious (the lightcurves have a sampling period of one day) and are removed.

For the 43 objects that remain, there is the possibility that they may lie away from the concentration of RR Lyraes because of an incorrect period estimate. As discussed in Section 3.2.2, errors in

3 Substructure revealed by RR Lyraes in SDSS Stripe 82

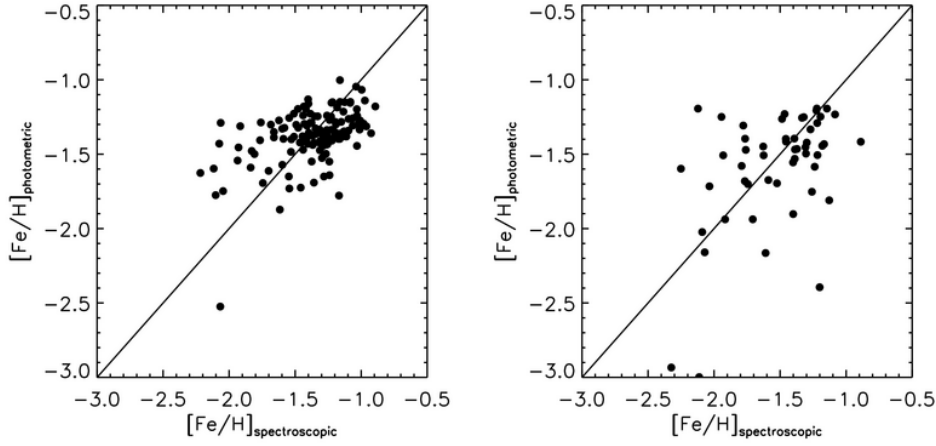


Figure 3.5: The performance of the photometric metallicity relationships in equations (3.7) and (3.9) is shown. The left (right) panel plots the RRAb (RRC) candidates with spectroscopic metallicities against the corresponding photometric estimate.

the period estimates are small, but sometimes a harmonic of the true period is obtained. Hence, we revisit the period analysis to determine whether any of the likely period peaks lie within the red RRAb box or the blue RRC box. If more than one period peak lies within a box, the period with the minimum string-length is used. Any objects for which a fitting period can be found are added to the RRAb or the RRC candidate set as appropriate. This reclassification results in 330 RRAb and 137 RRC candidates.

3.2.4 The RRAb types

126 of our RRAb and 52 RRC candidates possess SDSS spectra and have spectroscopic metallicity estimates. We use these objects to calibrate empirical relationships and thence derive photometric metallicities for the entire sample.

Jurcsik & Kovacs (1996) found that the metallicity of an RR Lyrae depends on the period P and the shape of the lightcurve, which may be parameterised via a Fourier decomposition:

$$f(\theta) = A_0 + \sum_{i=1}^N A_i \sin(i\theta + \phi_i). \quad (3.5)$$

The amplitudes A_i and the phases ϕ_i can then be combined as follows:

$$A_{ij} = \frac{A_i}{A_j}, \quad \phi_{ij} = j\phi_i - i\phi_j. \quad (3.6)$$

Inspired by the analogous relation of Jurcsik & Kovacs (1996), we use the spectroscopic metallicities and the lightcurve properties to derive the metallicity-period-amplitude-phase relation

$$\begin{aligned} [\text{Fe}/\text{H}] = & 0.845 - 4.487P - 0.187\phi_{31} - 1.454A_{31} + 2.166P\phi_{31} \\ & + 1.563PA_{31} - 8.374P^2 - 0.081\phi_{31}^2. \end{aligned} \quad (3.7)$$

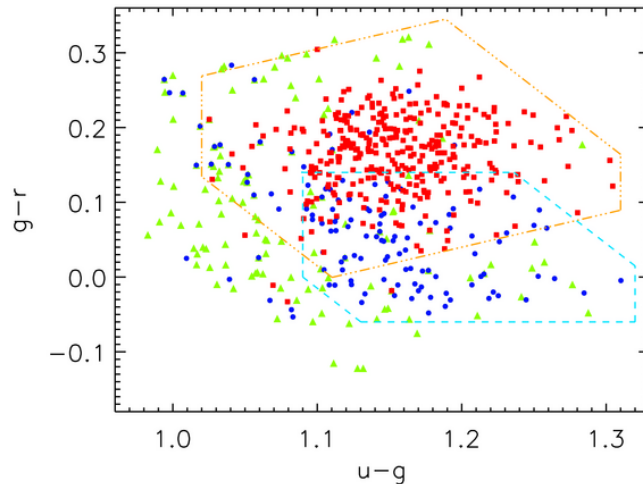


Figure 3.6: The RR Lyrae candidate selection boxes in the $u-g$ versus $g-r$ plane; the orange (dot-dashed) box is used to select RRab types, the cyan (dashed) box for RRC types. The RRab (RRC) candidates that pass the period, amplitude and metallicity cuts are shown as red squares (blue circles). Also shown are suspected eclipsing variables as green triangles.

which has a typical scatter $\sigma = 0.254$. Its performance is shown in the left panel of Figure 3.5. To refine our RRab sample, we insist that

$$-3 < [\text{Fe}/\text{H}] < 0, \quad (3.8)$$

and apply a further restriction to trim the sample of a remaining few eclipsing variables by imposing the selection box in orange (dot-dashed lines) in colour-colour space shown in Figure 3.6. This leaves us with 325 RRab candidates. Also shown in this figure are the confirmed RRab types as red squares and likely eclipsing variables as green triangles.

3.2.5 The RRC types

Morgan et al. (2007) found that the metallicities of c-type RR Lyraes also vary with period and lightcurve shape. Owing to the difference in pulsation mode, and hence lightcurve shape, between the RRab stars and the RRC stars, a new metallicity relation must be derived for the RRC candidates. The lightcurves were Fourier decomposed and the 52 RRCs with spectroscopic metallicities were used to derive the following metallicity-period-amplitude relation, the form of which is suggested by Morgan et al. (2007):

$$[\text{Fe}/\text{H}] = -10.669 + 60.944P + 4.351A_{21} - 23.418PA_{21} - 95.344P^2 + 1.864A_{21}^2. \quad (3.9)$$

As the right panel of Figure 3.5 shows, there is somewhat greater scatter in this relationship than the corresponding one for RRabs. The scatter in this relation was found to be $\sigma = 0.378$.

A metallicity cut $-3.75 < [\text{Fe}/\text{H}] < 0$ removes a few obvious outliers. As for the RRabs, we discard eclipsing variables by imposing the selection box in cyan (dashed lines) in colour-colour space shown

3 Substructure revealed by RR Lyraes in SDSS Stripe 82

in the lower panel of Figure 3.6. This leaves us with 97 RRc type candidates. Also shown in this figure are the confirmed RRc types as blue dots and likely eclipsing variables as green triangles.

In the same way that the outlying candidates were reanalysed to determine whether a period could be found that placed the star into the RRab or RRc dataclouds, so the RRab and RRc rejects are also reanalysed, just in case they are misclassified RRc and RRab respectively. The metallicity and colour cuts described above then determine inclusion in the candidate sets. Finally, a visual inspection of the lightcurves confirms that these are very high-quality samples. Judging by lightcurve shape, there are at most 21 possible contaminants in the RRab set and only 6 possible contaminants in the RRc set. The lightcurves typically possess low S/N and/or are poorly sampled. While many of these objects will be RR Lyrae, to be conservative, they are removed, giving us a final sample of 316 RRab stars and 91 RRc stars, 407 RR Lyraes in all.

3.3 Substructure revealed by the RR Lyraes

3.3.1 RR Lyrae Distances

RR Lyraes are “standard candles” because they have a well-defined absolute magnitude, which, nonetheless, depends on metallicity. We calculate distances via the distance modulus:

$$\log D = \frac{m_z - M_z + 5}{5} \quad (3.10)$$

The apparent magnitudes m_z come directly from the HLC. The absolute magnitudes M_z are obtained via the following relation from Cáceres & Catelan (2008):

$$\begin{aligned} M_z = & 1.3706 + 0.8941 \log Z + 0.1315 [\log Z]^2 \\ & - (2.6907 + 0.8192 \log Z + 0.0664 [\log Z]^2) \ln C_0 \\ & + (47.9836 + 31.7879 \log Z + 5.2221 [\log Z]^2) [\ln C_0]^2 \\ & + (141.7704 + 100.6676 \log Z + 17.4277 [\log Z]^2) [\ln C_0]^3 \\ & + (0.3286 + 2.0377 \log Z + 0.3882 [\log Z]^2) \log P \end{aligned} \quad (3.11)$$

where P is the fundamental period, $\log Z = [\text{Fe}/\text{H}] - 1.5515$ and $C_0 = (u - g)_0 - (g - r)_0$, with the 0 subscript denoting that the colours are unreddened. The intrinsic scatter in this relation is small compared to the errors. Uncertainties on the metallicities $[\text{Fe}/\text{H}]$ and distances D are computed using standard methods. From this analysis, we find that the distance errors are typically less than 5 per cent; in practice, the distance errors will be larger due to the scatter in the relations used to derive metallicities.

The right ascension, declination, classification, mean magnitudes, amplitude, period and distance of all our 407 RR Lyrae candidates are given in an accompanying electronic table. The means and dispersions for some useful quantities for the RRab and RRc subsamples are given in Table 3.1.

Table 3.1: The means and dispersions in the properties of the RR Lyrae variables split according to RRab and RRC types. Listed are the amplitudes in the g and r bands, the period, the reduced χ^2 in g and r , the Stetson index, the metallicity, the heliocentric distance D and Galactocentric distance r , the absolute magnitude M_z and the number of good epochs in g and r .

property	μ_{ab}	σ_{ab}	μ_c	σ_c
A_g (mag)	0.47	0.14	0.26	0.05
A_r (mag)	0.34	0.11	0.19	0.03
P (days)	0.58	0.07	0.33	0.04
χ_g^2	363.8	326.1	146.6	80.0
χ_r^2	250.9	232.3	98.5	53.8
L_g	10.7	5.2	8.4	2.5
[Fe/H]	-1.38	0.16	-1.61	0.42
D (kpc)	28.9	21.9	21.1	17.6
r (kpc)	29.2	21.7	21.5	17.5
M_z	0.44	0.11	0.71	0.15
N_g	29.6	7.4	29.4	8.4
N_r	29.6	7.7	29.6	8.0

3.3.2 The Sagittarius Stream, the Hercules-Aquila Cloud and the Pisces Overdensity

The distribution of RR Lyraes in right ascension and distance is shown in Figure 3.7, with the ab-types plotted as red circles and the c-types plotted as blue triangles. There are a number of things to notice. First, there are 296 RR Lyraes at right ascensions $20.7^{\text{h}} < \alpha < 24^{\text{h}}$, but only 111 at $0^{\text{h}} < \alpha < 3.3^{\text{h}}$. The greatest concentration of RR Lyraes is in the fields coincident with the Hercules-Aquila Cloud (Belokurov et al., 2007). Of course, not all these RR Lyraes are necessarily associated with the Cloud, as there may be contamination from the underlying smooth population associated with the Galactic Spheroid. It is known that the Bulge and Spheroid harbour a population of RR Lyraes, distributed in a roughly spherical manner around the Galactic Centre, with a metallicity distribution peaked at $[\text{Fe}/\text{H}] \sim -1$ (see e.g. Walker & Terndrup, 1991; Alcock et al., 1998; Collinge et al., 2006). The plane of the orbit of the Sagittarius dwarf galaxy crosses Stripe 82, and there is a visible overdensity of RR Lyraes at this location ($\alpha \approx 2^{\text{h}}$). Finally, we note that there are few (specifically 47) RR Lyrae at large distances ($D > 50$ kpc), of which 28 lie in a clump at $\alpha \approx 23.5^{\text{h}}$. We term the structure the *Pisces Overdensity*. Distance uncertainties are shown as vertical bars for each RR Lyrae – although the error bars for the distant RR Lyrae are large enough to be visible, they cannot be responsible for the overdensity.

The upper panel of Figure 3.8 shows the fraction of accessible volume as a function of Galactocentric radius r probed by our survey. The volumes are calculated via Monte Carlo integrations in which the RR Lyrae luminosity function is modelled as a Gaussian with mean and dispersion from Table 3.1; the magnitude limits used were those defining our RR Lyrae sample. The survey reaches at least $r \sim 100$ kpc before the accessible volume begins to decline. The brightest RR Lyraes in our sample have $M_z = 0.1$ and so are still detectable within $r \sim 130$ kpc. In classical models of the smooth halo, the RR Lyraes are distributed as a power-law like $\rho \sim r^{-n}$ with $n \sim 3.1$ (Wetterer & McGraw, 1996). With no substructure present in Stripe 82, the right ascension-distance graph of Figure 3.7 would look rather

3 Substructure revealed by RR Lyraes in SDSS Stripe 82

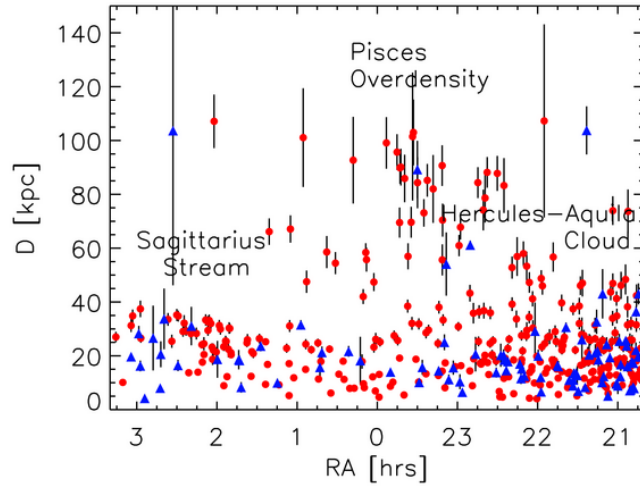


Figure 3.7: The spatial distribution of the ab-type (red circles) and the c-type (blue triangles) RR Lyraes.

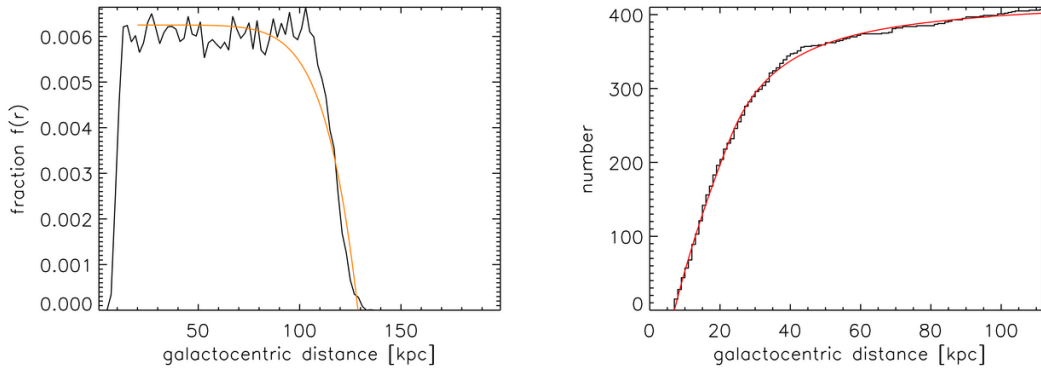


Figure 3.8: Top: The fraction of Galactic volume probed by the RR Lyrae in Stripe 82 as function of Galactocentric distance r . Bottom: The cumulative number of RR Lyrae within radius r in Stripe 82, together with the fits given in equation (3.12).

different. The fall-off in numbers would be steady, and not as sharp as the drop observed beyond $D \sim 40$ kpc, which is real and cannot be attributed to properties of the survey.

The presence of an edge to the RR Lyrae distribution in the stellar halo at $r \sim 50$ kpc has been proposed before by Ivezić et al. (2000), using a sample of 148 RR Lyrae in SDSS commissioning data. However, the same authors later applied their method to a larger area of the sky and found no break until at least 70 kpc (Ivezić et al., pp 179–+). Vivas & Zinn (2006) also found no break before the limit of their survey at ~ 60 kpc. So, “edge” may be too strong a term, but the number density profile of the RR Lyrae does seem to be best matched by a broken power-law, as shown in the lower panel of Figure 3.8. Such a parameterisation was first advocated by Saha (1985), who noticed that the RR Lyrae density fell off much more rapidly beyond Galactocentric radii of 25 kpc. Adjusting by the fraction of Galactic volume sampled by our survey, and assuming that our efficiency is $\epsilon \approx 1$, we find that the spherically-averaged number density of RR Lyrae as

3.3 Substructure revealed by the RR Lyraes

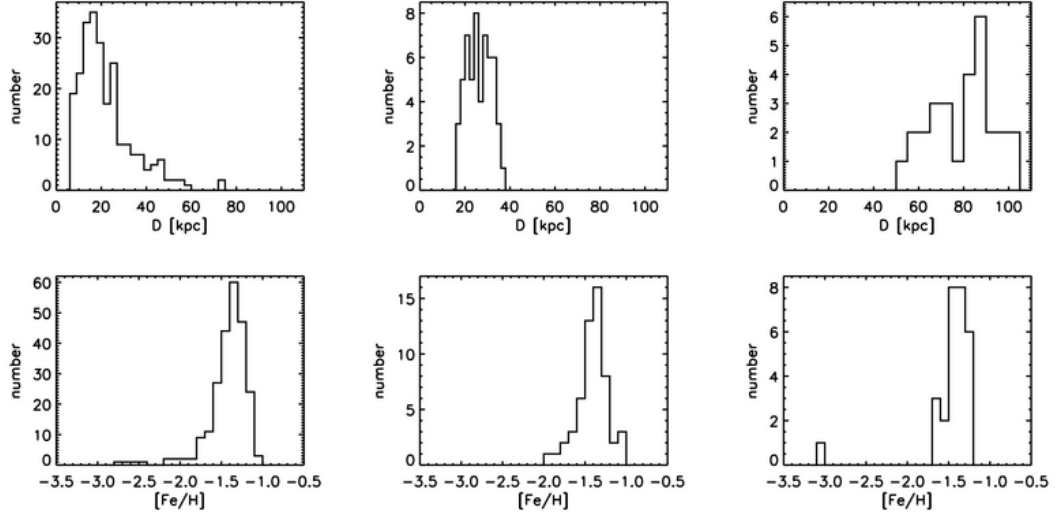


Figure 3.9: The distributions of distances (top) and metallicities (bottom) of RR Lyraes in the Hercules-Aquila Cloud (left), Sagittarius Stream (centre) and the Pisces Overdensity (right).

$$n(r) = 2.6 \times \begin{cases} \left(\frac{23\text{kpc}}{r}\right)^{2.4} & \text{if } 5 < r \leq 23 \text{ kpc} \\ \left(\frac{23\text{kpc}}{r}\right)^{4.5} & \text{if } 23 < r < 100 \text{ kpc} \end{cases} \quad (3.12)$$

out to ~ 100 kpc, beyond which our data is highly incomplete, with only bright RR Lyraes detectable (see Figure 3.9). Our break radius of 23 kpc is very close to that proposed by Saha (1985).

The inner power-law slope is almost the same as that found by Miceli et al. (2008) – namely $n = -2.43$ – in a very large sample of RR Lyrae stars closer than 30 kpc in the LONEOS survey. Of course, formulae such as equation (3.12) are just a parameterisation of the data, as the RR Lyrae distribution is neither spherically symmetric nor smooth, but dominated by the three structures in the Stripe. The break at $r \sim 25$ kpc is really a consequence of the fact that most of the RR Lyraes are in the Hercules-Aquila Cloud and the Sagittarius Stream substructures, which lie within 40 kpc of the Galactic centre. A similar conclusion regarding the importance of substructure is reached by Sesar et al. (2007), who divide their RR Lyrae distribution into 13 clumps, of which they suggest at least seven correspond to real substructures.

In Figure 3.10, the number density of RR Lyraes is plotted in the plane of Galactic longitude versus r band magnitude. The three substructures show up very clearly, together with some isolated hot pixels that may be indicators of real objects. We define the Sagittarius Stream RR Lyraes via

$$180^\circ > \ell > 135^\circ, \quad 16.5 < r < 18.5 \quad (3.13)$$

RR Lyraes associated with the Hercules-Aquila Cloud are extracted via

$$80^\circ > \ell > 45^\circ, \quad 14.5 < r < 20, \quad \ell + 15r < 358 \quad (3.14)$$

For the Pisces Overdensity, we chose the stars satisfying

3 Substructure revealed by RR Lyraes in SDSS Stripe 82

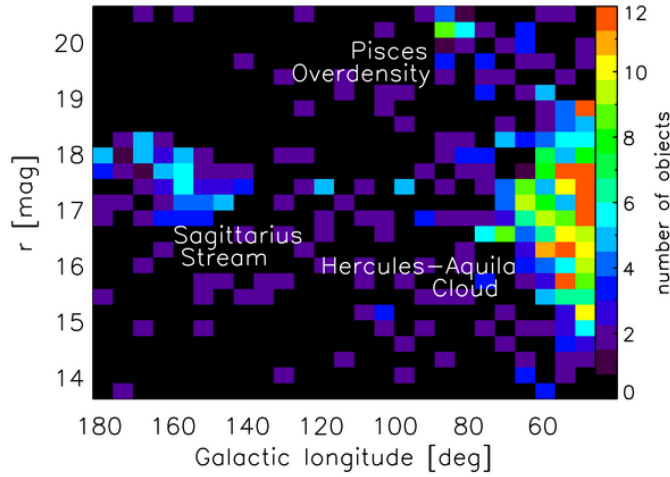


Figure 3.10: The number density of RR Lyraes in the plane of Galactic longitude versus r magnitude. There are three obvious overdensities corresponding to the Sagittarius Stream, the Hercules-Aquila Cloud and the Pisces Overdensity.

$$95^\circ > \ell > 60^\circ, \quad r > 19, \quad \ell + 15r > 358. \quad (3.15)$$

These cuts give 55 stars in the Sagittarius Stream, 28 in the Pisces Overdensity, and 237 in the Hercules-Aquila Cloud.

Ideally, we would like to separate any contaminating Bulge and Spheroid RR Lyrae from those of the Hercules-Aquila Cloud, but this is not easy. In particular, Figure 3.11 shows the density distribution of the RR Lyrae populations colour-coded according to metallicity. The comparatively metal-rich RR Lyraes (red in the Figure) do not seem to be distributed any differently from the comparatively metal-poor (green and blue). In fact, all the distributions are distended and distributed asymmetrically relative to the Galactic Centre, consistent with the bulk of the stars belonging to the Hercules-Aquila Cloud.

The properties of the RR Lyrae in the different substructures are listed in Table 3.2. Note that very nearly 60 per cent of all the RR Lyraes in Stripe 82 are associated with the Hercules-Aquila Cloud, emphasising the arguments made by Belokurov et al. (2007) as to the importance of this structure. The mean heliocentric distances of the Hercules-Aquila Cloud and the Sagittarius Stream are comparable in Stripe 82, but the Pisces Overdensity is much further away at $D \sim 80$ kpc. The Pisces Overdensity lies within a few degrees of the Magellanic Plane. Although the distance of the Overdensity is greater than that of the Large and Small Magellanic Clouds ($D \sim 55$ kpc), it is possible that the Magellanic Stream may be more distant in this area of the sky. Thus, at present, it is unclear whether the Pisces Overdensity is related to Magellanic Cloud debris.

One way to estimate the mass of the Pisces Overdensity is to compare with the Carina dSph, which is at a similar distance (~ 100 kpc; Mateo, 1998). Carina has a total mass of $\sim 2 \times 10^7 M_\odot$ and a mass-to-light ratio of ~ 70 . At least 75 RR Lyrae stars have been detected by Dall’Ora et al. (2003) using well-sampled multi-epoch data in the B and V bands, although over a small baseline of a few days.

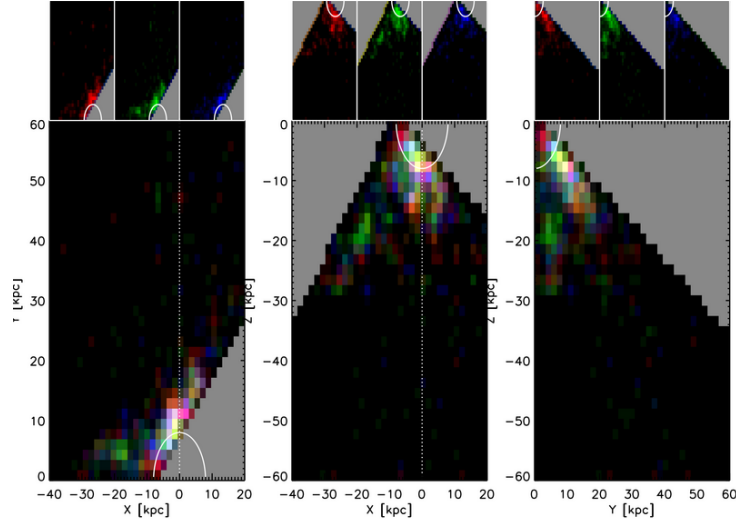


Figure 3.11: The density distributions of RR Lyrae candidates projected onto the principal planes of Galactocentric (x, y, z) coordinates. Here, red represents the high metallicity RR Lyrae population ($[\text{Fe}/\text{H}] > -1.3$), green medium ($-1.5 < [\text{Fe}/\text{H}] < -1.3$) and blue low ($[\text{Fe}/\text{H}] < -1.5$). The insets show each distribution plotted separately, together with a white circle centred at the origin. There is no obvious distinction according to metallicity, and the low, medium and high metallicity RR Lyraes are clearly distended and seemingly belong to the Hercules-Aquila Cloud. In particular, none of the populations is distributed in a spherically symmetric manner around the Galactic Centre.

Table 3.2: The range in Galactic coordinates and the means and dispersions in heliocentric distance, Galactocentric distance, period and metallicity of the RR Lyrae variables in the Hercules-Aquila Cloud, the Sagittarius Stream and the Pisces Overdensity.

	Hercules-Aquila Cloud	Sagittarius Stream	Pisces Overdensity
ℓ (deg)	[45°, 79°]	[139°, 182°]	[63°, 93°]
b (deg)	[-56°, -24°]	[-62°, -46°]	[-60°, -46°]
D (kpc)	21.9±12.1	26.1± 5.6	79.9±13.9
r (kpc)	20.1±11.3	31.4± 5.6	79.4±14.1
P (days)	0.51±0.12	0.54±0.12	0.56±0.08
[Fe/H]	-1.43±0.36	-1.43±0.30	-1.48±0.28

Assuming similar stellar populations and similar efficiencies of detection of bright RR Lyrae in the surveys, then we can use a simple scaling argument to estimate the total stellar mass associated with the Pisces Overdensity as $\sim 10^5 M_\odot$. We can corroborate this mass estimate by comparison with our data on the Hercules-Aquila Cloud. The calculation using the Hercules-Aquila Cloud has the advantage that the RR Lyrae populations in the two structures have been discovered by the same algorithm, but the disadvantage that the properties of the Cloud are also rather uncertain. The absolute magnitude of the Cloud is given by Belokurov et al. (2007) as $M_r = -13$, suggesting that its total stellar mass is $\sim 10^7 M_\odot$. Of course, the Cloud is an enormous structure, covering $\sim 80^\circ$ in longitude and probably extending above and below the Galactic plane by 50° . Only a small fraction (~ 1 per cent) of the Cloud is probed by the Stripe 82 data, suggesting that there must be $\sim 2 \times 10^4$ RR Lyraes associated with the Cloud in total. The mass of the Cloud covered by the Stripe is $\sim 10^5 M_\odot$. Again, assuming simi-

3 Substructure revealed by RR Lyraes in SDSS Stripe 82

lar stellar populations, the mass associated with the Pisces Overdensity is at least $\sim 10^4 M_{\odot}$, a value encouragingly similar to our first estimate.

Of the 28 stars identified as members of the Pisces Overdensity, the intrinsically faintest has $M_z = 0.76$. The stars extend over an area of 55 deg^2 of Stripe 82. Thus, the surface number density of the RR Lyraes is 0.51 deg^{-2} . By comparison, the Hercules-Aquila Cloud has 209 RR Lyraes with an absolute magnitude brighter than $M_z=0.76$. They cover 95 deg^2 of Stripe 82, and hence the surface number density is 2.20 deg^2 . This suggests that the Pisces Overdensity is ~ 4.33 times more diffuse than the Hercules-Aquila Cloud.

The distance and metallicity distributions of our RR Lyraes can be used to study the properties of the Hercules-Aquila Cloud, the Sagittarius Stream and the Pisces Overdensity. Plots are shown in Figure 3.9. The distribution of heliocentric distances for the Cloud has a mean of 22.0 kpc and a standard deviation of 12.1 kpc. One possible interpretation of the Cloud is that it is analogous to caustic features like the shells seen around elliptical galaxies. However, the considerable depth of the Cloud seen in the RR Lyrae distribution tends to argue against such an interpretation as a caustic structure.

In directions towards Stripe 82, the distances of the arms of the Sagittarius Stream are not well-known. Simulations offer a rough guide, but no more than that. The upper panel of Figure 3 of Fellhauer et al. (2006) shows the young leading arm (A), together with parts of the old trailing arm (B), at distances of 15-20 kpc; further, material belonging to parts of B, the old leading arm (C) and the young trailing arm (D) spread out over a swathe of distances 30-60 kpc. The distribution of distances of our Sagittarius RR Lyraes in Figure 3.9 does indeed show some evidence of bimodality. It is possible that the peak at distances $D \sim 20$ kpc corresponds to the A and B streams, whilst the peak at $D \sim 35$ kpc corresponds to the other wraps. However, the simulations also suggest that the second peak should be much broader than appears to be the case in the data. Our identifications are tentative and radial velocity data is required to enable a cleaner separation of the wraps, as is evident from the lower panel of Figure 3 of Fellhauer et al. (2006).

From Table 3.2, we see that the RR Lyrae in the Hercules-Aquila Cloud have a metallicity $[\text{Fe}/\text{H}] = -1.42 \pm 0.24$, whilst those associated with the Sagittarius Stream have $[\text{Fe}/\text{H}] = -1.41 \pm 0.19$. The Pisces Overdensity has a metallicity $[\text{Fe}/\text{H}] = -1.47 \pm 0.34$, comparable to the Hercules-Aquila Cloud, but richer than the typical populations in the outer halo, which have a metallicity of $[\text{Fe}/\text{H}] \sim -2$ (Carollo et al., 2007).

In fact, Vivas et al. (2005) have already carried out VLT spectroscopy of 14 RR Lyrae variables that lie in the leading arm of the Sagittarius Stream, finding a metallicity of $[\text{Fe}/\text{H}] = -1.76 \pm 0.22$. The stars lie well away from Stripe 82 at right ascensions $13^{\text{h}} < \alpha < 16^{\text{h}}$ and at heliocentric distances of ~ 50 kpc. Many of the RR Lyraes in our sample will belong to the trailing arm, which may account for some of the difference in the metallicity estimate.

We show a view of Stripe 82 as derived from SDSS main-sequence turn-off (MSTO) stars in Figure 3.12. The upper panel gives the number of MSTO stars as a function of right ascension and distance. The one-dimensional histogram plotted in black shows the dependence of number on right ascension alone. Note that the Sagittarius Stream is immediately visible at $\alpha \approx 2^{\text{h}} - 3^{\text{h}}$. There are two density maxima in the black histogram, perhaps hinting that more than one wrap of the Stream is detectable in MSTO stars. The Hercules-Aquila Cloud substructure also shows up very clearly, al-

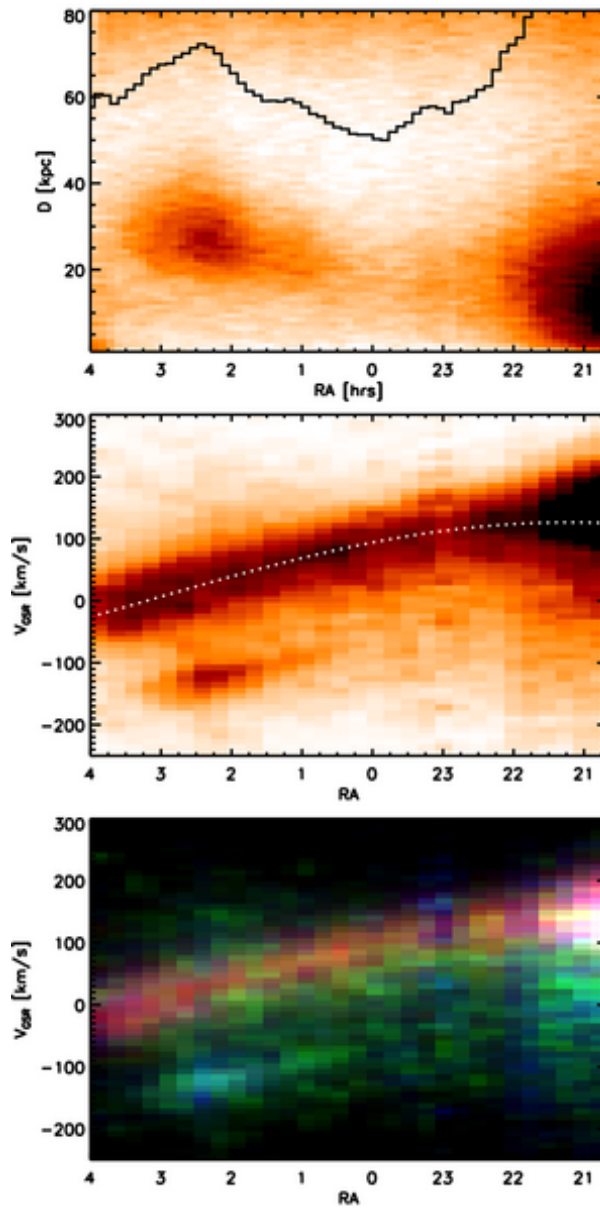


Figure 3.12: Top: The distributions of main sequence turn-off stars in Stripe 82 shown in the plane of right ascension versus heliocentric distance. The black histogram shows the one-dimensional distribution as a function of right ascension only. Middle: The velocity distribution of all stars with $g - i < 1$ with SDSS spectra. The white dashed curve shows the line $190 \sin \ell \cos b \text{ km s}^{-1}$ and marks the expected locus of stars belonging to the thick disk. Most thin disk stars are excised by the colour cut. Bottom: As middle, but the distribution is now colour-coded according to metallicity with red representing $[\text{Fe}/\text{H}] > -1$, green $-1.67 < [\text{Fe}/\text{H}] < -1$ and blue low $[\text{Fe}/\text{H}] < -1.67$. This separates the thin disk stars (reddish) from the older and metal-poor components of the stellar halo, such as the Hercules-Aquila Cloud.

3 Substructure revealed by RR Lyraes in SDSS Stripe 82

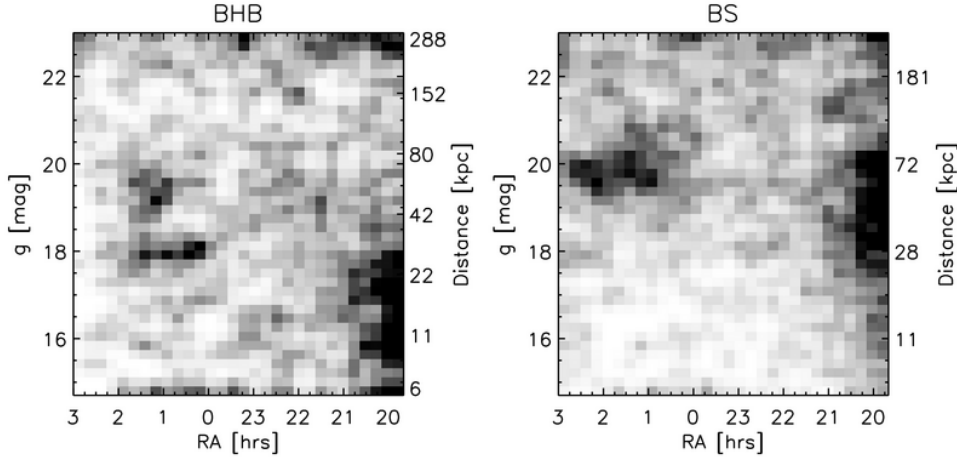


Figure 3.13: The distributions of BHB stars (left) and blue stragglers (right) in Stripe 82 shown in the plane of right ascension versus heliocentric distance.

though the fainter Pisces Overdensity is understandably absent. The distance estimates to the substructures derived from MSTO stars agree well with those from RR Lyraes. The SDSS DR6 includes a large number of stellar spectra which have been analysed to provide radial velocities and fundamental stellar atmospheric parameters (Lee et al., 2008). The velocities of all stars with spectra and satisfying $g - i < 1$, to remove most of the thin disk contaminants, are plotted against right ascension along Stripe 82 in the middle panel. Of course, most of the stellar targets are disk stars, and so the curve $v_{\text{GSR}} = 190 \cos b \sin \ell \text{ km s}^{-1}$ is plotted to show the locus of the thick disk in this dataset. The Sagittarius Stream stars are clearly offset in velocity from the thin disk at $v_{\text{GSR}} \approx -130 \text{ km s}^{-1}$. The bottom panel shows the same data, but now colour-coded according to metallicity so as to highlight different structures. We can detect the kinematically bifurcated Sagittarius Stream and clearly see the separation of the more metal-rich Galactic disk and bulge stars from the Hercules-Aquila Cloud. The eye can also discern some fainter substructure, the reality of which remains to be established.

A final view of Stripe 82 is provided in Figure 3.13, which shows the density distribution of blue horizontal branch stars (BHBs) and blue stragglers (BSs), selected using the colour cuts of Yanny et al. (2000). The BHB and RR Lyrae populations occupy adjacent, overlapping regions of the Hertzsprung-Russell diagram, thus we might expect to see all three substructures in the BHB density diagram – and so it is reassuring that the Sagittarius stream, the Hercules-Aquila cloud and the Pisces Overdensity are all visible. The same substructures are also identifiable in the BS populations with the exception of the Pisces Overdensity which is of course too distant. The Sagittarius Stream is clearly bifurcated in BHBs, although not in BSs, suggesting that the ratio of BHBs to BSs varies along the Stream. There is some evidence for bimodality in the BHB distance distribution of the Hercules-Aquila Cloud.

3.4 Summary

In this chapter, I have presented the extraction of a sample of RR Lyrae stars, **316** RRab types and **91** RRc types, from the variable catalogue described in Chapter 2, using a combination of cuts based on colour, period, amplitude and metallicity. The RR Lyraes lie at distances 5-115 kpc from the Galac-

tic centre and individual distance estimates, accurate to 5 per cent, are calculated using the colour, period and metallicity to estimate absolute magnitude.

If the RR Lyrae data are modelled by a smooth density distribution, then a good fit is provided by a broken power-law. The number density of RR Lyrae falls with Galactocentric radius r like $n(r) \sim r^{-2.4}$ for $5 < r < 23$ kpc, switching to a much steeper decline, $n(r) \sim r^{-4.5}$ for $23 < r < 100$ kpc. However, smooth, spherically-averaged density laws do not tell the whole story, as in reality the RR Lyrae distribution is strongly clumped. In Stripe 82, the distribution of RR Lyraes is dominated by three enormous substructures – namely, the Hercules-Aquila Cloud, the Sagittarius Stream and the Pisces Overdensity. We identified samples of **237** RR Lyraes in the Hercules-Aquila Cloud, **55** stars in the Sagittarius Stream and **28** in the Pisces Overdensity.

RR Lyraes belonging to the Hercules-Aquila Cloud are very numerous, and comprise almost 60 per cent of our entire Stripe 82 sample. Although there may be some contamination from a smooth component of RR Lyraes associated with the Galactic Bulge and Spheroid, there is no doubt concerning the existence of the structure, supporting the initial identification of Belokurov et al. (2007). We estimate that the total number of RR Lyraes associated with the Cloud is 2×10^4 . The Hercules-Aquila RR Lyraes lie at distances from the Galactic Centre of 20.2 ± 11.3 kpc, and are metal-poor with $[\text{Fe}/\text{H}] = -1.42 \pm 0.24$.

Both leading and trailing arms of the Sagittarius Stream also intersect Stripe 82. Simulations predict that the leading wrap is closer in heliocentric distance than the trailing, but the locations of the arms are not accurately known in this region of the sky. The heliocentric distances of our Sagittarius RR Lyraes, which predominantly are associated with the trailing arm, have a mean of 26.2 kpc and a dispersion of 5.5 kpc, whilst their metallicity is $[\text{Fe}/\text{H}] = -1.41 \pm 0.19$.

We have also identified a new concentration – the *Pisces Overdensity* – consisting of 28 RR Lyraes centred on Galactic coordinates of ($\ell \approx 80^\circ$, $b \approx -55^\circ$). This is one of the most distant clumps so far found in the halo, as the RR Lyrae lie at distances of ~ 80 kpc. Although the location is close to the Magellanic Plane, the Pisces Overdensity is much more distant than the Magellanic Clouds and may well be unrelated to any known component of the Galaxy. We have made an order-of-magnitude estimate of the total mass associated with the Overdensity as at least $\sim 10^4 M_\odot$. The associated RR Lyrae have a metallicity $[\text{Fe}/\text{H}] = -1.47 \pm 0.34$, comparable to the Hercules-Aquila Cloud, but richer than the typical populations in the outer halo.

This investigation has exploited the advantages of RR Lyrae stars for identifying remnants and substructure present in the halo of the Galaxy. Together with earlier SDSS discoveries (Belokurov et al., 2007; Juric et al., 2008), the patchy and clumpy nature of the RR Lyrae distribution adds support to the picture of an outer halo composed of overdensities and voids, perhaps entirely devoid of any smooth component (e.g. Bell et al., 2008). Further study of the kinematics and metallicities of RR Lyraes in Stripe 82 should lead to a major advance in our understanding of the Galactic halo, albeit that significant observational resources will be required to acquire the necessary follow-up spectroscopy.

4

Masses of the Milky Way and Andromeda Galaxies

The structure and extent of dark matter haloes have important implications for modern astrophysics, yet the determination of such properties is a difficult task and the results are often conflicting. A clear illustration is provided by the usage of Sagittarius Stream data to constrain the shape of the MW dark halo. Data obtained from the SDSS and 2MASS, two of the deepest and most comprehensive surveys of the last decade, has told us that the halo is nearly spherical (Fellhauer et al., 2006), prolate (Helmi, 2004), oblate (Johnston et al., 2005) or triaxial (Law et al., 2009) in nature! The MW is the closest halo available for our study, the availability of data has improved substantially in recent years and the quality of that data is unprecedented, and yet we are not able to determine its shape reliably.

Similarly, we are unable to measure the masses of the MW, or its neighbour M31 with any precision. Despite their proximity to us, their masses remain sketchily determined and there is some controversy as to which halo is more massive. Judged by criteria such as the surface brightness of the stellar halo or the numbers of GCs or the amplitude of the gas rotation curve, M31 is seemingly the more massive. Judged by criteria such as the velocities of the satellite galaxies and distant globulars or tidal radii of the dSphs, then the MW is seemingly the more massive. For example, Evans et al. (2000) argued that the M31 halo is roughly as massive as that of the MW, with the MW marginally being the more massive of the two, while recent studies have found evidence favouring both the MW (e.g. Evans & Wilkinson, 2000; Gottesman et al., 2002) and M31 (e.g. Klypin et al., 2002; Karachentsev et al., 2009) as the more massive galaxy.

The masses of both haloes within a few tens of kiloparsecs are reasonably well constrained by gas rotation curve data (e.g. Rohlfs & Kreitschmann, 1988; Braun, 1991). However, these data only sample the inner parts of the haloes. In order to probe further out, we must turn to the kinematics of the satellite populations. Such tracers are a valuable tool for studying the dark matter haloes as their orbits contain important information about their host potential. Distance, radial velocity and proper motion data can be used to constrain halo extent, mass and velocity anisotropy (see e.g. Little & Tremaine, 1987; Zaritsky et al., 1989; Kochanek, 1996; Wilkinson & Evans, 1999).

The uncertainties in the mass estimates for the MW and M31 are largely due to the fact that there is seldom proper motion data available to complement distance and radial velocity information. With

4 Masses of the Milky Way and Andromeda Galaxies

only one velocity component to work with, the eccentricities of the orbits are poorly constrained. Statistical methods must be applied to determine masses and these methods suffer greatly from the small sample sizes available, even with the recent burst of satellite discoveries associated with both galaxies.

The projected mass estimator was introduced by Bahcall & Tremaine (1981). They assumed that only projected distance and line-of-sight velocity information was available. The estimator is also contained in the study of White (1981) on scale-free ensembles of binary galaxies. The analysis was extended by Heisler et al. (1985) and further modified by Evans et al. (2003) to consider the case of tracer populations. These previous studies successfully used the mass estimator to weigh M31. However, in its present form, the mass estimator is ill-suited for application to the MW and such a study has not yet been attempted. Further, previous studies have not had access to proper motion data for any of the objects under consideration, so the estimator deals only with line-of-sight velocity information.

Here, I develop alternative forms of the estimator and analyse the conditions under which they are valid; the estimators are presented in Section 4.1 and rigorously checked in Section 4.2. The census of satellites around M31 has increased significantly (Zucker et al., 2004, 2007; Martin et al., 2006; Majewski et al., 2007; Ibata et al., 2007; Irwin et al., 2008; McConnachie et al., 2008) since the last studies of this type were attempted and so there is much more data available, hence, I apply the estimator to M31 with these new data. In addition, the new estimators include one such tailored towards use with MW data so I also estimate the mass of the MW. Further, a handful of MW satellites have proper motion data so I also investigate the addition of proper motion data and what advantages such data can contribute. The mass estimates are calculated in Section 4.3 and discussed in Section 4.4 before I conclude in Section 4.5.

4.1 Mass estimators

The projected mass estimator (Bahcall & Tremaine, 1981) takes the form

$$M = \frac{C}{G} \langle v_{\text{los}}^2 R \rangle = \frac{C}{G} \frac{1}{N} \sum_{i=1}^N v_{\text{los},i}^2 R_i \quad (4.1)$$

for a set of N tracers objects (e.g planetary nebulae, stars, GCs, dSph galaxy satellites) with line-of-sight velocities v_{los} and projected distances R . Here, G is the gravitational constant and C is a constant determined by the host potential and the eccentricity of the orbits. They found that $C = \frac{16}{\pi}$ for test particles with an isotropic velocity distribution orbiting a point mass and $C = \frac{32}{\pi}$ for test particles moving on radial orbits.

This analysis was extended by Heisler et al. (1985) to consider the case in which tracers may track the total mass (e.g. in galaxy groups). They found that $C = \frac{32}{\pi}$ for particles with an isotropic velocity distribution and $C = \frac{64}{\pi}$ for particles on radial orbits. A key assumption in this work is that the members/tracers track the mass of the group/host. This is not true for all tracer populations, particularly for those tracers which are commonly used to estimate the masses of ellipticals or the haloes of spiral galaxies.

4.1.1 Tracer Mass Estimator

Here, we give a formal derivation of our tracer estimators, so as to clarify the conditions under which they converge to the enclosed mass. Readers primarily interested in applications, and willing to take convergence on trust, should skip straight to the estimators themselves, namely equations (4.16), (4.23), (4.24) and (4.26). We give formulae for the various cases in which true distances or projected distances, and line-of-sight velocities, or radial velocities or proper motions, are known for the tracers. The estimators are both simple and flexible.

Let us begin by supposing that the observations are discrete positions r and radial velocities v_r of N members of a tracer population. Here, r is measured from the centre of the host galaxy, whilst $v_r = \dot{r}$ is the radial velocity. We propose to combine the positional and kinematic data to give the enclosed mass M in the form

$$M = \frac{C}{G} \langle v_r^2 r^\lambda \rangle = \frac{C}{G} \frac{1}{N} \sum_{i=1}^N v_{r,i}^2 r_i^\lambda. \quad (4.2)$$

Here, unlike equation (4.1), the constant C is not necessarily dimensionless. Notice that *a priori* we do not know the best choice for λ . This will emerge from our analysis.

If f is the phase space distribution function of the tracers and σ_r the radial velocity dispersion, we see that under the assumption of spherical symmetry:

$$\langle v_r^2 r^\lambda \rangle = \frac{1}{M_t} \int d^3\mathbf{r} d^3\mathbf{v} f v_r^2 r^\lambda = \frac{4\pi}{M_t} \int \rho \sigma_r^2 r^{\lambda+2} dr \quad (4.3)$$

where M_t is the mass in the tracers

$$M_t = 4\pi \int r^2 \rho dr. \quad (4.4)$$

Now, let us assume that the tracer population is spherically symmetric and has a number density which falls off like a power-law

$$\rho(r) \propto r^{-\gamma}; \quad \frac{d \log \rho}{d \log r} = -\gamma \quad (4.5)$$

at least within the radius interval $[r_{\text{in}}, r_{\text{out}}]$ where the data lie. Then, the estimator reduces to

$$\langle v_r^2 r^\lambda \rangle = \frac{1}{\mathcal{M}} \int_{r_{\text{in}}}^{r_{\text{out}}} r^{\lambda-\gamma+2} \sigma_r^2 dr; \quad \mathcal{M} = \begin{cases} \frac{r_{\text{out}}^{3-\gamma} - r_{\text{in}}^{3-\gamma}}{3-\gamma} & (\gamma \neq 3) \\ \log \left(\frac{r_{\text{out}}}{r_{\text{in}}} \right) & (\gamma = 3) \end{cases}, \quad (4.6)$$

where $\log x$ is the natural logarithm. Once the behaviour of σ_r^2 is found, we may relate this estimator to the dynamical halo mass $M(r)$. This can be achieved through solving the Jeans equation, which reads:

$$\frac{1}{\rho} \frac{d(\rho \sigma_r^2)}{dr} + \frac{2\beta \sigma_r^2}{r} = -\frac{GM(r)}{r^2}. \quad (4.7)$$

Here, we have introduced $\beta = 1 - \sigma_t^2/2\sigma_r^2$, the Binney anisotropy parameter, in which σ_t is the

4 Masses of the Milky Way and Andromeda Galaxies

tangential velocity dispersion. Now, $\beta \rightarrow \infty$ corresponds to a circular orbit model, $\beta = 1$ corresponds to purely radial orbits and $\beta = 0$ is the isotropic case.

We note that the Jeans equation (4.7) in a spherical system can be put into the form

$$Q\rho\sigma_r^2 = - \int Q\rho \frac{GM(r)}{r^2} dr; \quad \log Q = \int \frac{2\beta}{r} dr. \quad (4.8)$$

If β is independent of r , this simplifies to be $Q = r^{2\beta}$.

To proceed further, the underlying gravity field is assumed to be scale-free at least in the interval $[r_{\text{in}}, r_{\text{out}}]$, that is, the relative potential up to a constant is given by

$$\psi(r) = \begin{cases} \frac{v_0^2}{\alpha} \left(\frac{a}{r}\right)^\alpha & (\alpha \neq 0) \\ v_0^2 \log\left(\frac{a}{r}\right) & (\alpha = 0) \end{cases} \quad (4.9)$$

with $-1 \leq \alpha \leq 1$.¹ Here, a is a fiducial radius, which should lie in the region for which the power-law approximation for the relative potential is valid (i.e., $r_{\text{in}} \leq a \leq r_{\text{out}}$) and v_0 is the circular speed at that radius a . When $\alpha = 1$, this corresponds to the case in which the test particles are orbiting a point-mass; when $\alpha = 0$, the satellites are moving in a large-scale mass distribution with a flat rotation curve; when $\alpha = \gamma - 2$, the satellites track the total gravitating mass. We remark that our model of a scale-free tracer population of satellites in a scale-free potential has previously been used to study the mass of the MW by Kulessa & Lynden-Bell (1992), although using the standard technique of maximum likelihood for parameter estimation.

The scale-free assumption is also equivalent to proposing the halo mass profile to be

$$\frac{M(r)}{M(a)} = \left(\frac{r}{a}\right)^{1-\alpha}, \quad (4.10)$$

and the local mass density $\propto r^{-(\alpha+2)}$. Consequently, if the power-law behaviour were allowed to be extended to infinity, the total mass of the dark halo would necessarily be infinite unless $\alpha = 1$. (However, if the halo density were to fall off faster than r^{-3} and so the total gravitating mass is finite, the leading term for the potential would be Keplerian. That is to say, for the case of a finite total mass halo, the gravity field experienced by the tracers may be approximated to be that of a point mass, given that r_{in} is chosen to be sufficiently large so that the gravitating mass inside the sphere of r_{in} dominates the mass within the shell region populated by the tracers.)

Combining this with the constant-anisotropy assumption, the Jeans equation integrated between r and r_{out} then reduces to

$$r^{2\beta-\gamma}\sigma_r^2(r) - r_{\text{out}}^{2\beta-\gamma}\sigma_r^2(r_{\text{out}}) = \frac{GM(a)}{a^{1-\alpha}} \int_r^{r_{\text{out}}} \tilde{r}^{2\beta-\gamma-\alpha-1} d\tilde{r}. \quad (4.11)$$

provided that all our assumptions remain valid in the radius interval $[r_{\text{in}}, r_{\text{out}}]$ and $r, a \in [r_{\text{in}}, r_{\text{out}}]$.

¹ $\alpha = -1$ corresponds to the gravitational field that pulls with an equal magnitude force regardless of radius, which is formally generated by a halo density falling off as r^{-1} . Provided we regard the scale-free potential as an approximation valid over a limited range and not extending to spatial infinity, we can permit $\alpha \geq -2$, since $\alpha = -2$ corresponds to the harmonic potential generated by a homogeneous sphere.

Now, our goal is to find the total halo mass. In reality, the observed tracers are only populated up to a finite outer radius, and so, any mass distribution outside of that radius does not affect our observations in a strictly spherical system (Newton's theorem). We therefore extend the power-law potential assumption only up to the finite outer radius (here r_{out}), and set $a = r_{\text{out}}$. In other words, the halo mass that we are interested in is that contained within the outer radius, $M = M(r_{\text{out}})$. With $a = r_{\text{out}}$, solving equation (4.11) for $\sigma_r^2(r)$ results in (here $s \equiv r/r_{\text{out}}$)

$$\sigma_r^2 = \begin{cases} \frac{\sigma_r^2(r_{\text{out}}) - \hat{v}_0^2}{s^{2\beta-\gamma}} + \frac{\hat{v}_0^2}{s^\alpha} & (\alpha + \gamma - 2\beta \neq 0) \\ \frac{\sigma_r^2(r_{\text{out}}) - v_0^2 \log s}{s^\alpha} & (\alpha = 2\beta - \gamma) \end{cases} \quad (4.12)$$

where $v_0^2 = GM/r_{\text{out}}$ is the circular speed at r_{out} whilst $\hat{v}_0^2 \equiv v_0^2/(\alpha + \gamma - 2\beta)$.

Then, substituting the result of equation (4.12) into equation (4.6) and explicitly performing the integration yields (ignoring particular parameter combinations that involve the logarithm)

$$\frac{\langle v_r^2 r^\lambda \rangle}{(3-\gamma)r_{\text{out}}^\lambda} = \frac{v_0^2}{(\lambda - \alpha + 3 - \gamma)(\alpha + \gamma - 2\beta)} \frac{1 - u^{\lambda - \alpha + 3 - \gamma}}{1 - u^{3-\gamma}} + \frac{1}{\lambda - 2\beta + 3} \left[\sigma_r^2(r_{\text{out}}) - \frac{v_0^2}{\alpha + \gamma - 2\beta} \right] \frac{1 - u^{\lambda - 2\beta + 3}}{1 - u^{3-\gamma}} \quad (4.13)$$

where $u \equiv r_{\text{in}}/r_{\text{out}}$. Notice now that the choice of $\lambda = \alpha$ makes the u -dependence of the first term in the right-hand side drop out. In fact, this could also have been deduced on dimensional grounds by requiring that our estimator is not dominated by datapoints at small radii or large radii.

The last terms in equation (4.13) basically constitute the surface 'pressure' support terms in the Jeans equation, which we wish to minimize as $u \rightarrow 0$. Here, we limit ourselves to the case that $\lambda = \alpha$, when the corresponding leading term is

$$\frac{1 - u^{\alpha - 2\beta + 3}}{1 - u^{3-\gamma}} \sim \begin{cases} 1 & 2\beta - \alpha, \gamma < 3 \\ -u^{-(2\beta - \alpha - 3)} & \gamma < 3 < 2\beta - \alpha \\ -u^{\gamma - 3} & 2\beta - \alpha < 3 < \gamma \\ u^{\alpha + \gamma - 2\beta} & 3 < 2\beta - \alpha, \gamma \end{cases}. \quad (4.14)$$

In other words, provided that $\gamma > 3$ and $\gamma > 2\beta - \alpha$, the pressure term vanishes as $u \rightarrow 0$, and we obtain the scale-free Jeans solutions of Evans et al. (1997). In fact, since $\beta \leq 1$ and $-1 \leq \alpha \leq 1$, we find that $2\beta - \alpha \leq 3$ and thus the second condition here is essentially redundant. Consequently, provided that $\gamma > 3$, that is the tracer density falls off more quickly than r^{-3} , we find the estimator to be

$$\langle v_r^2 r^\alpha \rangle \simeq \frac{r_{\text{out}}^\alpha}{\alpha + \gamma - 2\beta} \frac{GM}{r_{\text{out}}} + \mathcal{R} \quad (4.15)$$

where the remainder $\mathcal{R} \rightarrow 0$ vanishes as $r_{\text{in}}/r_{\text{out}} \rightarrow 0$ (here, r_{in} and r_{out} are the inner and outer radius of the tracer population).

Alternatively, if $\gamma < 3$ and $2\beta - \alpha < 3$, the remainder term tends to a constant as $u \rightarrow 0$. In a

4 Masses of the Milky Way and Andromeda Galaxies

perfectly scale-free halo traced by again strictly scale-free populations, this constant must be zero. This is because, for such a system, σ_r^2 should also be scale-free. Yet equation (4.12) implies that this is possible only if $\sigma_r^2(r_{\text{out}}) = \hat{v}_0^2$. Subsequently this also indicates that the coefficient for the remainder in equation (4.13) vanishes too. Even after relaxing the everywhere strict power-law behaviour, we would expect that $\sigma_r^2 \sim \hat{v}_0^2$ and consequently that $|\sigma_r^2 - \hat{v}_0^2| \ll \hat{v}_0^2$, provided that $2\beta - \alpha < \gamma$, which is required to ensure $\hat{v}_0^2 > 0$. That is to say, we expect that $\hat{v}_0^2 r_{\text{out}}^\alpha \gg \mathcal{R}$ as $u \rightarrow 0$ in equation (4.15) for $2\beta - \alpha < \gamma < 3$, which is sufficient for justifying the applicability of our mass estimator.

In other words, we have obtained a very simple result

$$M = \frac{C}{G} \langle v_r^2 r^\alpha \rangle, \quad C = (\alpha + \gamma - 2\beta) r_{\text{out}}^{1-\alpha}, \quad (4.16)$$

provided that $C > 0$ (the simple interpolative argument indicates that this is still valid for $\gamma = 3$). This corresponds to the case in which the tracers have known radial velocity components v_r resolved with respect to the centre of the galaxy, as well as actual distances r . For satellites of the MW, the line of sight velocity v_{los} is measured, and corrected to the Galactic rest frame. Now, v_r may be calculated from v_{los} only if proper motion data exists. Alternatively, a statistical correction can be applied to estimate v_r from v_{los}

$$\langle v_r^2 \rangle = \frac{\langle v_{\text{los}}^2 \rangle}{1 - \beta \sin^2 \varphi} \quad (4.17)$$

where φ is the angle between the unit vector from the Galactic Centre to the satellite and the unit vector from the Sun to the satellite.

Note too that in the important isothermal case ($\alpha = 0$), the galaxy rotation curve is flat with amplitude v_0 . Then, for members of a population with density falling like $\rho \sim r^{-3}$, such as the Galactic GCs, equation (4.16) reduces to

$$v_0^2 = (3 - 2\beta) \langle v_r^2 \rangle. \quad (4.18)$$

This is a generalization of the estimator of Lynden-Bell & Frenk (1981) to the case of anisotropy. When the population is isotropic ($\beta = 0$), it reduces to the appealing simple statement that the circular speed is the rms velocity of the tracers multiplied by $\sqrt{3} \approx 1.732$.

Even if three dimensional distance r is replaced by projected distance R or v_r by some other projections of the velocity, the basic scaling result of equation (4.16) remains valid. Different projections simply result in distinct constants C , as we now show.

4.1.2 A Family of Estimators

Now, suppose that we have actual distances r from the centre of the host galaxy, but only projected or line of sight velocities v_{los} . This is the case for many of M31's satellite galaxies, for which distances have been measured by using the tip of the red giant branch method (see e.g., McConnachie et al., 2005) and for which projected velocities are known from spectroscopy. The calculation proceeds by considering

$$\langle v_{\text{los}}^2 r^\alpha \rangle = \frac{1}{M_t} \int d^3\mathbf{r} d^3\mathbf{v} f v_{\text{los}}^2 r^\alpha = \frac{2\pi}{M_t} \int_{r_{\text{in}}}^{r_{\text{out}}} dr \int_0^\pi d\theta \rho \sigma_{\text{los}}^2 r^{\alpha+2} \sin\theta \quad (4.19)$$

We now need the relationship between line-of-sight velocity dispersion σ_{los} and the radial velocity dispersion σ_r , namely

$$\sigma_{\text{los}}^2 = \sigma_r^2 (1 - \beta \sin^2 \varphi), \quad (4.20)$$

which is similar to equation (4.17) but here the angle φ is the angle between the line of sight and the position vector of the satellite with respect to the centre of the *host galaxy* (see e.g., Binney & Tremaine, 1987, Section 4.2). If the polar z -axis of the coordinate system is chosen such that the sun (that is, the observer) lies on the negative z -axis (i.e., $\theta = \pi$) at a distance d from the centre of the host galaxy, we find that

$$\sin^2 \varphi = \frac{\sin^2 \theta}{1 + 2\frac{r}{d} \cos \theta + \left(\frac{r}{d}\right)^2}. \quad (4.21)$$

However, for most external galaxies, it is reasonable to assume $d \gg r_{\text{out}}$, and therefore, we can safely approximate² that $\sin^2 \varphi \approx \sin^2 \theta$. Then,

$$\langle v_{\text{los}}^2 r^\alpha \rangle = \langle v_r^2 r^\alpha \rangle \int_0^{\pi/2} d\theta \sin \theta (1 - \beta \sin^2 \theta), \quad (4.22)$$

and thus we find that

$$M = \frac{C}{G} \langle v_{\text{los}}^2 r^\alpha \rangle, \quad C = \frac{3(\alpha + \gamma - 2\beta)}{3 - 2\beta} r_{\text{out}}^{1-\alpha}. \quad (4.23)$$

Next, we consider the case in which we have full velocity information for the satellites, i.e., both radial velocities and proper motions. For example, this is the case for a subset of the satellites of the MW (see e.g., Piatek et al., 2002). In this case, we can utilize $\sigma^2 = \sigma_r^2 + \sigma_t^2 = (3 - 2\beta)\sigma_r^2$, and therefore the estimator becomes

$$M = \frac{C}{G} \langle v^2 r^\alpha \rangle, \quad C = \frac{\alpha + \gamma - 2\beta}{3 - 2\beta} r_{\text{out}}^{1-\alpha}. \quad (4.24)$$

Finally, we can assume a worst-case scenario in which the only data available are projected distances R and line-of-sight velocities v_{los} for the tracers. Outside of the galaxies of the LG, this is the usual state of affairs. So, this would be the form of the estimator to find the dark matter mass of nearby giant ellipticals like M87 from positions and velocities of the GCs. The estimator is derived following the same procedure with $R = r \sin \theta$, which results in the relation

$$\langle v_{\text{los}}^2 R^\alpha \rangle = \langle v_r^2 r^\alpha \rangle \int_0^{\pi/2} d\theta \sin^{\alpha+1} \theta (1 - \beta \sin^2 \theta). \quad (4.25)$$

Consequently, the corresponding estimator is found to be³

²On the other hand, for the satellites of the MW, it is often assumed that $d \ll r_{\text{in}}$, which leads to $\sin \varphi \approx 0$ and consequently $\langle v_{\text{los}}^2 r^\alpha \rangle \approx \langle v_r^2 r^\alpha \rangle$.

³The result is valid provided that the integral is limited to spherical shells. However, given the lack of depth

4 Masses of the Milky Way and Andromeda Galaxies

$$M = \frac{C}{G} \langle v_{\text{los}}^2 R^\alpha \rangle, \quad C = \frac{(\alpha + \gamma - 2\beta)}{I_{\alpha,\beta}} r_{\text{out}}^{1-\alpha} \quad (4.26)$$

where

$$I_{\alpha,\beta} = \frac{\pi^{1/2} \Gamma(\frac{\alpha}{2} + 1)}{4\Gamma(\frac{\alpha}{2} + \frac{5}{2})} [\alpha + 3 - \beta(\alpha + 2)] \quad (4.27)$$

and $\Gamma(x)$ is the gamma function. This case is related to work by Bahcall & Tremaine (1981). So, for example, in the Keplerian case ($\alpha = 1$), a distribution of test particles with $\gamma = 3$ gives

$$C = \frac{32}{\pi} \frac{2 - \beta}{4 - 3\beta} \quad (4.28)$$

When $\beta = 0$, this implies that $C = 16/\pi$; whilst when $\beta = 1$, $C = 32/\pi$.

Some of these estimators are implicit in earlier work. In particular, some are equivalent to those introduced by White (1981), who had a different focus on the dynamics of binary galaxies but who made the same scale-free assumptions to obtain robust mass estimators. Very recently, An & Evans (2010, in preparation) found a related family of estimators that are independent of parameters derived from the tracer density (such as γ).

4.2 Checks with Monte Carlo Simulations

In order to verify the correctness of our mass estimators, we generate synthetic data-sets of anisotropic spherical tracer populations. Distances r are selected in $[r_{\text{in}}, r_{\text{out}}]$ assuming the power-law density profile in equation (4.5). Projection directions are determined by the position angles: $\cos \theta$ is generated uniformly in $[-1, 1]$ and ϕ is generated uniformly in $[0, 2\pi]$. If R lies outside of the allowed range, the projection direction is regenerated until R is within $[R_{\text{in}}, R_{\text{out}}]$.

The phase-space distribution functions that give rise to such density profiles are given in Evans et al. (1997). Tracer velocities are picked from the distributions

$$f(v) \propto \begin{cases} v^{2-2\beta} \left| \psi(r) - \frac{1}{2}v^2 \right|^{[2\gamma-3\alpha-2\beta(2-\alpha)]/(2\alpha)} & (\alpha \neq 0) \\ v^{2-2\beta} \exp\left(-\frac{v^2}{2\sigma^2}\right) & (\alpha = 0) \end{cases} \quad (4.29)$$

For $\alpha > 0$, the maximum velocity at any position is $\sqrt{2\psi(r)}$; for $\alpha \leq 0$, the velocities can become arbitrarily large. Following Binney & Tremaine (1987), we introduce spherical polar coordinates in velocity space (v, ξ, η) so that the velocities resolved in spherical polar coordinates with respect to the centre are then

$$v_r = v \cos \eta \quad v_\theta = v \sin \eta \cos \xi \quad v_\phi = v \sin \eta \sin \xi \quad (4.30)$$

To generate velocities with the correct anisotropy, ξ is generated uniformly in $[0, 2\pi]$ and η is information, it might seem more logical to perform the integration over cylindrical shells. Unfortunately, the result is more complicated, as it involves the integrals of incomplete beta functions.

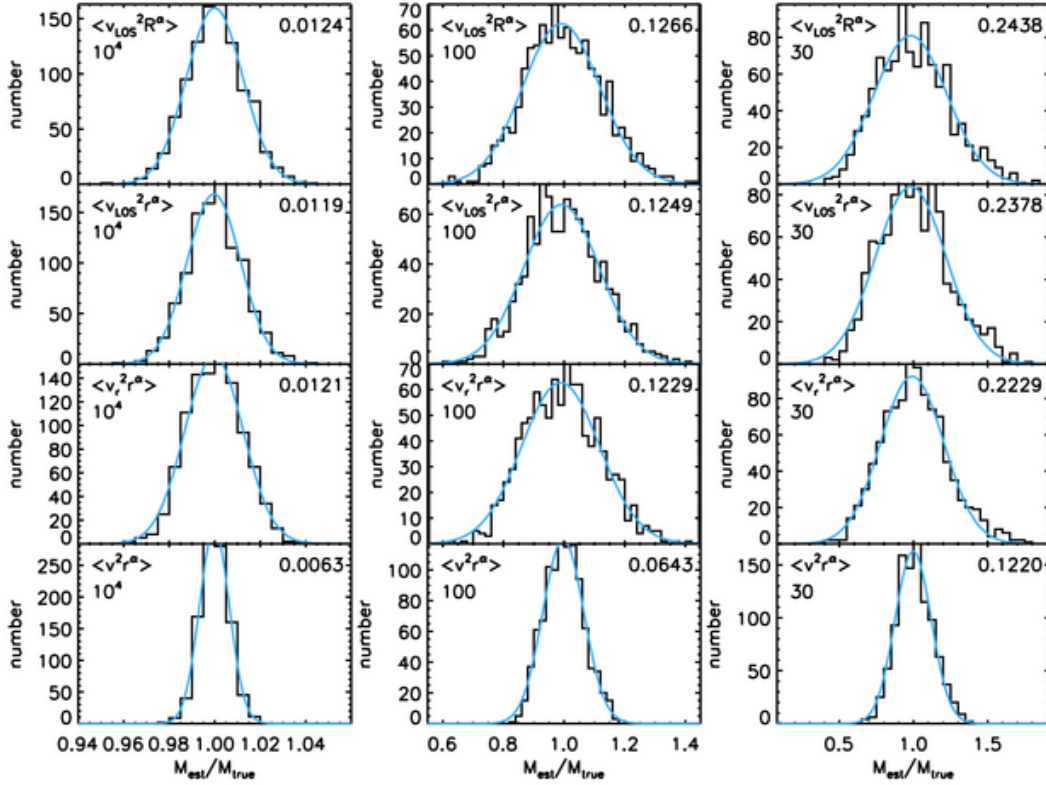


Figure 4.1: Distribution of mass estimate as a fraction of the true mass for 1000 Monte Carlo realisations, assuming that parameters α , β and γ are known exactly. Left: $N = 10,000$. Middle: $N = 100$. Right: $N = 30$. The number of satellites in the simulation and the form of the estimator used to recover the mass is shown in the top left corner of each panel. A best-fit Gaussian is plotted for each distribution and the standard deviation of the distribution is shown in the top right corner of each panel. On average, the tracer mass estimator recovers the true mass of the host. [The cases shown correspond to $\alpha = 0.55$, $\beta = 0.0$ and $\gamma = 2.7$].

picked in $[0, \pi]$ from the distribution

$$F(\eta) \propto |\sin \eta|^{1-2\beta} \quad (4.31)$$

where β is the Binney anisotropy parameter. Finally, the line-of-sight velocities are calculated and used in the tracer mass estimator.

Figure 4.1 shows the distribution of mass estimates as fractions of the true mass for 1000 realisations, assuming that parameters α , β and γ are known exactly; the left panels show simulations with 10,000 tracers, the middle panels for 100 tracers and the right panels for 30 tracers. The panels use the different forms of the estimator given in equations (4.16), (4.23), (4.24) and (4.26) respectively. A Gaussian with the same standard deviation as each distribution is also plotted for each panel. The standard deviation is included in the top-right corner of each plot and gives an estimate of the error in each case.

We see that our mass estimators are unbiased – that is, on average, the true mass is recovered in all cases. The benefit of using three dimensional distances r instead of projected distances R is modest, as is the improvement gained by using v_r in place of v_{los} . However, if proper motion data are

4 Masses of the Milky Way and Andromeda Galaxies

available, then using v instead of v_r gives a more accurate mass estimate.

So far, we have assumed that we know α , β and γ exactly, which is, of course, not the case. Our estimates for α , β and γ have errors associated with them, not least because the notion of a scale-free density profile in a scale-free potential is an idealization. As these parameters enter the estimator through the prefactor C , it is straightforward to obtain the additional uncertainty in the final answer using propagation of errors. As we will show in the next section α and γ are constrained either by cosmological arguments or by the data. The right-most column in Figure 4.1 (a host with 30 satellites) is the most applicable to our data-sets at present as the MW has 26 satellites and M31 23 satellites with a recorded line-of-sight velocity. The error on the mass estimate obtained in this case is $\sim 25\%$. This is much larger than that the effects of errors on α and γ and so the latter will be ignored for the rest of the discussion.

However, the case of the velocity anisotropy β is different as it is poorly constrained, with theory and data pointing in rather different directions. Changes in β can therefore make a substantial difference to the mass estimate.

Note that these simulations yield no insight into systematic errors because the mock data are drawn from the same distribution functions used to derive the form of the mass estimators. This is a concern as there are a number of causes of systematic error - for example, dark halos may not be spherical, or infall may continue to the present day so that the observed satellites may not necessarily be virialized. Deason et al. (2010) have tested the estimators derived in this paper, as well as a number of other commonly used estimators, against simulations. Specifically they extracted samples of MW-like galaxies and their satellites from the *Galaxies Intergalactic Medium Interaction Calculation* (Crain et al., 2009), a recent high-resolution hydrodynamical simulation of a large volume of the Universe. They find that the estimators in this paper significantly out perform the projected mass estimator of Evans et al. (2003).

Let us emphasize then that only random errors are assessed in this paper. Systematic errors from, for example, non-sphericity, non-equilibrium dynamics, and radial variations in parameters will normally exist as well. To address this requires comparison to N -body simulations. Such an analysis will be presented in a separate follow-up paper (Deason et al., 2010).

4.3 Mass Estimates for Andromeda and the Milky Way

4.3.1 Choice of Power-Law Index Parameters

We now apply the mass estimators to the MW and M31, the two largest galaxies in the LG. In converting heliocentric quantities to Galactocentric ones, we assume a circular speed of 220 km s^{-1} at the Galactocentric radius of the sun ($R_{\odot} = 8.0 \text{ kpc}$)⁴ and a solar peculiar velocity of $(U, V, W) = (10.00, 5.25, 7.17) \text{ km s}^{-1}$, where U is directed inward to the Galactic Centre, V is positive in the direction of Galactic rotation at the position of the sun, and W is positive towards the North Galactic Pole (see e.g., Dehnen & Binney, 1998).

⁴Reid et al. (2009) have argued that the parallaxes and proper motions of maser sources suggest that the circular rotation speed is probably closer to 250 km s^{-1} and the distance to the Galactic Centre is $\sim 8.4 \text{ kpc}$. We have checked that using these values makes only very modest changes to our mass estimates for the MW.

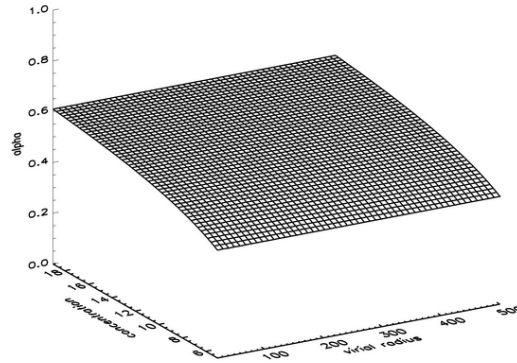


Figure 4.2: The best-fit value of the potential power-law index α to an NFW potential as a function of the concentration and virial radius. Note that for plausible values of the concentration c and the virial radius r_{vir} for galaxies like the MW and M31, α lies in the range 0.5-0.6. The surface is smooth and flattish, implying that α is reasonably insensitive to the details of the NFW potential.

For the M31 satellites, positional and velocity data must be computed relative to M31 itself. We take the position of M31 to be $(\ell, b) = (121.2^\circ, -21.6^\circ)$ at a distance of 785 kpc and its line-of-sight velocity to be -123 km s^{-1} in the Galactic rest frame (see e.g. McConnachie et al., 2005; McConnachie & Irwin, 2006b).

In order to apply our estimators to these systems, we need to compute the power-law index of the host potential α , the velocity anisotropy β and the power-law index of the satellite density distribution γ . There are cosmological arguments suggesting that the potentials of dark haloes are well-approximated by Navarro-Frenk-White (NFW) profiles (Navarro et al., 1996). Figure 4.2 shows the best-fit power-law to the NFW potential for a wide range of concentrations and virial radii. The fitting is performed in the region $10 < r/\text{kpc} < 300$, which is where the majority of the satellites lie. Now, Klypin et al. (2002) argued that the concentrations of the MW and M31 are $c \approx 12$, whilst the virial radii r_{vir} are in the range 250-300 kpc. In other words, for the range of concentrations and virial radii appropriate to galaxies like the MW and M31, we see – fortunately – that the surface in Figure 4.2 is slowly-changing and flattish with $\alpha \approx 0.55$.

If the satellite number density distribution $n(r)$ follows a power law with index γ , then the number of satellites within any radius, $N(< r)$, also follows a power-law with index $3 - \gamma$. We fit power-laws to the MW and M31 satellite cumulative distributions in order to estimate γ . We restrict ourselves to the inner regions of the satellite distributions, $r \leq 300 \text{ kpc}$; beyond this range, the satellite population is likely to be seriously incomplete. The distributions and the best-fitting power laws are shown in Figure 4.3; the MW data is shown in the upper panel and M31 data is shown in the lower panel. We find $\gamma = 2.6$ for the MW and $\gamma = 2.1$ for M31. Note that data from the Sloan Digital Sky Survey (SDSS; York et al., 2000) has been instrumental in the identification of many of the recently-discovered MW dwarfs. The SDSS coverage includes only the region around the North Galactic Cap, and, as such, the distribution of known MW satellites is concentrated in that area of the sky. However, given our underlying assumption that the distribution of satellites is spherically symmetric, this directional bias does not impair our mass estimators. A bigger worry may be the incompleteness in the satellite dis-

4 Masses of the Milky Way and Andromeda Galaxies

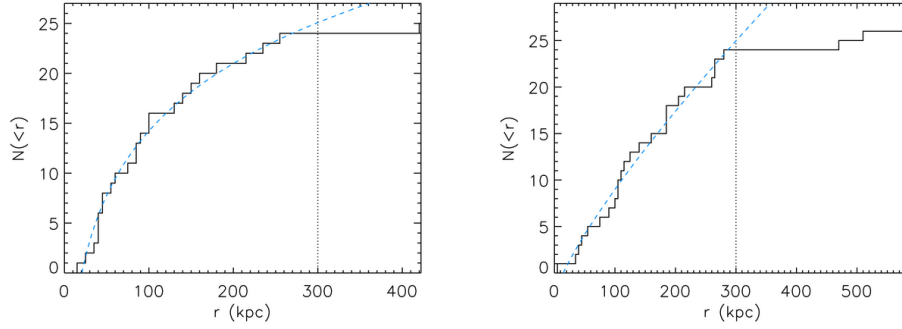


Figure 4.3: Cumulative numbers of satellite $N(<r)$ for the MW (upper) and M31 (lower). The best-fit power laws in the range $r \leq 300$ kpc are also plotted. The index of these power-law fits may be used to estimate the power-law index of the satellite density distribution $n(r)$.

tribution, which could affect the power index for the tracer number density if the directional incompleteness varies in different distances.

Finally, there are a number of possibilities for the velocity anisotropy for the satellite galaxies. Previous studies often assumed isotropy, arguing that there is no compelling evidence to the contrary. However, Diemand et al. (2007) found that the velocity anisotropy of satellites in simulations behaves like $\beta(r) \simeq 0.55(r/r_{\text{vir}})^{1/3}$ for $0.2r_{\text{vir}} \leq r \leq r_{\text{vir}}$. To estimate β for the MW and M31 satellites, we calculate the weighted mean of this distribution

$$\bar{\beta} = \frac{\int_{0.2r_{\text{vir}}}^{r_{\text{vir}}} \beta(r)n(r)r^2 dr}{\int_{0.2r_{\text{vir}}}^{r_{\text{vir}}} n(r)r^2 dr} \quad (4.32)$$

where the weighting function $n(r)$ is the satellite number density distribution. This gives $\bar{\beta} = 0.44$ for the MW and $\bar{\beta} = 0.45$ for M31. This is similar to the anisotropy of halo stars ($\beta = 0.37$) in simulations reported by Xue et al. (2008). Even though these numbers have the backing of simulations, they are somewhat surprising. Most of the MW satellites with measured proper motions are moving on polar or tangential orbits. Using the sample of the 7 MW satellites with proper motions, we can compute the radial and tangential components of the Galactocentric velocity. From these, the observed anisotropy $\beta \sim -4.5$, which favours tangential orbits. This is consistent with the earlier, though indirect, estimate of Wilkinson & Evans (1999), who found $\beta \sim -1$, again favouring tangential orbits. The origin of this discrepancy between simulations and data is not well understood. Perhaps there is considerable cosmic scatter in the anisotropy of the satellites, as it may depend on the details of the accretion history of the host galaxy. Figure 4.4 plots brings both good news and bad. The left panel shows that the mass estimates for external galaxies using the line of sight estimator of equation (4.23) are reasonably insensitive to the precise value of β . This makes sense, as for a galaxy like M31, the line of sight velocity encodes information on both the radial and tangential velocity components referred to the M31's centre. However, in the case of the MW, the situation is very different. The measured velocities provide information almost wholly on the radial component referred to the Galactic Center. In the absence of proper motions, the velocity anisotropy is largely unconstrained by the data. This is the classical mass-anisotropy degeneracy, and so – as the right panel shows – there is considerable uncertainty in the mass estimates inferred using equation (4.16).

4.3 Mass Estimates for Andromeda and the Milky Way

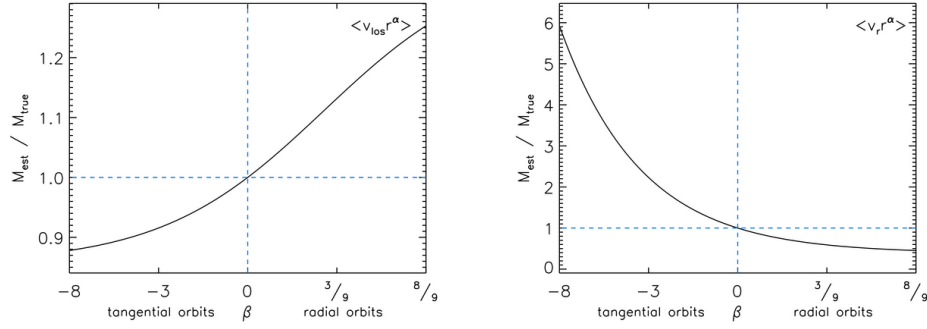


Figure 4.4: The sensitivity of the estimated mass on the anisotropy parameter β for a satellite population with $\alpha = 0.55$, $\beta = 0$ and $\gamma = 2.7$. The figure shows the mass recovered using the input values of α and γ and varying the value of β . The functional form of the curve is easy to deduce. It is a rational function of β for the upper panel, which uses the estimator of equation (4.23), and a linear function of β for the lower panel, which uses equation (4.16).

In what follows, we typically quote mass estimates for the anisotropies derived both from observations β_{data} and from simulations β_{sim} , as well as for the case of isotropy ($\beta = 0$). In the absence of consistent indications to the contrary, our preference is to assume isotropy and to give greatest credence to the mass estimates obtained with this assumption.

4.3.2 Radial Velocity Datasets

Armed with values for α , β and γ , we now set the mass estimators to work. Data for the satellites of the MW and M31 are given in Tables 4.1 and 4.2 respectively. Objects for which no line-of-sight velocity has been measured (And XVII, And XVIII, And XIX, And XX, And XXI and And XXII) are included in the tables, but excluded from the analysis.

Using equation (4.16) and recalling that the Monte Carlo simulations gave errors of $\sim 25\%$, we give estimates of the mass with 100, 200 and 300 kpc for the MW in Table 4.3. Assuming velocity isotropy, we obtain for the mass of the MW $M_{300} = 0.9 \pm 0.3 \times 10^{12} M_{\odot}$. The cursedness of the mass-anisotropy degeneracy is well illustrated by the fact that using the observationally-derived β_{data} gives $M_{300} = 3.4 \pm 0.9 \times 10^{12} M_{\odot}$, whilst using that from simulations gives $M_{300} = 0.6 \pm 0.2 \times 10^{12} M_{\odot}$. The huge spread in mass estimates is due to the fact that the line-of-sight velocities for the satellites are almost entirely providing information on the radial velocities as judged from the Galactic Centre. There is almost no information on the tangential motions in our dataset. However, there are other astrophysical reasons why masses higher than $\sim 2 \times 10^{12} M_{\odot}$ are disfavoured.

Using equation (4.23), we obtain the mass of M31 within 300 kpc as $M_{300} = 1.4 \pm 0.4 \times 10^{12} M_{\odot}$. Here, though, in sharp distinction to the case of the MW, plausible changes in the velocity anisotropy generate modest changes of the order of 10 per cent in the mass estimate, as shown in Table 4.3. Of course, this is understandable, as the line-of-sight velocity now has information on both the radial and tangential components, albeit tangled up in the projection.

Taking the masses derived using velocity isotropy ($\beta = 0$), we note that this work hints at the removal of a long-standing puzzle, namely that the kinematic data on the satellite galaxies suggested that M31 was less massive than the MW, whereas other indicators (such as the total numbers of GCs

4 Masses of the Milky Way and Andromeda Galaxies

Table 4.1: Data table for the satellites of the MW. Listed are Galactic coordinates (l , b) in degrees, Galactocentric distance r in kpc and corrected line-of-sight velocity in km s^{-1} .

Name	l (deg)	b (deg)	r (kpc)	v_{los} (km s^{-1})	Source
Bootes I	358.1	69.6	57	106.6	1,2
Bootes II	353.8	68.8	43	-115.6	3,4
Canes Venatici I	74.3	79.8	219	76.8	5,6
Canes Venatici II	113.6	82.7	150	-96.1	6,7
Carina	260.1	-22.2	102	14.3	8,9
Coma Bernices	241.9	83.6	45	82.6	6,7
Draco	86.4	34.7	92	-104.0	8,10,11
Fornax	237.3	-65.6	140	-33.6	8,12,13
Hercules	28.7	36.9	141	142.9	6,7
LMC	280.5	-32.9	49	73.8	8,14,15
Leo I	226.0	49.1	257	179.0	8,16,17
Leo II	220.2	67.2	235	26.5	8,18,19
Leo IV	265.4	56.5	154	13.9	6,7
Leo T	214.9	43.7	422	-56.0	6,20
Leo V	261.9	58.5	175	62.3	21
SMC	302.8	-44.3	60	9.0	8,22,23
Sagittarius	5.6	-14.1	16	166.3	8,24
Sculptor	287.5	-83.2	87	77.6	8,25,26
Segue 1	220.5	50.4	28	113.5	3,27
Segue 2	149.4	-38.1	41	39.7	28
Sextans	243.5	42.3	89	78.2	8,9,29
Ursa Major I	159.4	54.4	101	-8.8	3,6
Ursa Major II	152.5	37.4	36	-36.5	6,30
Ursa Minor	104.9	44.8	77	-89.8	8,10,11
Willman 1	158.6	56.8	42	33.7	2,3

Sources: 1 - Belokurov et al. (2006), 2 - Martin et al. (2007), 3 - Martin et al. (2008), 4 - Koch et al. (2009), 5 - Zucker et al. (2006), 6 - Simon & Geha (2007), 7 - Belokurov et al. (2007), 8 - Karachentsev et al. (2004), 9 - Mateo (1998), 10 - Bellazzini et al. (2002), 11 - Armandroff et al. (1995), 12 - Saviane et al. (2000), 13 - Walker et al. (2006), 14 - Freedman et al. (2001), 15 - van der Marel et al. (2002), 16 - Bellazzini et al. (2004), 17 - Koch et al. (2007), 18 - Bellazzini et al. (2005), 19 - Koch et al. (2007), 20 - Irwin et al. (2007), 21 - Belokurov et al. (2008), 22 - Cioni et al. (2000), 23 - Harris & Zaritsky (2006), 24 - Ibata et al. (1997), 25 - Kaluzny et al. (1995), 26 - Quéloz et al. (1995), 27 - Geha et al. (2009), 28 - Belokurov et al. (2009), 29 - Walker et al. (2006), 30 - Zucker et al. (2006)

or the amplitude of the gas rotation curve) suggested the reverse. In fact, with the new datasets, the ratio of the masses of M31 to the MW (~ 1.5) is close to that which would be inferred using the Tully-Fisher relationship and the assumption that the luminosity is proportional to the total mass ($250^4/220^4 \approx 1.67$). If instead the radial anisotropies derived from simulations are preferred, then the ratio is ~ 1.98 .

4.3 Mass Estimates for Andromeda and the Milky Way

Table 4.2: Data table for the satellites of M31. Listed are Galactic coordinates (l , b) in degrees, actual distance r from the centre of M31 in kpc, projected distance R from the centre of M31 in kpc and corrected line-of-sight velocity in km s^{-1} .

Name	l (deg)	b (deg)	r (kpc)	R (kpc)	v_{los} (km s^{-1})	Source
M33	133.6	-31.3	809	206	74	1,2
M32	121.1	-22.0	785	5	95	2,3
IC 10	119.0	-3.3	660	261	-29	2,3,4
NGC 205	120.7	-21.1	824	39	58	1,2
NGC 185	120.8	-14.5	616	189	106	1,2
IC 1613	129.8	-60.6	715	510	-56	2,3,5
NGC 147	119.8	-14.2	675	144	117	1,2
Pegasus	94.8	-43.6	919	473	85	1,2
Pisces	126.7	-40.9	769	268	-37	1,2
And I	121.7	-24.8	745	59	-84	1,2
And II	128.9	-29.2	652	185	83	1,2
And III	119.4	-26.3	749	75	-57	1,2
And V	126.2	-15.1	774	109	-107	1,2
And VI	106.0	-36.3	775	267	-64	1,2
And VII	109.5	-9.9	763	218	21	1,2
And IX	123.2	-19.7	765	41	94	1,6,7
And X	125.8	-18.0	702	110	130	8,9
And XI	121.7	-29.1	785	102	-140	7,10
And XII	122.0	-28.5	830	107	-268	7,10,11
And XIII	123.0	-29.9	785	115	64	7,10
And XIV	123.0	-33.2	740	161	-204	12
And XV	127.9	-24.5	770	94	-57	13,14
And XVI	124.9	-30.5	525	280	-106	13,14
And XVII	120.2	-18.5	794	45		15
And XVIII	113.9	-16.9	1355	589		16
And XIX	115.6	-27.4	933	187		16
And XX	112.9	-26.9	802	128		16
And XXI	111.9	-19.2	859	148		17
And XXII	132.6	-34.1	794	220		17

Sources: 1 - McConnachie et al. (2005), 2 - McConnachie & Irwin (2006b), 3 - Karachentsev et al. (2004), 4 - Sakai et al. (1999), 5 - Cole et al. (1999), 6 - Zucker et al. (2004), 7 - Collins et al. (2009), 8 - Zucker et al. (2007), 9 - Kalirai et al. (2009), 10 - Martin et al. (2006), 11 - Chapman et al. (2007), 12 - Majewski et al. (2007), 13 - Ibata et al. (2007), 14 - Letarte et al. (2009), 15 - Irwin et al. (2008), 16 - McConnachie et al. (2008), 17 - Martin et al. (2009)

Table 4.3: Enclosed mass within 100, 200 and 300 kpc for MW and M31. We offer three estimates: one using the anisotropy inferred from data ($\beta \sim -4.5$), one assuming isotropy ($\beta = 0$) and the third with the anisotropy derived from simulations ($\beta \sim 0.45$).

Galaxy	$M_{300} (\times 10^{11} M_{\odot})$			$M_{200} (\times 10^{11} M_{\odot})$			$M_{100} (\times 10^{11} M_{\odot})$		
	$\bar{\beta}_{data}$	isotropic	$\bar{\beta}_{sim}$	$\bar{\beta}_{data}$	isotropic	$\bar{\beta}_{sim}$	$\bar{\beta}_{data}$	isotropic	$\bar{\beta}_{sim}$
Milky Way	34.2 ± 9.3	9.2 ± 2.5	6.6 ± 1.8	21.1 ± 5.7	5.5 ± 1.6	3.8 ± 1.0	13.9 ± 4.9	3.3 ± 1.1	2.1 ± 0.7
... excl Leo I	25.2 ± 7.5	6.9 ± 1.8	5.0 ± 1.2
... excl Leo I, Her	21.1 ± 6.3	5.8 ± 1.5	4.2 ± 1.1	17.5 ± 5.3	4.6 ± 1.4	3.2 ± 0.8
MW with PMs	38.6 ± 7.0	24.1 ± 5.3	22.1 ± 5.3	28.3 ± 5.5	18.5 ± 4.2	17.0 ± 4.2	22.2 ± 5.0	13.8 ± 3.9	11.4 ± 3.1
... excl Draco	27.1 ± 4.9	14.1 ± 3.1	12.2 ± 2.7	18.1 ± 3.4	10.0 ± 2.3	8.7 ± 2.2	12.9 ± 3.1	6.9 ± 1.9	5.4 ± 1.5
... excl LMC/SMC	38.8 ± 6.8	24.6 ± 5.8	21.7 ± 4.9	28.3 ± 5.7	18.4 ± 4.3	16.3 ± 4.1	22.7 ± 5.6	13.9 ± 4.2	11.2 ± 3.4
... excl Draco, LMC/SMC	25.9 ± 5.1	12.4 ± 2.9	10.6 ± 2.5	17.0 ± 3.5	8.5 ± 2.2	7.2 ± 1.8	11.3 ± 2.9	5.4 ± 1.7	4.2 ± 1.3
M31	15.8 ± 3.3	14.1 ± 4.1	13.1 ± 3.8	15.4 ± 4.1	12.4 ± 3.8	10.6 ± 3.5	2.6 ± 1.0	2.1 ± 1.0	1.8 ± 1.0
... excl AndXII	12.2 ± 2.7	10.9 ± 3.1	10.1 ± 3.2	11.4 ± 3.2	9.2 ± 3.1	7.9 ± 2.8
... excl AndXII, AndXIV	9.6 ± 2.1	8.5 ± 2.4	8.0 ± 2.4	8.6 ± 2.6	6.9 ± 2.4	5.9 ± 2.2
M31 with PMs	15.1 ± 3.8	13.9 ± 3.5	13.1 ± 3.5

4.3 Mass Estimates for Andromeda and the Milky Way

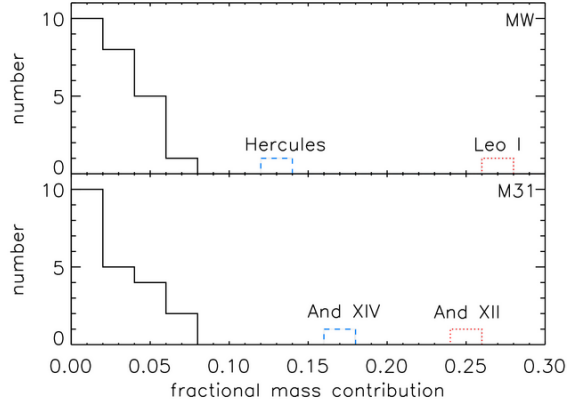


Figure 4.5: The fractional contribution each satellite makes to the mean mass estimator for the MW (top) and M31 (bottom). For both galaxies, the mass budget is dominated by two satellites. For the MW these are Leo I (red, dotted) and Hercules (blue, dashed). For M31, these are And XII (red, dotted) and And XIV (blue, dashed).

However, it may be imprudent to include all the satellites. For example, Leo I has long been known to dominate mass estimates of the MW, on account of its large distance (~ 260 kpc) and high line-of-sight velocity (see e.g. Kulessa & Lynden-Bell, 1992; Kochanek, 1996; Wilkinson & Evans, 1999). It is unclear that Leo I is actually on a bound orbit, as opposed to a hyperbolic one. Hence, many attempts at determining the mass of the MW quote estimates both including and excluding Leo I. In fact, recent photometric and spectroscopic evidence presented by Sohn et al. (2007) favours the picture in which Leo I is bound on an orbit with high eccentricity (~ 0.95) and small perigalacticon (10-15 kpc). In particular, such models give good matches to the surface density and radial velocity dispersion profiles of Leo I, and imply high mass estimates for the MW. However, Sales et al. (2007) using simulations found a population of satellite galaxies on extreme orbits ejected from haloes as a result of three-body slingshot effects, and suggested that Leo I might be an example of such an object. So, although the present evidence favours a bound orbit, a definitive verdict must await the measurement of Leo I's proper motion by the *Gaia* satellite, which should resolve the issue.

Given that there is one satellite that is known to inflate the MW's mass, it is interesting to investigate whether any of the other satellites, particularly the recent discoveries, play similar rôles. The upper panel of Figure 4.5 shows the fractional contributions each satellite makes to the MW's mass ($Cv_{\text{los}}^2 r^a / (GN)$) – it is the total of these values that we take to be the mass estimate. There are two clear outliers; the outermost satellite in this distribution is Leo I, the less extreme satellite is Hercules. Like Leo I, Hercules has a substantial radial velocity and a relatively large Galactocentric distance (~ 130 kpc). Hercules has a highly elongated, irregular and flattened structure (Belokurov et al., 2007; Coleman et al., 2007). This is consistent with tidal disruption during pericentric passages on a highly eccentric orbit ($e > 0.9$). This seems good evidence that Hercules is truly bound to the MW.

We repeat the same analysis for M31 and the results are shown in the bottom panel of Figure 4.5. Interestingly, we see that there are two outliers in the distribution, namely two of the recent discoveries, And XII and And XIV. Notice that though both objects have a substantial effect on M31's mass estimate, neither are as extreme as Leo I. It is the inclusion of these two new objects in the satellite dataset that has augmented the mass of M31, so that it is now somewhat greater than that of the MW.

4 Masses of the Milky Way and Andromeda Galaxies

But, this begs the question: should these satellites be included? And XIV was discovered by Majewski et al. (2007) in a survey of the outer M31 stellar halo. They recognized its extreme dynamical properties and suggested that it may either be falling into M31 for the first time or that M31's mass must be larger than hitherto estimated by virial arguments. In fact, And XIV's lack of gas and its elongated structure suggest that ram pressure stripping and tidal effects may have been important in its evolution. This is consistent with And XIV being a true satellite of M31 that has already suffered a pericentric passage, a conclusion that could be strengthened with deeper imaging, which might reveal the presence of tidal tails around And XIV.

And XII is a still more ambiguous object – it was discovered as a stellar overdensity by Martin et al. (2006). Spectroscopic observations were subsequently taken by Chapman et al. (2007), who conjectured that the satellite might be falling into the LG for the first time. The evidence for this is its large velocity and its likely location behind M31. However, it remains unclear whether this evolutionary track is consistent with the absence of detection of HI gas in the object. Pristine, infalling dwarfs, which have not yet experienced a pericentric passage of 50 kpc or less, should retain sizeable amounts of neutral HI gas, whereas Chapman et al. (2007) constrain the mass in HI to be less than $3 \times 10^3 M_{\odot}$.

In light of this, we provide more mass estimates, after removing possible ambiguous objects (and re-computing the parameter γ where necessary). For the MW, we exclude Leo I only and then Leo I and Hercules. For M31, we exclude And XII only and then And XII and And XIV. These mass estimates are also shown in Table 4.3. Note that, for example, the exclusion of Leo I does not change the mass estimate within 100 or 200 kpc, as Leo I is outside of this range. Similarly, And XII and And XIV lie outside of 100 kpc from the center of M31, so the mass estimates without them do not change the final column of the table.

In the case of velocity isotropy ($\beta = 0$), it requires the excision of both And XII and And XIV from the datasets for the mass estimate of M31 to become comparable to or smaller than the MW. For example, the mass of M31 with And XII and And XIV both removed is $0.85 \pm 0.24 \times 10^{12} M_{\odot}$, as compared to the mass of the MW with Leo I retained of $0.92 \pm 0.25 \times 10^{12} M_{\odot}$. However, we have argued that And XIV is most likely bound, whilst And XII is a more ambiguous case. In other words, the problem pointed to by Evans & Wilkinson (2000) – namely that the mass of M31 inferred from the kinematics of the satellites is less than the mass of the MW – has indeed been ameliorated by the discovery of more fast-moving M31 satellites.

It seems particularly intriguing that such satellites exist for both the MW and M31. Wilkinson & Evans (1999) used virialized models to estimate that the probability that, in a sample of 30 satellites, there is an object like Leo I, which changes the mass estimate by a factor of a few. They found that the probability is minute, only $\sim 0.5\%$. Prior expectation does not favour the existence of objects like Leo I or And XII, yet in fact, both big galaxies in the LG possess such satellites. The clear conclusion is that the satellites in the outer parts of these galaxies cannot all be virialized. This is a point in favour of processes such as those advocated by Sales et al. (2007) to populate such orbits.

4.3 Mass Estimates for Andromeda and the Milky Way

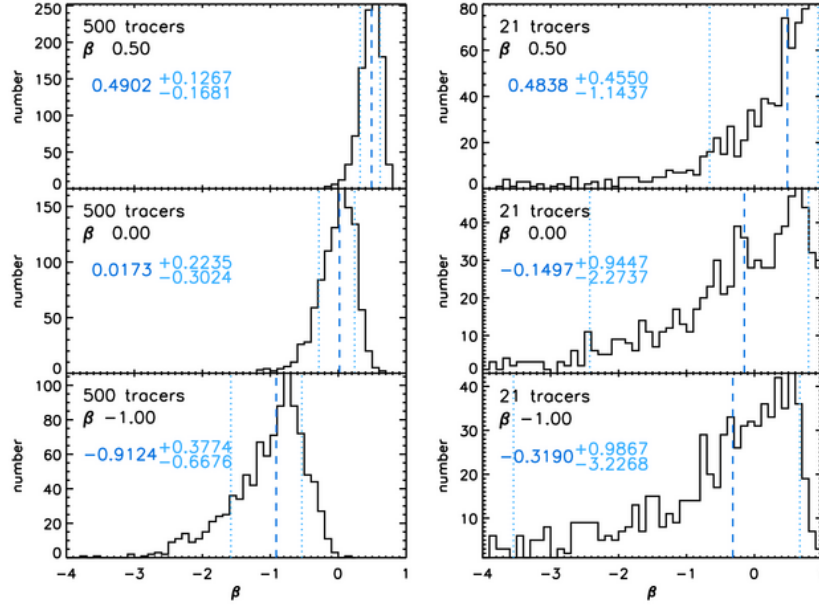


Figure 4.6: Distribution of β obtained from simultaneous mass and velocity anisotropy fitting. The median of each distribution is shown as a blue dashed line and the 68 % confidence limits as cyan dotted lines. These values are also given in blue and cyan on the plot. The left panel shows the idealised case for 500 tracers, the right panel the case tailored to our M31 data where only 21 tracers are used. The value of β used to generate the tracer population is also shown.

4.3.3 Simultaneous Solution for Mass and Anisotropy

There is one further way in which the estimators can be set to work with the line-of-sight velocities. When three dimensional positions and projected positions are simultaneously available – as for example in the case of M31’s satellites – it is possible to use the estimators based on both the $\langle v_{\text{los}}^2 r^\alpha \rangle$ and the $\langle v_{\text{los}}^2 R^\alpha \rangle$ moments to solve simultaneously for both the total mass and the anisotropy parameter. There is however no guarantee that the solution for β is in the physical range $-\infty \leq \beta \leq 1$.

The success of this procedure of course rests on the accuracy of the data. The distances of the M31 satellites are determined by the tip of the red giant branch method and have errors of ± 30 kpc (see e.g., McConnachie et al., 2005). If we use equations (4.23) and (4.26), and simultaneously solve for the unknowns, we obtain

$$M_{300} = 1.5 \pm 0.4 \times 10^{12} M_\odot, \quad \beta = -0.55_{-3.2}^{+1.1} \quad (4.33)$$

which corresponds to mild tangential anisotropy. These are surprisingly sensible answers given the distance errors.

Figure 4.6 is inferred from Monte Carlo simulations and shows the distributions of anisotropy parameters derived from simultaneous mass and anisotropy fitting for mock datasets. Also given in the panels are the median and 68 per cent confidence limits for the anisotropy parameter, in the case of 21 satellite galaxies (comparable to the present dataset for M31) and the case of 500 satellites. Although with 21 tracers, the errors on the anisotropy parameter are substantial, matters improve significantly with larger numbers of tracers. A dataset of 500 halo satellites (dwarf galaxies, GCs and

4 Masses of the Milky Way and Andromeda Galaxies

Table 4.4: Table of proper motion data for the satellites of the MW and M31. Listed are equatorial proper motions in mas century⁻¹.

Name	$\mu_\alpha \cos \delta$ (mas/century)	μ_δ (mas/century)	Source
Carina	22 ± 9	15 ± 9	1
Draco	60 ± 40	110 ± 30	2
Fornax	48 ± 5	-36 ± 4	3
LMC/SMC	198 ± 5	25 ± 5	4
Sculptor	9 ± 13	2 ± 13	5
Sextans	-26 ± 41	10 ± 44	6
Ursa Minor	-50 ± 17	22 ± 16	7
M33	2.1 ± 0.7	2.5 ± 1.2	8
IC10	-0.2 ± 0.8	2.0 ± 0.8	9
M31	2.1 ± 1.1	-1.0 ± 0.9	10

Sources: 1 - Piatek et al. (2003), 2 - Scholz & Irwin (1994), 3 - Piatek et al. (2007), 4 - Piatek et al. (2008), 5 - Piatek et al. (2006), 6 - Walker et al. (2008), 7 - Piatek et al. (2005), 8 - Brunthaler et al. (.pp 211–+), 9 - Brunthaler et al. (2007), 10 - van der Marel & Guhathakurta (2008), though unlike the other proper motions, this not a measurement but inferred from indirect evidence.

planetary nebulae) is perhaps not unreasonable in the near future. This raises the possibility that the method of simultaneous fitting may prove more compelling in the future. In fact, given 500 tracers, it is reasonable to use the estimators based on both the $\langle v_{\text{los}}^2 r^a \rangle$ and the $\langle v_{\text{los}}^2 R^a \rangle$ moments to fit simultaneously at each distance, thus giving the run of anisotropy parameter and mass with radius.

4.3.4 Radial and Proper Motion Datasets

Thus far, we have used only the line-of-sight velocities to make mass estimates. In this section, we add in the proper motions of satellites, where available. Thus, for the MW, we combine results from equation (4.16) for satellites without proper motions and from equation (4.24) for those with proper motions, weighting each estimate by the reciprocal of the standard deviation to give the final answer.

Proper motions, albeit with large error bars, have been measured for a total of 9 of the MW satellite galaxies. It seems prudent to exclude Sagittarius, as it is in the process of merging with the MW, and to treat the interacting Magellanic Clouds as a single system. This leaves us with a set of 7 satellites with proper motion data, summarized in Table 4.4. In most cases, errors on proper motions are large and, where multiple studies exist, the measurements are sometimes in disagreement. The proper motions inferred by ground-based methods are in reasonable agreement with those derived from the *Hubble Space Telescope* (*HST*) in the cases of Fornax (Piatek et al., 2007; Walker et al., 2008), Carina (Piatek et al., 2003; Walker et al., 2008) and the Magellanic Clouds (Piatek et al., 2008; Costa et al., 2009). But, for Ursa Minor (Scholz & Irwin, 1994; Piatek et al., 2005) and for Sculptor (Schweitzer et al., 1995; Piatek et al., 2006; Walker et al., 2008), agreement between different investigators is not good, and we have preferred to use the estimates derived from *HST* data. Nonetheless, it is important to include the proper motion data, especially for mass estimates of the MW. We use these proper motions along with distance and line-of-sight velocity data to calculate full space velocities for these

4.3 Mass Estimates for Andromeda and the Milky Way

satellites, as described in Piatek et al. (2002). The method is also outlined in Appendix A.

In addition, there are two satellites of M31 with measured proper motions, namely M33 and IC 10. This astonishing feat has exploited the *Very Long Baseline Array* to measure the positions of water masers relative to background quasars at multiple epochs (Brunthaler et al., 2005, 2007). Unfortunately, the technique cannot be extended to M31 itself, as it does not contain any water masers, and so its proper motion is much less securely known. However, van der Marel & Guhathakurta (2008) reviewed the evidence from a number of sources – including kinematics of the M31 satellites, the motions of the satellites at the edge of the LG, and the constraints imposed by the tidal distortion of M33’s disk – to provide a best estimate. These data are also listed in Table 4.4.

The MW satellites are so remote that their line-of-sight velocities in the Galactic rest frame are almost identical to their radial velocities, as judged from the Galactic Centre. The proper motion data provide genuinely new information on the tangential motions and this is the only way to break the mass-anisotropy degeneracy. The same argument does not hold with equal force for M31, as the line-of-sight velocities incorporate contributions from both the radial and tangential components as reckoned from the centre of M31. Nonetheless, it is good practice to use all the data available, even though the proper motions of M33 and IC 10 with respect to the M31 reference frame must be inferred using an estimate of M31’s proper motion (rather than a measurement).

For the satellites without proper motions, we use the form of the estimator given in equation (4.16) or equation (4.23) for the MW and M31 respectively; for those with proper motions, we use equation (4.24). We combine results from the two estimators, weighting each estimate by the reciprocal of the standard deviation to give the final answer. To infer the standard deviation, we perform Monte Carlo simulations. So, for the case of the MW, we generate mock datasets of 25 satellites, for which only 7 have proper motions. The errors on radial velocities are dwarfed by the uncertainty caused by the small number statistics and so are neglected. But, the errors on the proper motions are not negligible and they are incorporated into the simulations by adding a value selected at random from the range $[-0.5 \mu, 0.5 \mu]$, where μ is the proper motion. The flat distribution has been chosen as systematic errors are as important as random Gaussian error in the determination of proper motions. The standard deviations of the fractional mass distribution the satellites with and without proper motions are separately computed, as illustrated in the panels of Figure 4.7. We linearly combine the mass estimates, weighting with the reciprocal of the standard deviation, to give the final values reported in Table 4.3.

Given that the MW satellites with measured proper motions are moving on polar orbits, it is no surprise that the mass estimate of the MW has now increased. Adopting the value of β we estimate from the data, we find $M_{300} = 3.9 \pm 0.7 \times 10^{12} M_{\odot}$ for the MW and $M_{300} = 1.5 \pm 0.4 \times 10^{12} M_{\odot}$ for M31. Assuming isotropy, we find $M_{300} = 2.4 \pm 0.5 \times 10^{12} M_{\odot}$ for the MW and $M_{300} = 1.4 \pm 0.4 \times 10^{12} M_{\odot}$ for M31. Notice however, the mass estimate for M31 has barely changed from the value inferred from the full radial velocity dataset.

Again, we calculate the contribution that each satellite makes to the mass estimate to investigate whether any are dominating the final answer. First, this procedure guards against the possibility of a completely rogue proper motion measurement. Second, there are some suggestions that the Magellanic Clouds may not be bound, or even if bound may be on only its second passage and so may not be part of the relaxed distribution of satellite galaxies (Besla et al., 2007). So, it is helpful to check that

4 Masses of the Milky Way and Andromeda Galaxies

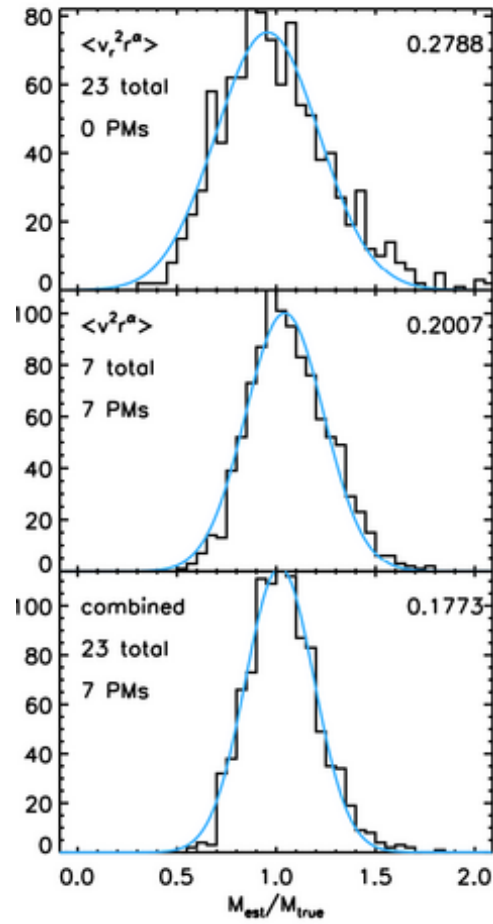


Figure 4.7: Distribution of mass estimates as a fraction of true mass for Monte Carlo simulations using (top) 23 satellites with radial velocities, (middle) 7 satellites with proper motions and (bottom) 23 satellites, 7 of which have proper motions. The standard deviation of the best fitting Gaussian is shown in the top-right hand corner of each panel. [These plots assume $\beta = -4.51$, as estimated from the data].

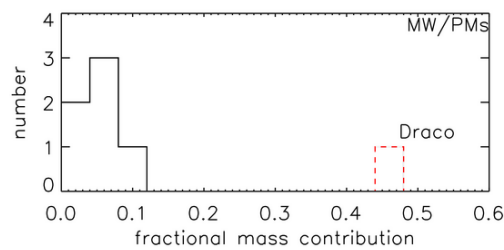


Figure 4.8: The fractional contribution each satellite with proper motions makes to the mean mass estimate for the MW. Notice the extreme effect of Draco's proper motion.

our results are not unduly sensitive to its inclusion. As Figure 4.8 shows, we find that Draco is a clear outlier and nearly doubles the MW mass estimate. If we remove Draco from the sample, we instead recover a mass $M_{300} = 2.7 \pm 0.5 \times 10^{12} M_{\odot}$ (assuming β_{data}) or $M_{300} = 1.4 \pm 0.3 \times 10^{12} M_{\odot}$ (assuming isotropy). It is particularly concerning that the proper motion of Draco has such a substantial effect, because – as judged from the size of the error bars in Table 4.4 – it is one of the noisier measurements. By contrast, the exclusion of the Magellanic Clouds has only a minor effect, as is evident from the results listed in Table 4.3.

We have covered a number of possibilities, so it is probably useful for us to give our best estimates. On balance, we think the case for including at least And XIV among the satellite sample for Andromeda is strong. Whilst And XII is a more ambiguous case, the lack of any HI gas suggests to us that it should also be included. Among the satellites of the MW, we favour including Leo I based on the work of Sohn et al. (2007), whilst we are inclined to discard the proper motion of Draco reported in Scholz & Irwin (1994) until corroborated. Until the discrepancy between the velocity anisotropies reported in simulations and in data is explained, we prefer to use the data as our guide.

So, our best estimate for the mass of the MW within 300 kpc is

$$M_{300} \sim 2.7 \pm 0.5 \times 10^{12} M_{\odot} \quad (4.34)$$

whilst for M31, it is

$$M_{300} \sim 1.5 \pm 0.4 \times 10^{12} M_{\odot}. \quad (4.35)$$

These estimates are obtained using the combined radial velocity and proper motion datasets. The error bars only incorporate the statistical uncertainty. As we have emphasised, there are much greater uncertainties induced by selection of satellite members and velocity anisotropy. In particular, when these uncertainties are considered, it is not possible to decide which of the MW or M31 is more massive based on satellite kinematic data alone.

4.4 Discussion

It is instructive to compare our results with a number of recent estimates of the masses of the LG and its component galaxies. Xue et al. (2008) extracted a sample of ~ 2400 blue horizontal branch stars from the SDSS. These are all resident in the inner halo within 60 kpc of the Galactic centre. This has the advantage that the BHBs are surely virialized, but the disadvantage that no inference can be made about the mass exterior to 60 kpc. Hence, any estimate as to the total mass is driven wholly by prior assumptions rather than the data. In fact, Xue et al. (2008) assumed an NFW halo with a canonical concentration holds, and then estimated the virial mass of the MW's dark matter halo as $M = 1.0_{-0.2}^{+0.3} \times 10^{12} M_{\odot}$, using Jeans modelling with an anisotropy parameter inferred from numerical simulations. This is lower than our preferred value, but in good agreement with our comparable calculations using line-of-sight velocity datasets alone.

A somewhat similar calculation for M31 has been reported by Seigar et al. (2008). The mass of the

4 Masses of the Milky Way and Andromeda Galaxies

baryonic material is estimated using a Spitzer 3.6m image of the galaxy, together with a mass-to-light ratio gradient based on the galaxy's $B - R$ colour. This is combined with an adiabatically-contracted NFW halo profile to reproduce the observed HI rotation curve data. They find a total virial mass of M31's dark halo as $8.2 \pm 0.2 \times 10^{11} M_{\odot}$. This is lower than all our estimates, with the exception of those based on samples excluding both And XII and And XIV.

Although these calculations are interesting, it is worth remarking that the final masses are not wholly controlled by the data. We know that, from Newton's theorem, any mass distribution outside the limiting radius of our data has no observational effect in a spherical or elliptical system. To estimate the virial mass from data confined to the inner parts (such as BHBs or the optical disk) requires an understanding of the structure of the pristine dark halo initially, as well as how it responds to the formation of the luminous baryonic components. It is this that controls the final answer.

Li & White (2008) used the Millennium Simulation to extract mock analogues of the LG and calibrate the bias and error distribution of the Timing Argument estimators (see e.g., Kahn & Woltjer, 1959; Raychaudhury & Lynden-Bell, 1989). From this, they obtain a total mass of the two large galaxies in the LG of $5.3 \times 10^{12} M_{\odot}$ with an interquartile range of $[3.8 \times 10^{12}, 6.8 \times 10^{12}] M_{\odot}$ and a 95 % confidence lower limit of $1.8 \times 10^{12} M_{\odot}$. Importantly, Li & White (2008) showed that the mass estimate from the timing argument is both unbiased and reasonably robust. This is a considerable advance, as there have long been worries that the gross simplification of two-body dynamics implicit in the original formulation of the Timing Argument may undermine its conclusions.

It therefore seems reasonable to assume that the combined mass of the MW and M31 is at least $3.8 \times 10^{12} M_{\odot}$, and perhaps more like $5.3 \times 10^{12} M_{\odot}$. The low estimates of the MW and M31 masses of Xue et al. (2008) and Seigar et al. (2008) are not compatible with this, and barely compatible with 95 % lower limit of Li & White (2008). Using our preferred values in equations (4.34) and (4.35), the combined mass in the MW and M31 galaxies is $3.0 \pm 0.6 \times 10^{12} M_{\odot}$. This is still lower than the $3.8 \times 10^{12} M_{\odot}$ of Li & White, but much more modestly so.

Li & White (2008) also estimated a virial mass for the MW of $2.4 \times 10^{12} M_{\odot}$ with a range of $[1.1 \times 10^{12}, 3.1 \times 10^{12}] M_{\odot}$, based on timing arguments for Leo I. This is in reasonable accord with our best estimate. In fact, it is in better agreement if we include the problematic proper motion of Draco, but this then makes the MW more massive than M31.

4.5 Summary

We have derived a set of robust tracer mass estimators, and discussed the conditions under which they converge. Given the positions and velocities of a set of tracers – such as GCs, dwarf galaxies or stars – the estimators compute the enclosed mass within the outermost datapoints. The accuracy of the estimator has been quantified with Monte Carlo simulations. The estimators are applicable to a wide range of problems in contemporary astrophysics, including measuring the masses of elliptical galaxies, the haloes of spiral galaxies and galaxy clusters from tracer populations. They are considerably simpler to use than distribution-function-based methods (see e.g. Little & Tremaine, 1987; Kulessa & Lynden-Bell, 1992; Wilkinson & Evans, 1999), and involve no more calculation than taking weighted averages of combinations of the positional and kinematical data. They should find

widespread applications.

The mass estimators are applied to the satellite populations of the MW and M31 to find the masses of both galaxies within 300 kpc. These estimates are the first to make use of the recent burst of satellite discoveries around both galaxies. Both satellite populations have nearly doubled in size since previous estimates were made. We summarise our results by answering the questions; What are (1) the minimum, (2) the maximum and (3) the most likely masses of the MW and M31 galaxies?

(1) The mass of the MW within 300 kpc could be as low as $0.4 \pm 0.1 \times 10^{12} M_{\odot}$. This would imply that Leo I is gravitationally unbound, contrary to the recent evidence provided by Sohn et al. (2007). Leo I would then be either an interloper or an object being ejected from the MW by an encounter. It would also require that the proper motion of Draco (Scholz & Irwin, 1994) is incorrect, which is not inconceivable given the difficulty of the measurements. It implies that the satellite galaxies are moving on radial orbits and so the velocity anisotropy is radial.

The mass of M31 within 300 kpc could plausibly be as low as $0.8 \pm 0.2 \times 10^{12} M_{\odot}$. This would be the case if both And XII and And XIV are not gravitationally bound, which is possible if mechanisms such as those proposed by Sales et al. (2007) are ubiquitous. It would also require that the proper motion data on M33 and IC10 or – perhaps more likely – the indirectly-inferred proper motion of M31 is in error. Again, such a low estimate for the mass occurs only if the satellites are moving predominantly radially.

Although it is interesting to ask how low the masses of the MW and M31 could be, it does produce a mystery in the context of the Timing Argument, which typically yields larger combined masses. It is possible that some of the mass of the LG is unassociated with the large galaxies. Although not the conventional picture, this is probably not ruled out and there have been suggestions that $\sim 10^{12} M_{\odot}$ may be present in the LG in the form of baryons in the warm-hot intergalactic medium (Nicastro et al., 2003). There are few constraints on the possible existence of dark matter smeared out through the LG, and unassociated with the large galaxies. However, the clustering of the dwarf galaxies around the MW and M31 does suggest that the gravity of the dark matter is centered on the prominent galaxies.

(2) The largest mass estimate we obtained for the MW is $3.9 \pm 0.7 \times 10^{12} M_{\odot}$. This extreme value is driven by the assumption of tangential anisotropy for the satellites, so that the measured line-of-sight velocities also imply substantial tangential motions as well. The estimate assumes all the satellites including Leo I to be bound, and the anomalously-high proper motion measurement of Draco to be valid.

Note that the present data allow considerably more scope to increase the mass of the MW than M31. Our largest mass estimate for M31 is a more modest $1.6 \pm 0.4 \times 10^{12} M_{\odot}$, which occurs when we analyse the whole sample incorporating And XII and And XIV and assume tangentially-anisotropic velocity distributions.

The current consensus is that the two galaxies are of a roughly similar mass, with M31 probably the slightly more massive of the two. This though is inferred from indirect properties, such as the numbers of GCs, which correlates with total mass albeit with scatter, or the amplitude of the inner gas rotation curve. The stellar halo of M31 is certainly more massive than that of the MW, although this may not be a good guide to the dark halo. Of course, it could be that the current consensus is wrong, and that the MW halo is more massive than that of Andromeda. There is some evidence in

4 Masses of the Milky Way and Andromeda Galaxies

favour of this – for example, the typical sizes of the M31 dSphs are large than those of the MW, which is explicable if the MW halo is denser. However, it does not seem reasonable to postulate that the mass of the MW is substantially larger than that of M31. Hence, the very large estimate of $3.9 \pm 0.7 \times 10^{12} M_{\odot}$ is really a manifestation of the degeneracy in the problem of mass estimation with only primarily radial velocity data.

(3) Our preferred estimates come from accepting Leo I, And XII and And XIV as bound satellites, whilst discarding the Draco proper motion as inaccurate. This gives an estimate for the mass of the MW within 300 kpc as $2.7 \pm 0.5 \times 10^{12} M_{\odot}$ and for M31 as $1.5 \pm 0.4 \times 10^{12} M_{\odot}$, assuming the anisotropy implied by the data ($\beta \approx -4.5$). The error bars are just the statistical uncertainty and do not incorporate the uncertainty in anisotropy or sample membership. In view of the uncertainties present, it is not possible to decide which of the MW or M31 is the more massive based on the kinematic data.

These values for the masses are attractive for a number of reasons. First, the mass ratio between the MW and M31 is of order unity, which accords with a number of other lines of evidence. Second, the values allow most of the dark matter in the LG implied by the Timing Argument to be clustered around the two most luminous galaxies. Third, they are within the range found for cosmologically motivated models of the MW and M31 (Li & White, 2008).

We prefer to assume the anisotropy implied by the (admittedly scanty) data on the proper motions of the satellites. However, for completeness, we quickly sketch the effects of dropping this assumption. If the velocity distribution is isotropic, or even radially anisotropic as suggested by the simulations, then the mass of the MW becomes $1.4 \pm 0.3 \times 10^{12} M_{\odot}$ or $1.2 \pm 0.3 \times 10^{12} M_{\odot}$ respectively. Similarly for M31, the values are $1.4 \pm 0.4 \times 10^{12} M_{\odot}$ (isotropy) or $1.3 \pm 0.4 \times 10^{12} M_{\odot}$ (radially anisotropic).

The greatest sources of uncertainty on the masses remain the role of possibly anomalous satellites like Leo I and the velocity anisotropy of the satellite populations. There is reason to be optimistic, as the *Gaia* satellite will provide proper motion data on all the dwarf galaxies that surround the MW and M31, as well as many hundreds of thousands of halo stars. The analysis that we have carried out here indicates that proper motions are important if we wish to increase the accuracy of our estimates, as well as understand the dynamical nature of objects like Leo I. While we are not yet able to exploit the proper motions, *Gaia* will allow us to do so.

5

Application of the Timing Argument to host-satellite systems

In Section 1.4, I discussed the importance of dSph galaxies to our understanding of structure formation. They are the smallest dark matter halos known to exist and they are some of the most dark-matter-dominated objects in the universe. Given that structure forms hierarchically, they will also have been some of the first objects to form and are, in essence, the building blocks of structure. Thus they are a vital component in our understanding of the nature of dark matter and are the best place for different dark matter theories to be tested.

Many of the dSphs in the LG are in the process of being tidally stripped by their host (the Sgr dSph and its well-known Sgr tidal stream is an extreme example, but we also see evidence of tidal distortion in other MW dSphs), which can somewhat distort the conclusions we are able to draw about their properties. It would be very useful to have an “unspoiled” dSph to study; Andromeda XII (And XII) and Andromeda XIV (And XIV) appear to be such dSphs.

And XII was one of three satellites of M31 discovered in CFHT data by Martin et al. (2006) as an overdensity of RGB stars. They were unable to constrain the distance to And XII with any accuracy, nevertheless, their estimate of 740-955 kpc put the dwarf comfortably inside the virial radius of M31. Assuming the distance of And XII to be the same as that of M31, they were able to estimate the size and brightness of the object, finding And XII to be smaller and fainter than any of the previously-known M31 dSphs.

Chapman et al. (2007) followed up on this study with spectroscopic observations, from which they were able to obtain an improved heliocentric distance estimate of 830 ± 50 kpc and to derive a heliocentric line-of-sight velocity of -556 km s^{-1} . They also calculated a series of model orbits for And XII and concluded that it is likely that And XII was formed outside of the virial radius of the LG. Further, the high velocity and large separation from the centre of M31 imply that And XII follows a highly eccentric orbit - as would be expected for objects that are accreted late and have only recently become bound. Thus, they suggest that And XII is on its first infall into the LG.

Collins et al. (2009) re-analysed the data from Chapman et al. (2007) and their distance and ve-

5 Application of the Timing Argument to host-satellite systems

locity results were consistent with the previous analysis. They then extended the analysis to estimate further photometric and spectroscopic properties. Using photometric data, they found an absolute magnitude the same as that estimated by Martin et al. (2006), thus confirming the faint nature of the object. Fitting an exponential model, they estimate a half-light radius twice that estimated by Martin et al. (2006), bringing the size of And XII into line with other satellites. Using spectroscopic data, they resolve a velocity dispersion of $2.2^{+4.3}_{-2.2} \text{ km s}^{-1}$, which is lower than would be expected for a dSph. They were also able to obtain a total mass estimate of $1.2^{+3.3}_{-1.2} \times 10^6 M_{\odot}$, lower than the $10^7 M_{\odot}$ mass threshold predicted for brighter dSphs.

And XIV was discovered in KPNO photometric survey of the outer halo of M31 (Majewski et al., 2007). They were only able to place loose constraints upon the distance of 630 – 850 kpc, however, with follow-up spectroscopic data they were able to derive a rather large heliocentric line-of-sight velocity of $-481.1 \pm 1.2 \text{ km s}^{-1}$. They dubbed the dwarf a “dynamical rogue” that “distinguishes itself from other LG galaxies by its extreme dynamics”. Based on M31 mass models, they concluded that, even at its projected radius, And XIV was at the M31 escape velocity, which could, in turn, imply that And XIV is on its first infall into the LG.

And XIV was recently analysed in more detail by Kalirai et al. (2010). They found a distance of $871 \pm 87 \text{ kpc}$ and a line-of-sight velocity in excellent agreement with the Majewski et al. (2007) estimate, confirming the extraordinary nature of this dwarf’s dynamics.

Chapter 4, published as Watkins et al. (2010), estimated the mass of M31 using a tracer mass estimator applied to the M31 satellite population. They found that And XII was the dominant contributor to the mass estimate, due to its higher-than-expected velocity, given its radius; And XIV was also found to make a significant contribution to the mass estimate (though less than that made by And XII). Thus, once again, highlighting these objects as unusual compared with the majority of the M31 satellites.

Clearly, these are very interesting systems, worthy of further study. If, indeed, And XII and And XIV were formed outside of the LG and are now only now on their first infall, then they will have spent most of their lives in isolation. They may be able to aid our understanding of the structure and formation of dSphs without the effects of strong gravitational interactions biasing their properties.

It would be beneficial to have independent verification of the conclusion that And XII and And XIV are on their first infall; one way to proceed is to apply the Timing Argument (TA) to the M31-And XII system and to the M31-And XIV system. The TA has been traditionally used to estimate the mass of the LG by analysing the relative motions of the MW and M31 (see e.g. van der Marel & Guhathakurta, 2008) and, more recently, it has been applied to certain of the MW satellites in order to estimate the MW mass (Li & White, 2008; Kallivayalil et al., 2009). In all of these previous cases, the MW forms one half of the pair under consideration; never before has the TA been applied to two external galaxies, as we do here. Given that And XII and And XIV are believed to be on their first infall, however, they are prime candidates for an analysis of this nature; we can use them to constrain the mass of M31-satellite system (which is, of course, dominated by the mass of M31) and, at the same time, derive some properties of their common orbit. In analysing two systems, we hope to probe these systems in more detail and also to confirm the efficacy of the TA method as applied to external galaxies.

The chapter is organised as follows: I outline the TA in Section 5.1 and describe the data that we use in Section 5.2, Section 5.3 derives orbital parameters for the M31-And XII system and we conclude

in Section 5.6.

5.1 Timing Argument

The principle behind the TA is as follows: we consider two galaxies that are nearby and moving towards each other at the present time. At the time of the Big Bang, they were close together and began to move apart with the Hubble expansion. At high redshift, their mutual gravitational attraction would have caused them to decouple from the Hubble flow and their orbit can then be described using Newtonian dynamics. Given their present separation and velocities and the time for which they have been interacting, we can estimate the properties of their orbit.

Kahn & Woltjer (1959) were the first to apply the TA to infer that there must be a significant amount of intergalactic mass for the LG to be dynamically stable. Since then, the TA has been frequently applied to the LG assuming both radial orbits (see e.g. Gott & Thuan, 1978; Lynden-Bell & Frenk, 1981; Mishra, 1985; Raychaudhury & Lynden-Bell, 1989; Lynden-Bell, 1999) and elliptical orbits (see e.g. Einasto & Lynden-Bell, 1982; Kochanek, 1996; van der Marel & Guhathakurta, 2008) and to binary galaxies in a set of N-body simulations (Kroeker & Carlberg, 1991) in order to test the accuracy of TA masses. More recently, Li & White (2008) used the galaxy pairs from the Millennium simulation to statistically study TA mass estimates, they also applied their results to the LG and to the MW-Leo I system in order to obtain a mass estimate for the MW; also Kallivayalil et al. (2009) have applied the TA to the MW-LMC system in order to estimate the mass of the MW.

It should be noted that in previous works, the MW has been one member of the galaxy pair being analysed, so the radial and tangential velocities are (relatively) easy to obtain. Here, we are applying the method to two external galaxies and so the radial and tangential velocities we derive are dependent on the velocity anisotropy we assume; this issue is discussed further in Section 5.2.

It is worth pausing here to consider the validity of the approximations the TA makes and whether or not it is worth proceeding in the face of such assumptions. The TA treats the two galaxies as point masses, which is clearly a gross oversimplification of the true nature of any system - indeed, both And XII and And XIV lie inside the virial radius of M31 - and the galaxies themselves will have evolved and, in the case of the M31, accreted a significant amount of mass since the Big Bang. Li & White (2008) recently studied LG-like pairs in the Millennium Simulation, thus accounting for the relative extents and evolution history of the galaxies, to show that the TA gives an almost unbiased estimate of the combined mass of two large galaxies, like the MW and M31. They then extended the analysis to a MW-like galaxy with a smaller satellite and showed that the TA is equally effective for determining the mass of the host. So it seems, that despite the rather generous assumptions, the TA is surprisingly effective.

Of course, the MW will also exert a force on each of the satellites as well, and if that force is a significant fraction of the force they experience due to M31 then the assumption of an isolated system will be suspect. However, given that the force exerted by the MW on And XII (And XIV) is only 3% (8%) of that exerted by M31, we are confident that the assumption of an isolated system is reasonable.

To apply the TA to a given dataset, we solve the following set of equations, where η is the eccentric anomaly, e is the eccentricity, a is the semi-major axis length and M is the total mass of the

5 Application of the Timing Argument to host-satellite systems

system:

$$r = a(1 - e \cos \eta) \quad (5.1)$$

$$t = \left(\frac{a^3}{GM} \right)^{\frac{1}{2}} (\eta - e \sin \eta) \quad (5.2)$$

$$v_r = \left(\frac{GM}{a} \right)^{\frac{1}{2}} \frac{e \sin \eta}{1 - e \cos \eta} \quad (5.3)$$

$$v_t = \left(\frac{GM}{a} \right)^{\frac{1}{2}} \frac{\sqrt{1 - e^2}}{1 - e \cos \eta} \quad (5.4)$$

We have four equations and four unknowns, however, unless we are in the special case where $e = 1$, these equations are not easily solved. To proceed, we first use equations (5.1) and (5.3) to eliminate a and M in equation (5.2):

$$\frac{v_r t}{r} = \frac{e \sin \eta (\eta - e \sin \eta)}{(1 - e \cos \eta)^2} \quad (5.5)$$

and then from the ratio of v_r and v_t , we can obtain an expression for e :

$$\frac{v_r}{v_t} = \frac{e \sin \eta}{\sqrt{1 - e^2}} \quad (5.6)$$

so

$$e = \pm \frac{v_r}{\left(v_r^2 + v_t^2 \sin^2 \eta \right)^{\frac{1}{2}}} \quad (5.7)$$

The sign ambiguity is resolved by ensuring that $e \geq 0$; thus, the positive (negative) sign is taken for receding (approaching) orbits. Substituting for equation (5.7) in equation (5.5) then gives:

$$t = \pm \frac{r \sin \eta \left(\eta \left(v_r^2 + v_t^2 \sin^2 \eta \right)^{\frac{1}{2}} \mp v_r \sin \eta \right)}{\left(\left(v_r^2 + v_t^2 \sin^2 \eta \right)^{\frac{1}{2}} \mp v_r \cos \eta \right)^2} \quad (5.8)$$

From this we may solve for η , then we can calculate e via equation (5.7) and a and M via

$$a = \frac{r}{1 - e \cos \eta} \quad \text{and} \quad M = \frac{a^3 (\eta - e \cos \eta)^2}{G t^2} \quad (5.9)$$

and from a , e and M , we can also calculate the apocenter, pericenter and period of the orbit,

$$r_{\text{apo}} = a(1 + e), \quad r_{\text{peri}} = a(1 - e) \quad \text{and} \quad T = 2\pi \sqrt{\frac{a^3}{GM}} \quad (5.10)$$

5.2 The Data

In order to apply the TA to the M31 - And XII system and the M31 - And XIV system, we need to know r , t , v_r and v_t for each system at the present time.

Time t is straightforward to obtain: for each host-satellite pair, the TA assumes that their orbits are bound, and that their mutual gravitational attraction caused them to decouple from the Hubble flow at high redshift, thus $t = 0$ corresponds to the Big Bang, and the current time t is the age of the universe, which has been constrained using WMAP data to be $t_u = 13.73^{+0.16}_{-0.15}$ Gyr (Spergel et al., 2007). This value will be the same for both systems.

The separations r are also easily calculated using simple trigonometry. The centre of M31 lies at $(00^{\text{h}}42^{\text{m}}44^{\text{s}}.3, +41^{\circ}16'09'')$ and heliocentric distance $d_{\text{M31}} = 785 \pm 25$ kpc (McConnachie et al., 2005). And XII lies at $(00^{\text{h}}47^{\text{m}}27^{\text{s}}, +34^{\circ}22'29'')$ (Martin et al., 2006) and at a heliocentric distance of $d_{\text{XII}} = 833 \pm 44$ kpc (Nicolas Martin, private communication). And XIV lies at $(00^{\text{h}}51^{\text{m}}35^{\text{s}}.0, +29^{\circ}41'49'')$ (Majewski et al., 2007) and at a heliocentric distance of $d_{\text{XIV}} = 871 \pm 87$ kpc (Kalirai et al., 2010). Thus, the M31 - And XII separation is $r_{\text{XII}} = 109$ kpc and the M31 - And XIV separation is $r_{\text{XIV}} = 189$ kpc.

The velocities v_r and v_t are more complicated to determine as we are not able to measure either value directly. Given the heliocentric line-of-sight velocity v_{los} and the heliocentric equatorial transverse velocity (v_α, v_δ) of an object, its Galactic transverse velocity (v_ℓ, v_b) and, hence, its velocity in the Galactocentric Rest Frame (GRF) may be calculated following the prescription explained in Appendix A.

The observed line-of-sight velocity of M31 has been well studied and is well constrained; for the present work, we use $v_{\text{los,M31}} = -301 \text{ km s}^{-1}$ (McConnachie & Irwin, 2006b). However, the same is not true for M31's transverse velocity, despite repeated attempts to constrain it; we adopt proper motion estimates from van der Marel & Guhathakurta (2008) who performed a statistical analysis of the orbital velocities of M31 satellites to find $(v_\alpha, v_\delta) = (78, -38) \text{ km s}^{-1}$. (It should be noted that these values have contributions from the solar peculiar motion and the motion of the LSR, which can be removed using equations (A.9) and (A.10).)

The observed line-of-sight velocity of And XII is $v_{\text{los,XII}} = -577.0^{+2.3}_{-2.7} \text{ km s}^{-1}$ (Collins et al., 2009) and for And XIV is $v_{\text{los,XIV}} = -481.0 \pm 1.2 \text{ km s}^{-1}$ (Kalirai et al., 2010). In the absence of any proper motion measurements, we assume that the motion of each dwarf is purely along its line-of-sight (i.e. $v_\ell = 0$ and $v_b = 0$). As well as the intrinsic motion of the dwarf, this velocity has contributions from the solar peculiar motion, the motion of the LSR and the relative motion of M31 and the MW, all of which must be removed using the methods described in Appendix A. The corrected line-of-sight velocity is then $v_{\text{cor}} = \mathbf{v}_{\text{MRF,dwarf}} \cdot \lambda_{\text{dwarf}}$, where $\mathbf{v}_{\text{MRF,dwarf}}$ is the M31-centric velocity of the dSph and λ_{dwarf} is the unit line-of-sight vector to the dwarf.

These corrected line-of-sight velocities of And XII ($v_{\text{cor}} = -264 \text{ km s}^{-1}$) and And XIV ($v_{\text{cor}} = -196 \text{ km s}^{-1}$) have contributions from both the radial velocities v_r and the tangential velocities v_t

$$v_{\text{cor}} = v_r \cos \alpha + v_t \sin \alpha \cos \zeta \quad (5.11)$$

for α the angle between the line joining the centre of M31 and the centre of the dSph and the line-of-sight to the dSph and ζ the angle between the tangential velocity vector and the projection of the

5 Application of the Timing Argument to host-satellite systems

line-of-sight vector in the plane perpendicular to the radial velocity vector. α may be calculated via

$$\cos \alpha = \frac{d_{\text{dwarf}}^2 + r_{\text{dwarf}}^2 - d_{\text{M31}}^2}{2d_{\text{dwarf}}r_{\text{dwarf}}} \quad (5.12)$$

$$\sin \alpha = \frac{d_{\text{M31}} \sin \phi}{r_{\text{dwarf}}} \quad (5.13)$$

where ϕ is the angular separation of the dSph and M31 and can be found via,

$$\cos \phi = \cos b_{\text{dwarf}} \cos b_{\text{M31}} \cos(\ell_{\text{dwarf}} - \ell_{\text{M31}}) + \sin b_{\text{dwarf}} \sin b_{\text{M31}} \quad (5.14)$$

Now we suppose that v_r and v_t are related by a velocity ratio τ ,

$$\tau = \pm \frac{v_t}{v_r}. \quad (5.15)$$

Hence,

$$v_t = \frac{\tau v_{\text{cor}}}{\pm \cos \alpha + \tau \sin \alpha \cos \xi} \quad (5.16)$$

and

$$v_r = \pm \frac{v_t}{\tau} \quad (5.17)$$

These equations allow for two solutions for v_r and v_t , depending on the sign adopted; the solution that should be taken will depend on the sign and size of the other parameters. We recall that we require v_t to be positive. If the two solutions obtained are both negative then there is no v_t and v_r that produce the observed GRF line-of-sight velocity for the given parameters τ , α and ξ . If only one solution is positive then the sign that gave that value should be used. When both solutions are positive, we use the smaller value since, in general, we will seek to set a lower constraint on the mass of the M31-satellite system, and hence require the solution that gives the lower energy. It can be shown analytically that the positive sign should be taken when v_{cor} and $\cos \alpha$ have the same sign and the negative sign should be taken when v_{cor} and $\cos \alpha$ have opposite signs. There are no solutions when v_{cor} and $\cos \xi$ have opposite signs and $|\cos \alpha| < |\tau \sin \alpha \cos \xi|$.

It should also be noted that this analysis assumes that we know both τ and ξ , which we do not; however, if we adopt values of τ and ξ , we can estimate v_r and v_t and hence, calculate a , e , η and M .

5.3 M31 mass and orbit parameters

5.3.1 M31 - And XII orbit

In the absence of velocity anisotropy information and the angle of inclination of the orbit with respect to the plane of the sky, we cannot estimate the mass of the M31-And XII system; the best we can do is work out the mass estimates for a grid of values of τ and ξ and obtain a lower limit on the mass.

For each pair of τ and ξ values, equation (5.8) is solved for η via an iterative process in which:

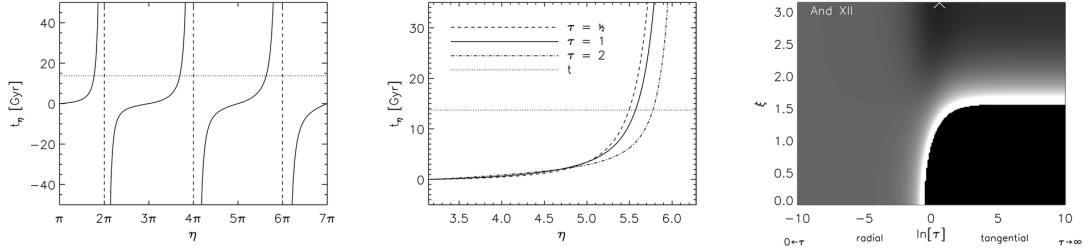


Figure 5.1: Left panel: The solid line shows the behaviour of t as a function of η for $\tau = 1$ and $\xi = \pi$. The dotted line shows the value of t we have adopted for this study. Solutions to equation (5.8) occur when the solid and dotted lines intersect; it is clear that multiple solutions exist. Middle panel: Same as the left panel, for the region $[\pi, 2\pi]$. The solid (dashed, dot-dashed) line shows the solution for $\tau = 1$ (0.5, 2) for $\xi = \pi$. The corresponding graphs for higher ranges of η are very similar so are not shown. Right panel: A contour plot showing how the mass estimate changes with $\ln(\tau)$ and ξ , where we restricted solutions for η to the region $[\pi, 2\pi]$. Black represents the low masses and white the highest masses; the solid black section in the bottom right corresponds to the region where no solution may be found. The mass estimates reaches a minimum when $\tau \sim 1.8$ and $\xi = \pi$, highlighted by the white cross. Again, the graphs for higher ranges of η are very similar so are not shown.

1. we calculate t_η for a uniform distribution of η in $[\eta_{\min}, \eta_{\max}]$,
2. we find the value of η for which $\Delta_t = |t - t_\eta|$ is minimised,
3. we make this value of η the centre of our grid, reduce the grid spacing by a factor of 10 and then rerun the grid calculation.

In this way we are able to progressively refine the grid we are searching over. The method stops when $\Delta_t < 10^{-5}$ or when the maximum resolution of the computer has been achieved whichever occurs first. The final value of η obtained from the grid search is then used to calculate e , a and M as described in Section 5.2.

The left panel of Figure 5.1 shows the behaviour of t as a function of η for $\tau = 1$ and $\xi = \pi$; it is clear that multiple solutions exist. We start investigating the first by searching for a solution $\eta \in [\pi, 2\pi]$, thus assuming that And XII is on its first infall into M31. Solutions are shown in the middle panel of Figure 5.1 for three values of τ (the solid, dashed and dot-dashed lines) and $\xi = \pi$ with the adopted value of t shown as a dotted line.

The velocity ratio τ is highly asymmetric about 1 ($0 \leq \tau \leq \infty$), so instead of generating τ uniformly in $[0, \infty]$, we use $\ln(\tau)$ as a proxy for τ and generate $\ln(\tau)$ uniformly in $[-10, 10]$. Mass estimates are plotted as a function of τ and ξ in the right-hand panel of Figure 5.1. There is a clear minimum in the distribution for $\tau = 1.8$ and $\xi = \pi$, thus we are able to place a lower constraint on the mass of the system of $M = 1.1 \times 10^{12} M_\odot$. The corresponding orbit has semi-major-axis length $a = 291$ kpc, eccentricity $e = 0.73$ and eccentric anomaly $\eta = 5.7$. From these parameters we can deduce the apocenter $r_{\text{apo}} = 503$ kpc, the pericenter $r_{\text{peri}} = 79$ kpc and the period $P = 14.1$ Gyr.

We repeat the analysis for next 9 solutions admitted by equation (5.8) and investigate the change of orbital properties with η - the results are shown in Figure 5.2. The left panel shows the apocenters, pericenters and semi-major-axis lengths of the orbits; the apocenters asymptote to the current position of the satellite and the pericenters asymptote to 0, thus, it seems that there is never an unphysical

5 Application of the Timing Argument to host-satellite systems

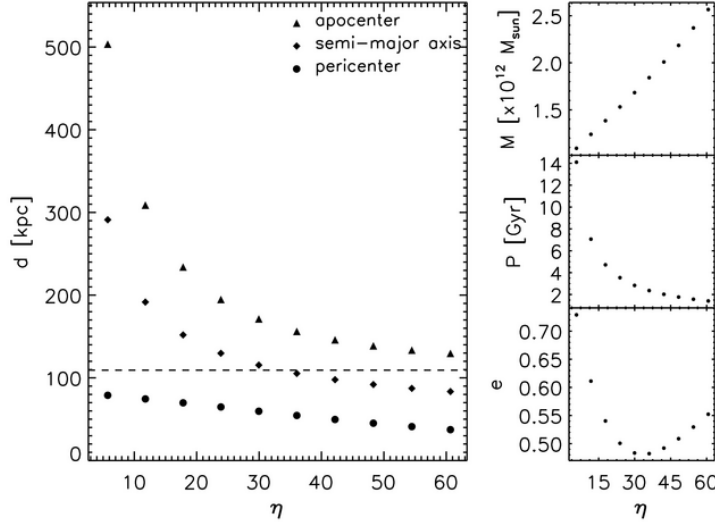


Figure 5.2: Multiple solutions are admitted for η (as shown in the left panel of Figure 5.1) and here we show the results for the first 10 solutions. Left panel: apocenter (triangles), semi-major axis (diamonds) and pericenter (circles) as a function of η . The dotted line shows the current position of the satellite. It appears that the apocenter asymptotes to the current position of the satellite while the pericenter asymptotes to 0. Top right: Minimum mass estimate as a function of η . Middle right: orbital period P as a function of η . Bottom right: eccentricity as a function of η .

solution to the equations which would help us to further constrain the allowed orbits.

The top-right panel shows that the mass estimate increases with η . We now ask whether it is possible to place any constraints on the number of orbits And XII has completed by comparing our results with previous mass estimates. Recently, Watkins et al. (2010) used a tracer mass estimator applied to the satellite population of M31 to estimate the mass within 300 kpc, finding $M_{300} = 1.5 \pm 0.4 \times 10^{12} M_{\odot}$. We take the upper limit of this mass estimate to be the maximum mass allowed by the TA estimate. Adopting this maximum mass, we conclude that And XII can have completed at most six orbits of M31. Adopting the Watkins et al. (2010) mass estimate as the best mass estimate, the 4-orbit scenario gives the best match to the mass estimate. The corresponding orbit has mass $M = 1.5 \times 10^{12} M_{\odot}$, semi-major-axis length $a = 130$ kpc, eccentricity $e = 0.50$ and, hence, apocenter $r_{\text{apo}} = 195$ kpc, pericenter $r_{\text{peri}} = 65$ kpc and period $P = 3.5$ Gyr.

Satellites are predicted to undergo periods of star formation as they pass through pericenter; using this orbit information we have deduced for And XII, we can calculate the times of all previous pericenter passages and thus predict when star formation is likely to have occurred in the past. The solution we have adopted puts And XII on its fourth orbit of M31, so we predict three bursts of star formation in its history; the first 10.2 Gyr ago, the second 6.6 Gyr ago and the third 3.1 Gyr ago. Unfortunately, the data that exists for And XII is not yet good enough for its actual SFH to be determined, so we are unable to check our predictions against reality.

So using the TA, we are able to place a lower limit on the mass of the system; combining the TA with previous mass estimates, we are able to make estimates of the number of orbits a system has completed and even predict the star formation history (SFH) of the satellite.

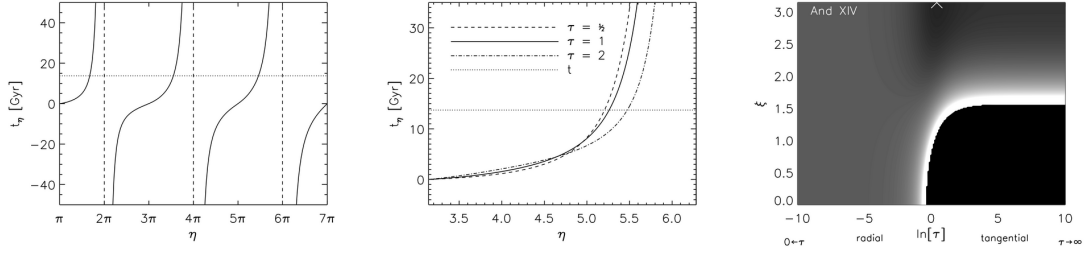


Figure 5.3: The same as Figure 5.1 for And XIV with $\xi = \pi$. Again, the middle and right panels show solutions for $\eta \in [\pi, 2\pi]$.

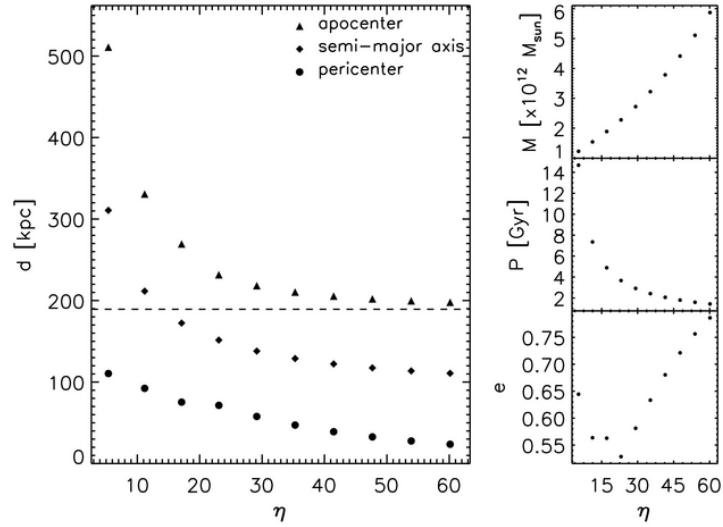


Figure 5.4: Same as Figure 5.2 for And XIV.

5.3.2 M31 - And XIV orbit

The analysis was repeated using And XIV; with the results shown in Figure 5.3. The left panel once again shows the behaviour of t with η with the middle showing the same in the range $[\pi, 2\pi]$ and the right panel showing the mass estimated for different values of assumed τ in the same range; the overall shapes of all three graphs are very similar to those found for And XII. Multiple solutions are again admitted and we investigate the first ten, as before.

For $\eta \in [\pi, 2\pi]$, the minimum mass is found to be $M = 1.2 \times 10^{12} M_{\odot}$ when $\tau = 1.5$ and $\xi = \pi$, with orbital properties $a = 311$ kpc, $e = 0.64$ and $\eta = 5.4$, with corresponding apocenter $r_{\text{apo}} = 511$ kpc, pericenter $r_{\text{peri}} = 110$ kpc and period $P = 14.7$ Gyr.

For higher orbits (see Figure 5.4), we see the same trends as for And XII, the apocenters asymptote to the current position of And XIV and the pericenters asymptote to 0; the mass again increases steadily and using the Watkins et al. (2010) M31 mass estimates, we conclude that And XIV has completed at most three orbits, and it is most likely on its second orbit. The corresponding orbit in this case has mass $M = 1.5 \times 10^{12} M_{\odot}$, semi-major-axis length $a = 212$ kpc, eccentricity $e = 0.56$ and, hence, apocenter $r_{\text{apo}} = 331$ kpc, pericenter $r_{\text{peri}} = 92$ kpc and period $P = 7.4$ Gyr.

Once again, we can also predict the SFH of And XIV by calculating the times of pericenter pas-

5 Application of the Timing Argument to host-satellite systems

sage. As And XIV is only on its second orbit of M31, it will only have passed through pericenter once, so we predict a burst of star formation 6.4 Gyr ago. Again, the quality of the And XIV is not yet good enough for us to compare this estimate with observations.

The overall trends observed in this analysis are very similar to the trends observed in the M31-And XII analysis; and further, the minimum mass estimates are in good agreement, which increases confidence in the modifications to the TA we have presented here.

5.4 Modelling

The notion of “extreme” satellites suggests that And XII and And XIV are peculiar and often have properties that are different from those of the general M31 satellite population. Indeed, it is their large line-of-sight velocities that first drew our attention to these objects and prompted this study. Now we consider whether these two satellites really are on extreme orbits, or whether they are simply ordinary satellites on ordinary orbits and we just happen to viewing them at a special point in their orbit or from a special viewing position.

How many such satellites do we expect? Wilkinson & Evans (1999) looked at the case of Leo I with smooth distribution functions and concluded that such extreme satellites are very rare. So if And XII and And XIV are representatives of a smooth, dynamically relaxed population then they should be very unusual.

To go beyond smooth distribution functions, we run a series of Monte Carlo simulations; we exploit the TA to generate a suite of orbits and then “observe” their present-day positions and line-of-sight velocities with respect to a series of simulated observers.

To simulate orbits, we require a , e and M . As we are concerned with the M31 satellite population, we take mass $M = M_{\text{M31}} = 1.5 \times 10^{12} M_{\odot}$. Semi-major axes a and eccentricities e are drawn from the distributions

$$f(a)da \propto a^{\mu} da \quad g(e)de \propto e^{\nu} de \quad (5.18)$$

respectively, where $f(a)da$ represents the probability of finding an object with semi-major axis in $[a, a + da]$ and $g(e)de$ the probability of the eccentricity lying in $[e, e + de]$. Here we choose $\mu = -3$ and $\nu = 1$, though we explore the effect of changing these shortly.

We integrate each orbit forwards from zero for one complete period P and then extract the present-day host-satellite separations and radial and tangential velocities as being those values when the time $t = t_{\text{u}} \bmod P$. We also calculate the position vectors of the satellite in a Cartesian coordinate system centred on the host with the x and y axes in the plane of the satellite orbit and the z axis normal to the plane. The x axis is taken to point along the semi-major axis. Thus the position vector of any point in the orbit is given by

$$\mathbf{r}_{\text{hs}} = \left(a (\cos \eta - e), a \sqrt{1 - e^2} \sin \eta, 0 \right) \quad (5.19)$$

and the velocity of the satellite with respect to the host at any point is then

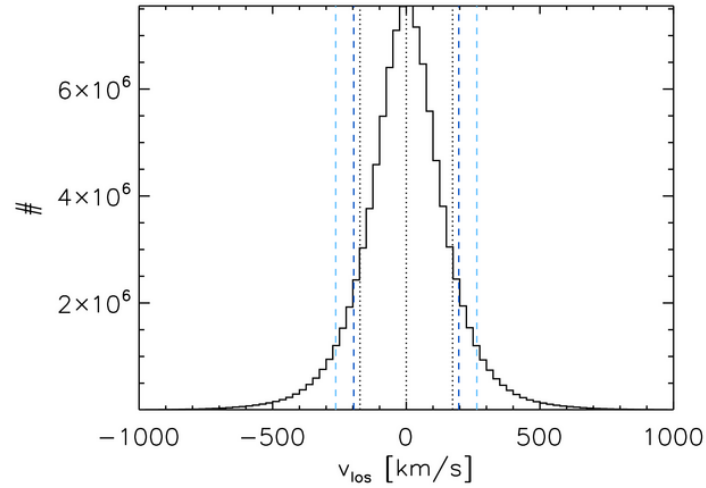


Figure 5.5: Distribution of line-of-sight velocities from the Monte Carlo simulations using 10000 orbits and 10000 viewing positions.

$$\mathbf{v}_{\text{hs}} = \left(-\sqrt{\frac{GM}{a}} \frac{\sin \eta}{1 - e \cos \eta}, \sqrt{\frac{GM}{a}} \frac{\sqrt{1 - e^2} \cos \eta}{1 - e \cos \eta}, 0 \right). \quad (5.20)$$

Again, we are only interested in the position and velocity vectors at the present time.

Observer positions are generated as position vectors relative to the host, in the same Cartesian coordinates by setting $d = 785$ kpc (the M31-MW separation distance) and generating ϕ uniformly in $[0, 2\pi]$ and θ in $[-\frac{\pi}{2}, \frac{\pi}{2}]$ by selecting $\sin \theta$ uniformly in $[-1, 1]$. The position vector of the observer with respect to the host is then

$$\mathbf{r}_{\text{ho}} = (d \cos \phi \cos \theta, d \sin \phi \cos \theta, d \sin \theta). \quad (5.21)$$

and the position vector of the satellite with respect to the observer is given by

$$\mathbf{r}_{\text{os}} = \mathbf{r}_{\text{hs}} - \mathbf{r}_{\text{ho}}. \quad (5.22)$$

The unit line-of-sight vector from the viewer to the satellite is then $\lambda = \mathbf{r}_{\text{os}}/|\mathbf{r}_{\text{os}}|$ and the line-of-sight velocity is

$$v_{\text{los}} = \mathbf{v}_{\text{hs}} \cdot \lambda. \quad (5.23)$$

10^4 orbits and 10^4 viewing positions were generated and then the line-of-sight velocity at the present day was calculated for each orbit from every viewing angle. The distribution of line-of-sight velocities obtained is shown in Figure 5.5. The mean and 1σ values are marked by the dotted lines and we find that $\sim 24\%$ of the cases resulted in line-of-sight velocities that lay more than 1σ from the mean. We also found that $\sim 20\%$ of the cases had line-of-sight velocities whose magnitudes were greater than that of And XIV and $\sim 11\%$ has line-of-sight velocities with magnitudes greater than that of And XII. By this measure, it is reasonably likely to find extreme satellites.

5 Application of the Timing Argument to host-satellite systems

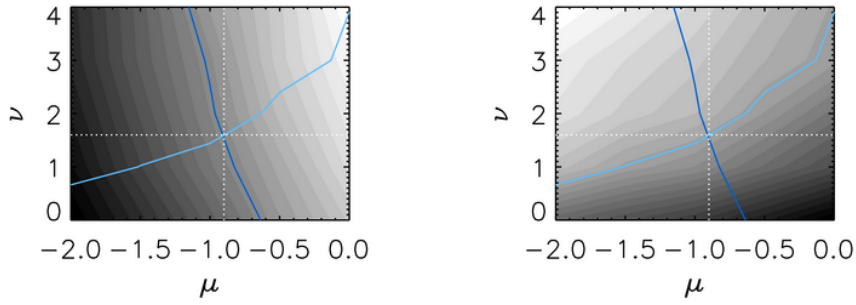


Figure 5.6: Contour plots to show how the mean separation (left) and ratio of satellites with velocities like And XII or higher and satellites with velocities like And XIV or higher (right) vary as we change the power-law indices of the distributions of a and e . The dark blue line shows the contour on which the mean separation is 189 kpc and the light blue line shows the contour on which the ratio of And XII-like to And XIV-like satellites is 0.5. The white dotted lines show where the two highlighted contours cross, and we adopted these values for our simulations.

In reality, we have two objects with velocities like And XIV or higher (And XII and And XIV) and only one object with the velocity of And XII or higher (And XII itself), so we predict these percentages to be $\sim 9\%$ and $\sim 4.5\%$ respectively. The ratios of the two percentages are consistent with the simulations, however the values from the simulations are higher, implying that we should expect more And XII-like and And XIV-like satellites than we currently observe. However, the sample of satellites is incomplete; it is entirely possible that more of these “extreme” satellites will be discovered.

We must also consider that the distributions described by equation (5.18) could also be in error. The M31 satellite population has a mean separation distance from the centre of M31 of 189 kpc (this value is 181 kpc if we restrict our attention to only those satellites with line-of-sight velocities). By contrast, our distributions for a and e give satellites with a mean separation of only 108 kpc. In general, increasing indices μ and ν gives percentages and a mean separation more consistent with the M31 population.

Figure 5.6 shows contour plots to show how the mean separation (left) and ratio of satellites with velocities like And XII or higher and satellites with velocities like And XIV or higher (right) vary as we change the power law indices of the distributions of a and e (μ and ν respectively). The dark blue line shows the contour on which the mean separation is 189 kpc and the light blue line shows the contour on which the ratio of And XII-like to And XIV-like satellites is 0.5. We see that these two highlighted contours cross when $\mu \sim -0.9$ and $\nu \sim 1.6$ (shown by the white dotted lines) so we put these distributions into our simulations, and use the same numbers in what follows. It is not possible with the forms of the distribution functions we have chosen, to match simultaneously the mean separation, the percentage of satellites with velocities greater than And XII and the percentage of satellites with velocities greater than And XIV. These distributions for a and e predict that $\sim 22\%$ of satellites have line-of-sight velocities outside of 1σ , nearly 12% have velocities more extreme than And XIV and nearly 6% have velocities more extreme than And XII, and they give a mean separation of 192 kpc.

This analysis is all very well if we assume that satellites fall into host halos on orbits that are independent to those followed by all other satellites, however we do not believe this to be the case.

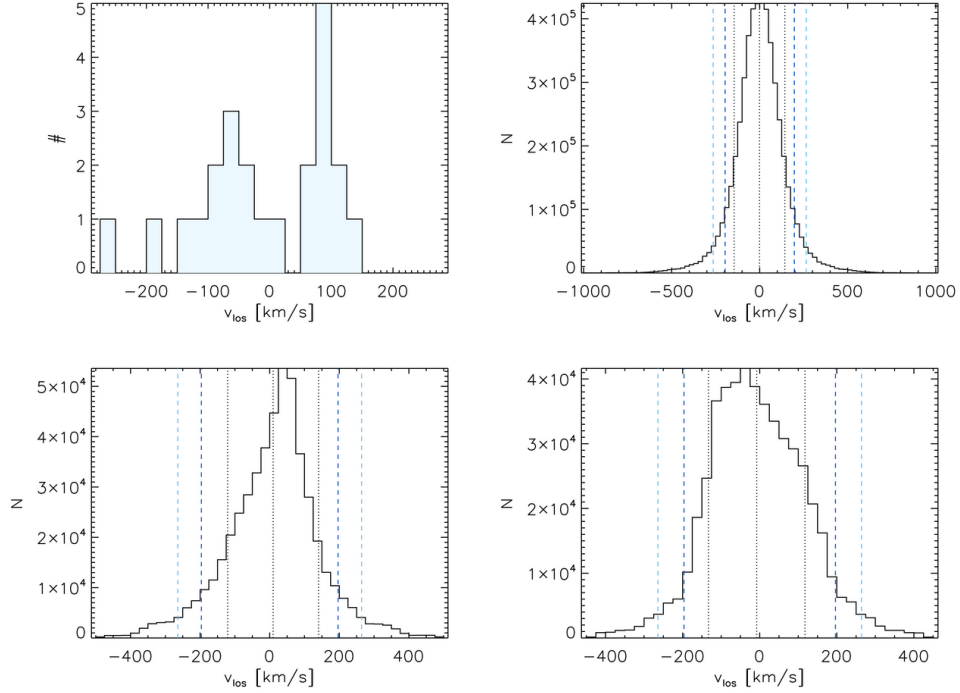


Figure 5.7: Top left: The actual M31 satellite population line-of-sight velocity distribution. Top right and lower panels: The line-of-sight velocity distributions from Monte Carlo simulations where 10 satellites are put on to each of N orbits with different infall times - in order to approximate group infall along a filament - and then “observed” from each of 10^4 viewing positions. In the top-right panel $N = 50$ and the resulting distribution is very similar to the previous non-filamentary distribution. In the two lower panels $N = 5$ and here the distributions of line-of-sight velocities are very much dependent on the initial 5 orbits as they are so few.

Instead it is believed that satellites fall in along filaments and are accreted in groups. In order to better model this situation, we repeat the same analysis as described above, but allow 10 satellites to populate each orbit, each with different infall times.

Satellites are believed to have been accreted early, so we restrict the infall times t_{in} to lie between 0 - 3 Gyr and choose a distribution function

$$f(t)dt \propto (3-t)dt \quad (5.24)$$

that favours the earlier times within that range. Then the satellite’s position and velocity at the present time will be those given by the simulated orbit at time $t_{\text{u}} - t_{\text{in}}$.

We start by generating 50 orbits and put 10 satellites on each, with their infall times picked separately for each group. We then “observe” all of the satellites from each of 10^4 viewing positions. The resulting line-of-sight velocity distribution, shown in the left panel of Figure 5.7, is very similar to that obtained from the previous analysis, by virtue of the large number of orbits we have generated. We find that $\sim 35\%$ of satellite lie outside of 1σ , $\sim 5\%$ are predicted to have velocities more extreme than And XII, $\sim 11\%$ are predicted to have velocities outside of And XIV and the mean separation of the satellites from the host centre is 198 kpc.

However, when we pick only 5 orbits, each populated by 10 satellites - a case which is more

5 Application of the Timing Argument to host-satellite systems

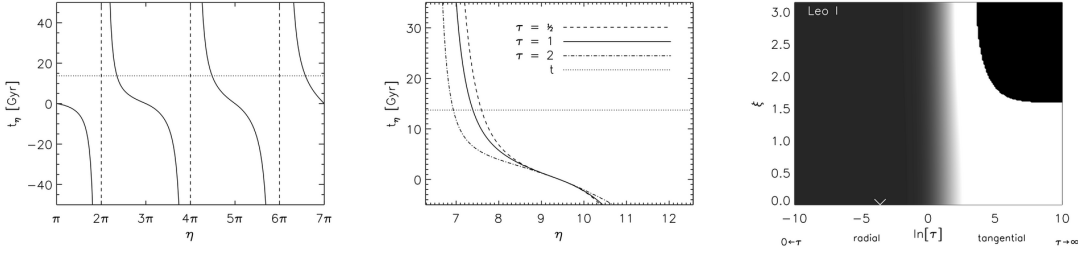


Figure 5.8: The same as Figure 5.1 for Leo I with $\xi = 0$. Now, the middle and right panels show solutions for $\eta \in [2\pi, 4\pi]$.

representative of real satellite populations - then the results are more interesting. The line-of-sight distributions from two separate simulations are shown in the two middle panels of Figure 5.7. Firstly, the line-of-sight velocity distribution is dependent on the 5 orbits generated in the simulation, as would be expected for such a low number of orbits. However, one common feature, regardless of the particular orbits generated, is that the resulting distribution is not smooth and now appears to be very much a superposition of a number of Gaussians instead of one large Gaussian, as we might expect. We also note that the mean and peak of the distributions are also offset from zero. This is a more realistic prediction of what we can expect to observe and seems broadly consistent with the actual distribution of M31 satellite line-of-sight velocities shown in the right-hand panel of Figure 5.7.

5.5 The Milky Way

5.5.1 MW - Leo I orbit

We also apply the TA to the MW - Leo I system. The system has been analysed with the TA before (Li & White, 2008), however, they did not allow for a tangential velocity component or an eccentricity in their equations.

The left panel of Figure 5.8 shows the solution to equation (5.8) for Leo I for $\tau = 1$ and $\xi = 0$; the overall shape of the graph is very similar to those for And XII and And XIV with the one major difference that this graph is inverted. This is a result of the fact that Leo I is moving away from the MW, unlike And XII and And XIV, which are both moving towards M31. This means that Leo I must have passed through its pericenter and is now making its way back out to its apocenter. A consequence of this is that there is no solution for $\eta \in [\pi, 2\pi]$, however, as for the other cases we have studied, there are multiple solutions for $\eta > 2\pi$.

The middle panel of Figure 5.8 shows how the shape of this graph changes with τ in the range $2\pi < \eta < 4\pi$ and the right panel shows how the mass estimate changes with τ and ξ in the same η range.

The minimum mass is found to be $M = 1.6 \times 10^{12} M_{\odot}$ when $\tau = 0.03$ and $\xi = 0$, with orbital properties $a = 314$ kpc, $e = 1.0$ and $\eta = 7.7$, with corresponding apocenter $r_{\text{apo}} = 627$ kpc, pericenter $r_{\text{peri}} = 0$ kpc and period $P = 12.9$ Gyr. With such a very low value of τ and an eccentricity of $e = 1$, this is essentially a purely radial orbit; this is the assumption made by Li & White (2008).

Again, we can analyse the first few orbits and attempt to constrain the number of orbits Leo I

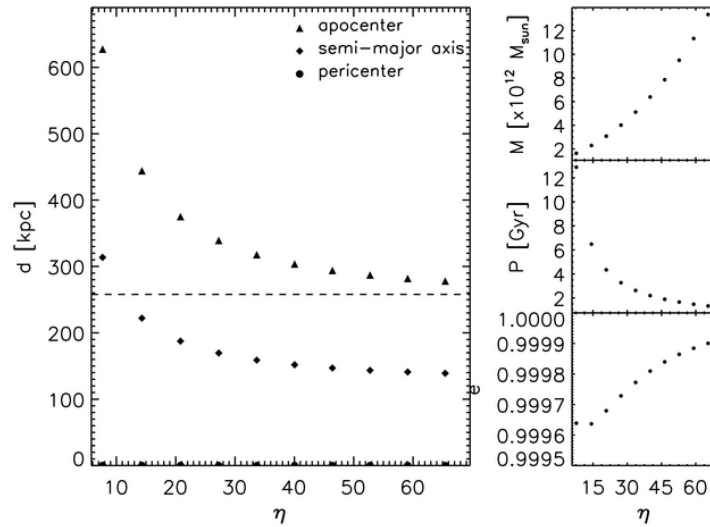


Figure 5.9: Same as Figure 5.2 for Leo I.

must have completed using previous mass estimates for the MW. Watkins et al. (2010) recently estimated the mass of the MW to be $2.7 \pm 0.5 \times 10^{12} M_{\odot}$. The upper limit of this mass range, admits only the first three solutions we have presented here; with the second solution giving the best match to the Watkins et al. (2010) mass estimate. As discussed above, Leo I is moving away from the centre of the MW and, as such, has completed at least one orbit already. Thus, the admitted solutions correspond to scenarios where Leo I is on its second, third or fourth orbit, and the best match to the Watkins et al. (2010) estimate puts Leo I on its third orbit. In this case, the orbit has mass $M = 3.1 \times 10^{12} M_{\odot}$, semi-major-axis length $a = 188$ kpc, eccentricity $e = 1.000$ and, hence, apocenter $r_{\text{apo}} = 375$ kpc, pericenter $r_{\text{peri}} = 0$ kpc and period $P = 4.3402$ Gyr. We note that this is not a very good match to the MW mass estimate, which could be the fault of either the assumptions we have made in performing the timing argument or uncertainties in the mass estimate that we were trying to match. Again, this is a perfectly radial orbit.

5.6 Discussion

In this Chapter, I have applied the TA to the M31 - And XII and M31 - And XIV systems in order to derive the properties of their orbits. We find that multiple physically realistic solutions can be found; for an object moving towards the centre of M31 (as is the case with both And XII and And XIV) the first solution assumes that the satellite is on its first orbit of M31, the second solution corresponds to the case where the satellite is on its second orbit, and so on. Where an object is moving away from the centre of M31, the first solution implies the object has completed one full orbit and is already on its second, the second solution suggests the third orbit, etc.

As both of the galaxies we have studied are external to the MW and we only have heliocentric radial velocity information for the satellites, we are unable to constrain the M31-centric radial and tangential velocities, we can only estimate them by assuming a ratio between v_r and v_t and by assuming an angle of inclination of the orbit to the plane of the sky. Thus we are not able to exactly

5 Application of the Timing Argument to host-satellite systems

constrain the particular orbit of the system, instead we find a family of solutions, with the parameters dependent upon the number of orbits we assume the satellite has completed, the ratio of the radial and tangential velocities and the inclination angle.

The best conclusion we can draw from this analysis regarding the mass of the system (which is dominated by the mass of M31) is that of a lower mass limit. The lowest mass estimate is achieved when we assume that the satellite is on its first orbit of M31; the velocity ratio for which the mass is minimised is purely a function of the geometry of the system and, as such, its particular value is uninteresting. From the analysis of the M31 - And XII system, we find a minimum mass of $M = 1.1 \times 10^{12} M_{\odot}$ and from the M31 - And XIV system, we find a minimum mass of $M = 1.2 \times 10^{12} M_{\odot}$.

Mass estimates for M31 are numerous in the literature, having been obtained via a number of different methods. Evans & Wilkinson (2000) and Evans et al. (2000) carried out dynamical modelling using distances and radial velocities to the then-known M31 satellites to estimate the mass of the extended halo of M31, finding $M = 1.23_{-0.6}^{+1.8} \times 10^{12} M_{\odot}$ and $M = (7 - 10) \times 10^{11} M_{\odot}$ (depending on the details of the modelling) respectively. More recent estimates have been presented by Klypin et al. (2002), who used constraints from Λ CDM modelling to estimate a virial mass for M31 of $M_{\text{vir}} = 1.6 \times 10^{12} M_{\odot}$ (where $r_{\text{vir}} = 300$ kpc), and Watkins et al. (2010), who used a tracer mass estimator applied to the satellite population of M31 to estimate the mass within 300 kpc, finding $M_{300} = 1.5 \pm 0.4 \times 10^{12} M_{\odot}$.

Our lower limits are certainly consistent with these previous mass estimates, and they show remarkable agreement with each other, increasing confidence in this method, despite the assumptions that we have been forced to make in the process.

These lower mass limits, however, do not give us any particular insight into the nature of the orbits of And XII and And XIV. In order to do this, we combined our TA results with previous mass estimates in order to place constraints on the number of orbits each satellite has potentially and most-likely completed. We adopted the Watkins et al. (2010) mass estimate of M31 ($M_{300} = 1.5 \pm 0.4 \times 10^{12} M_{\odot}$) to conclude that And XII can have completed at most six orbits of M31, with a 4-orbit scenario giving the best match to the mass estimate. Similarly, And XIV can have completed only 3 orbits of M31, with the 2-orbit scenario being the best match. With these most-likely orbits we calculate the times of previous pericenter passages, which are believed to correspond to bursts of star formation; however the data that exists for the satellites at present is not good enough to be able to calculate SFHs so our predictions can not be compared with reality.

We then asked the question of whether And XII and And XIV really are satellites on different orbits to the general M31 population, or if they are indistinguishable from the rest, only viewed from a special direction that serves to give them anomalously high line-of-sight velocities and artificially inflate their significance. We ran Monte Carlo simulations in which we applied our TA methods to generated orbits. A set of orbits were created with varying values of semi-major axis a and eccentricity e with the the mass M fixed as the mass of M31, and a set of viewing positions were created evenly over the surface of a sphere with a radius equal to the MW-M31 separation. For each orbit the present-day, line-of-sight velocity was calculated for each viewing point and the overall distribution of velocities was analysed. The initial distributions from which a and e values were drawn, suggested that, although their velocities lie in the wings of the distribution, And XII and And XIV are less unusual than we conclude from observations. We were able to change the distributions in order to better match the observed mean host-satellite separation for the M31 population and the ratio of And

XII-like satellites to And XIV-like satellites, although the individual fractions of expected And XII-like and And XIV-like satellites remain higher than observed. So it seems that these “extreme” satellites are not as unusual as previously predicted from analyses employing smooth distribution functions, which predict them to be very rare.

We also ran a second set of simulations where orbits were populated by multiple satellites in order to approximate group infall along a filament. In this case, when only a small number of orbits were modelled, the resulting line-of-sight velocity distributions were highly dependent on the randomly-generated orbits, had means offset from zero and were poorly fit by Gaussians, much like the observed M31-satellite line-of-sight distribution.

Finally, we considered the MW - Leo I system. The approach was very similar to that used for And XII and And XIV, the only difference is that Leo I is moving away from the centre of the MW (whereas And XII and And XIV are moving towards the centre of M31) so Leo I must have already reached pericenter at least once and is now moving back out to apocenter. We found a minimum mass for the MW of $M = 1.6 \times 10^{12} M_{\odot}$, and adopting the Watkins et al. (2010) mass estimate of the MW ($M_{300} = 2.7 \pm 0.5 \times 10^{12} M_{\odot}$), we conclude that Leo I can have completed at most four orbits with a 3-orbit scenario offering the best match.

It seems, then, that the TA method is useful for putting lower constraints on the mass of an external galaxy, as well being an excellent tool for estimating the mass of M31, the MW or the LG. Combining the TA with previous mass estimates, we are able to make estimates of the number of orbits a system has completed. From further analysis, we conclude that And XII and And XIV are not as unusual as previously believed.

6

Discussion & Conclusions

*For I dipt into the Future, far as human eye could see,
Saw the vision of the world, and all the wonder that would be.*

- Alfred Tennyson (1809-1892), Locksley Hall

My thesis has covered three disparate, yet connected, areas; I have searched for substructures in the Galactic halo, I have estimated the masses of the two LG spirals and I have investigated the orbits of two of the M31 satellites thought to be on “extreme” orbits. There is a common theme: in each case, I have used a set of tracer objects to perform the analysis. In the study of the Galactic halo, the tracers were the set of 407 RR Lyraes; in the study of the MW and M31 masses, the tracers were their 55 satellites; and in the study of the And XII and And XIV orbits, the tracers were And XII and And XIV themselves.

In this final chapter, I summarise the work I have presented in this thesis, discuss some recent follow-up work that has been carried out by other groups since we published our discovery of the Pisces Overdensity, and look towards the future in the form of three large, all-sky surveys: Pan-STARRS, LSST and Gaia.

6.1 Chapter Summaries

6.1.1 Variable stars in SDSS Stripe 82

Chapter 2 began with a description of the SDSS and highlighted its importance in the field of Galactic Archaeology. While the survey has generally imaged any given field once or twice only, one particular section of the survey footprint - named Stripe 82 - has been repeatedly imaged over the duration of the survey, with an average of ~ 30 observations per target and as many as 80 observations in some very fortunate cases. This multiple-epoch data is ideal for studies of variability and proper motions,

6 Discussion & Conclusions

and it is to this end that Bramich et al. (2008) created two catalogues from the Stripe 82 data. The first, the LMCC, contains the light-motion-curves for all the objects in the Stripe and the second, the HLC, contains a set of derived quantities for those objects, including mean magnitudes and various statistics to help identify and quantify variability. I described in this chapter how I used the LMCC and HLC to construct a catalogue of the 21 939 variable objects in Stripe 82.

A handful of randomly-selected light-motion curves showed obvious variation and the nature of the variation was varied, with both RR Lyraes and eclipses easily identified; thus, the sample does indeed contain variable stars and the algorithm is sensitive to a variety of different types of variable object.

Following the work of Sesar et al. (2007), I also applied crude colour-colour cuts to the variable sample to distinguish between different types of variable object, finding stellar locus stars to be the dominant population at bright ($g < 19$) magnitudes and low-redshift quasars dominant at faint ($g < 22$) magnitudes. Colour-magnitude diagrams suggested that variable quasars are the most common type of variable object found in the variable catalogue. I also found the RR Lyraes to be significant population across the Stripe.

6.1.2 Substructure revealed by RR Lyraes in SDSS Stripe 82

In Chapter 3, I presented the extraction of a sample of RR Lyrae stars from the variable catalogue described in Chapter 2. 407 RR Lyraes were identified using a combination of cuts based on colour, period, amplitude and metallicity, of which 316 were classified as ab-type RR Lyraes and 91 were c-type RR Lyraes. The RR Lyraes were found to lie at distances 5-115 kpc from the Galactic centre and individual distance estimates, accurate to 5 per cent, were calculated using the colour, period and metallicity to estimate absolute magnitude.

By analysing the distribution of RR Lyraes in Stripe 82, I found that the region is dominated by three enormous substructures. The Hercules-Aquila Cloud, containing 237 RR Lyraes, and the Sagittarius Stream, containing 55 RR Lyraes, were previously known to exist in that part of the sky.

The Hercules-Aquila Cloud is the dominant source of RR Lyraes in Stripe 82, with almost 60% of the sample contained therein. It is possible that there may be some contamination from a smooth component of RR Lyraes associated with the Galactic Bulge and Spheroid, which we are unable to disentangle with the data currently available, however such a population could in no way account for the entire Hercules-Aquila detection; the substructure initially identification by Belokurov et al. (2007) definitely exists. Given the number of RR Lyraes in the Stripe 82 detection and the predicted total extent of the structure, I estimate that the total number of RR Lyraes associated with the Cloud is 2×10^4 . The Hercules-Aquila RR Lyraes lie at distances from the Galactic Centre of 20.2 ± 11.3 kpc, and are metal-poor with $[\text{Fe}/\text{H}] = -1.42 \pm 0.24$.

Both leading and trailing arms of the Sagittarius Stream are believed intersect Stripe 82. Simulations predict that the leading wrap is closer in heliocentric distance than the trailing, but the locations of the arms are not accurately known in this region of the sky. The heliocentric distances of the Stripe 82 Sagittarius RR Lyraes, which predominantly are associated with the trailing arm, have a mean of 26.2 kpc and a dispersion of 5.5 kpc, whilst their metallicity is $[\text{Fe}/\text{H}] = -1.41 \pm 0.19$.

The third substructure, the Pisces Overdensity, was previously unknown and was identified as

an group of 28 RR Lyraes at a distance of centred on Galactic coordinates of ($\ell \approx 80^\circ, b \approx -55^\circ$). The mean distance of the group is ~ 80 kpc, thus making it one of the most distant clumps so far found in the halo. The Pisces Overdensity is clearly distinct from both the Hercules-Aquila Cloud and the Sagittarius Stream and, although its location is close to the Magellanic Plane, it is much more distant than the Magellanic Clouds so neither is it associated with the Magellanic Stream. I also described an order-of-magnitude estimate of the total mass associated with the Overdensity as at least $\sim 10^4 M_\odot$. The associated RR Lyrae have a metallicity $[\text{Fe}/\text{H}] = -1.47 \pm 0.34$, comparable to the Hercules-Aquila Cloud, but richer than the typical populations in the outer halo.

With nearly 80% of the RR Lyraes in the Stripe associated with identified substructures, it is clear that the distribution of RR Lyraes in the halo is strongly clumped, with little, or even no, smooth underlying halo component. Nevertheless, I show that the best fit to the RR Lyrae density distribution is provided by a broken power-law model, with the number density of RR Lyrae falling slowly with Galactocentric radius r like $n(r) \sim r^{-2.4}$ for $5 < r < 23$ kpc and then more sharply as $n(r) \sim r^{-4.5}$ for $23 < r < 100$ kpc. Of course, we must bear in mind here that smooth, spherically-averaged density laws can only provide crude approximations to the true nature of the halo, as substructure is so dominant.

The work presented in this chapter illustrated the suitability of RR Lyraes as standard candles and, thus, their utility as tracers of substructure in the halo. The dominance of substructures in this part of the sky, especially when considered together with earlier SDSS discoveries (Belokurov et al., 2007; Juric et al., 2008) lends further support to the theory that stellar halos are built predominantly, or even solely, from accreted satellites (e.g. Bullock & Johnston, 2005; Bell et al., 2008) with little or no underlying component formed in situ.

6.1.3 Masses of the Milky Way and Andromeda Galaxies

In Chapter 4, I derived a set of robust tracer mass estimators, and discussed the conditions under which they converge. Previous estimators of this type have only considered projected distance and line-of-sight velocity data, however there is often more data available to us. To be able to exploit this additional data, I have derived a modified form of the tracer mass estimator which requires actual distance instead of just projected distance, and a further modification that incorporates proper motion data as well.

These tracer mass estimators, as the name suggests, are applicable to any tracer population for which position and velocity information exists - BHB stars, GCs, dSph galaxies and planetary nebulae are typical examples - and compute the enclosed mass within the outermost datapoints. In order to test their efficacy, I ran a series of Monte Carlo simulations, from which I was also able to quantify the size of the errors on each estimator. They are considerably simpler to use than distribution-function-based methods (see e.g. Little & Tremaine, 1987; Kulessa & Lynden-Bell, 1992; Wilkinson & Evans, 1999), and involve no more calculation than taking weighted averages of combinations of the positional and kinematical data. Their ease of use and the range of datasets to which they may be applied make them incredibly useful.

The exact form of the estimator used will depend on the type of data that is available for the population in question and, if different parts of the data set contain different types of data, then two

6 Discussion & Conclusions

forms of the estimator can be used together, in order to best exploit all the data at our disposal. For example, I show that if only a subset of a given dataset has associated proper motion information, then we can use the proper motion form of the estimator on that subset and the line-of-sight velocity only form of the estimator on the remainder and combine the results. The resulting estimate is better than could be achieved using the line-of-sight velocity form of the estimator on the entire dataset or the proper motion form of the estimator on only the subset with proper motions.

The mass estimators were then applied to the satellite populations of the MW and M31 to find the masses of both galaxies within 300 kpc. The MW satellite population has been used previously in numerous studies of the MW mass, although never with a tracer mass estimator and most such studies were carried out before the recent burst of MW satellite discoveries. Similarly, the size of the M31 satellite population has nearly doubled since the last study to apply a tracer mass estimator to M31 was completed.

In order to apply the mass estimators to the data it was necessary to make some assumptions about the velocity anisotropy of the satellites. Results from N-body cosmological simulations suggest that velocity anisotropy is positive, favouring radial orbits, whereas the limited proper motion data that exists for the satellite suggests a negative velocity anisotropy, favouring negative orbits. In the absence of any further knowledge, I provided three mass estimates, one with the velocity anisotropy obtained from simulations, one that assumes velocity isotropy and one with a velocity anisotropy obtained from the data; finding the former of these estimates to be the smallest and the latter the largest.

There was also some question as to whether all of the satellites should be included when performing the mass estimates. Leo I has long been known to bias mass estimates due to its line-of-sight velocity, which is larger than would be expected given its distance from the centre of the MW. A quick check of the contributions made to the mass estimate by each individual satellite reveal that Leo I was by far the dominant contributor, with Hercules also making a significantly large contribution. A similar analysis of the M31 satellites revealed that And XII and And XIV were outliers in that population, with mass contributions far larger than those provided by the other satellites. This result was not wholly surprising as And XII and And XIV have both been highlighted in the literature as “extreme” satellites that are very possibly on their first infall into M31 (as I considered in great detail in Chapter 5). Finally, Draco was found to contribute nearly half of the mass estimate when the proper motions of the MW satellites were also considered. In light of these anomalous satellites, the mass estimates were made both with and without their inclusion in the population samples.

The preferred mass estimates come from accepting Leo I, Hercules, And XII and And XIV as bound satellites, whilst discarding the Draco proper motion as inaccurate. This gives an estimate for the mass of the MW within 300 kpc as $2.7 \pm 0.5 \times 10^{12} M_{\odot}$ and for M31 as $1.5 \pm 0.4 \times 10^{12} M_{\odot}$, assuming the mildly tangential anisotropy implied by the data ($\beta \approx -4.5$). The error bars are just the statistical uncertainty and do not incorporate the uncertainty in anisotropy or sample membership.

These values for the masses are attractive for a number of reasons. First, the mass ratio between the MW and M31 is of order unity, which is in agreement with a number of other lines of evidence. Second, the values allow most of the dark matter in the LG implied by the Timing Argument to be clustered around the two most luminous galaxies. Third, they are within the range found for cosmologically motivated models of the MW and M31 (Li & White, 2008).

While M31 is believed to have the more massive stellar halo, these numbers suggest that the MW inhabits the larger dark halo, however in view of the uncertainties present, it is not possible to say for certain if this is indeed the case based on the kinematic data currently available.

6.1.4 Application of the Timing Argument to host-satellite systems

In Chapter 5, I applied the TA to the M31-And XII and M31-And XIV systems in order to derive the properties of their orbits. The TA has never before been applied to two galaxies outside of the MW, so it was first necessary to adapt the TA method for use with two external galaxies. Assuming that the satellites are on their first orbits of M31, it was possible to place lower limits on the mass of M31; finding a minimum mass of $M = 1.1 \times 10^{12} M_{\odot}$ from the M31-And XII system and $M = 1.2 \times 10^{12} M_{\odot}$ from the M31-And XIV system. These lower limits are consistent with previous mass estimates, and they show remarkable agreement with each other, increasing confidence in this method, despite a number of assumptions it was necessary to make in the process. More information regarding the nature of the host-satellite orbits was obtained by combining the TA results with previous mass estimates (specifically those found in Chapter 4). And XII can have completed at most six orbits of M31, with a 4-orbit scenario giving the best match to the mass estimate. Similarly, And XIV can have completed only 3 orbits of M31, with the 2-orbit scenario being the best match. The same methods applied to the MW-Leo I system, estimated a minimum mass for the MW of $M = 1.6 \times 10^{12} M_{\odot}$, and suggest that Leo I can have completed at most four orbits with a 3-orbit scenario offering the best match. For And XII and And XIV, their SFHs were also predicted by calculating the times of past pericentric passages, which are believed to trigger bursts of SF.

I then considered whether And XII and And XIV really are satellites on “extreme” orbits compared to the general M31 population, or if they are indistinguishable from the rest only viewed from a special direction that serves to give them anomalously high line-of-sight velocities and artificially inflate their significance. I ran a set of Monte Carlo simulations in which the TA methods developed here were applied to generated orbits, with the mass M fixed as the mass of M31 and the host-observer distance fixed as the MW-M31 separation. Semi-major-axis a and eccentricity e were picked from power-law distributions and viewing angles ϕ and θ were picked uniformly over the surface of a sphere and then, for each orbit, the present-day, line-of-sight velocity was calculated for each viewing point and the overall distribution of velocities was analysed. The distributions of a and e were adjusted until the mean separation of the simulated satellites and the ratio of And XII-like satellites to And XIV-like satellites were consistent with the observed population. The results suggest that satellites like And XII and And XIV are reasonably likely; in stark contrast to previous analyses which employed smooth distribution functions to conclude that such satellites are very rare.

Finally, a second set of simulations, designed to simulate group infall along filaments, was also carried out by populating a small number of orbits with multiple satellites. In this case the resulting line-of-sight velocity distributions were highly dependent on the randomly-generated orbits, had means offset from zero and were poorly fit by Gaussians, much like the observed M31-satellite line-of-sight distribution.

It seems, then, that the TA method is reasonably robust for putting lower constraints on the mass of an external galaxy, as well being an excellent tool for estimating the mass of M31, the MW or the

6 Discussion & Conclusions

LG. Combining the TA with previous mass estimates, we are able to make estimates of the number of orbits a system has completed. From further analysis, we conclude that And XII and And XIV are more likely than previously believed.

6.2 Prospects for the Future

6.2.1 The Pisces Overdensity

Since I completed the work described in Chapter 3, a number of groups have since confirmed the detection of the Pisces Overdensity. Sesar et al. (2007) presented a number of possible substructure candidates, of which “Substructure J” was found in the same part of the sky as the Pisces Overdensity. Sesar et al. (2010) found the distance to Substructure J to be ~ 80 kpc, thus confirming that Substructure J and the Pisces Overdensity are spatially coincident, and are, in fact, one and the same. They also conclude that the Overdensity is unlikely to be associated with the Sgr Stream as it is offset from the Stream’s best-fit orbital plane. In the same paper, they also studied a very similar Stripe 82 dataset and reached the same conclusions as I have presented in this thesis regarding the distribution of RR Lyraes in the halo; namely that it is highly inhomogeneous and that there is evidence of a break in the distribution at ~ 30 kpc.

Kollmeier et al. (2009) recently obtained spectroscopic data for 8 RR Lyraes that were thought to be a part of the Pisces Overdensity. They found 5 of those stars to have heliocentric line-of-sight velocities in a very narrow range centred on $\sim -75 \text{ km s}^{-1}$. Monte Carlo simulations conclude that it is very unlikely that such coherent velocity group could be seen by chance, thus confirming that the photometric overdensity is due to a physically associated system. Which begs the question of what exactly is the Pisces Overdensity?

The extent of the structure certainly suggests that the progenitor was fairly large and the velocity dispersion, such as it is with only 5 stars to contribute to it, is similar to those of the Sgr Stream and the Monoceros Stream, both of which have dSph progenitors. Estimates of its mass also indicate that it is of a similar mass to dSph halos. So it seems that the spectroscopic results support a conclusion that the progenitor is a dSph galaxy and not a GC, but whether it is still bound or has already become unbound is less clear. Kollmeier et al. (2009) cannot rule out the possibility that it is virialised, however with such a small sample of stars for an object that covers such a large area, neither can they rule out the possibility that it has been completely disrupted either.

The remaining 3 stars in the sample, are very definitely offset from the other 5, with velocities of $\sim -190 \text{ km s}^{-1}$, and 2 of the 3 have velocities that are remarkably similar, differing by only 9 km s^{-1} . This suggests that they could be part of a second object; with so few objects there is insufficient evidence to make such a claim with any certainty but it is not an unreasonable assumption to make. It is unlikely to find velocities so offset from the main Pisces detection simply due to the effects of disruption, and overlapping substructures are not uncommon - the Sgr Stream is known to overlap with other objects in the halo. And if the halo is indeed predominantly or entirely built up as a result of mergers and accretions (see e.g. Bullock & Johnston, 2005; Bell et al., 2008), as is increasingly accepted to be the case, then we would expect to see substructures overlapping one another.

Sesar et al. (2010) obtained spectra for a further 5 stars in the Pisces Overdensity and analysed them alongside the Kollmeier et al. (2009) stars. They found evidence that the substructure is composed of two different kinematic groups, in line with previous results, although they argue that the data do not yet allow us to identify whether the two groups had a common progenitor or if they are the remnants from two different objects. They found both groups to be very spatially extended and thus argue that they are likely to be unbound.

In summary, the Pisces Overdensity is definitely a real object in the halo of the MW but its nature remains unknown. It could be part of a stream left behind as a satellite was torn apart on its passage through the MW halo, it could be the remnants of the core of a disrupted satellite, possibly already unbound. The Kollmeier et al. (2009) spectroscopic data suggests the Pisces stars are, or were once, part of a dSph galaxy, and Sesar et al. (2010) further suggest that the object is unbound, but with so few stars on which to base their hypothesis, these claims must be treated with some caution. There is also evidence that the Pisces Overdensity contains two kinematic groups, though whether they are of common origin cannot yet be confirmed.

Further photometry extending beyond the limits of Stripe 82 will be vital in determining the extent of this curious object, and the additional data will also enable us to better understand its properties, however this data will ideally be coupled to spectroscopic information if we are to be able to determine its nature with confidence.

6.2.2 Surveys

In Section 1.2.4 and Section 1.3 of my introduction, I discussed some recent surveys that have been instrumental in furthering our knowledge of the LG. The survey of Andromeda's stellar halo carried on the CFHT and, more recently, the SPLASH and PAndAS surveys have greatly improved our view of M31. A host of new satellites have been discovered - a fact we exploited in Chapter 4 and two of which we studied in Chapter 5 - and the halo has been explored in great detail, and mapped out to a distance far larger than would have been predicted a decade ago. The story is much the same for the MW. The 2MASS survey of red giant stars and the SEKBO and QUEST RR Lyrae surveys have provided us with a host of high-quality datasets which have been analysed in great detail in order to probe the halo; and to which RAVE and OGLE have contributed unparalleled spectroscopic information.

However, the single most significant contribution to the field of Galactic Archaeology in recent years has arguably been that made by the SDSS, as I discussed in Chapter 2. Before SDSS, the census of MW satellites stood at just nine and the rate of discovery was one or two per decade; that number has since more than tripled, with 29 satellites currently known and, while the rate of discovery has tailed off somewhat from its peak, new discoveries are still being reported every few months. Further, the SDSS has allowed us to explore the Galactic halo in unprecedented detail and to depths never before achieved on such a large scale - the SDSS footprint covers nearly a quarter of the sky.

Of course, this also means that the SDSS footprint covers *only* a quarter of the sky. Other surveys have done their bit in attempts to study the rest of the halo, however coverage from other surveys is patchy, meaning that some parts of the sky have been studied in great detail while other parts remain largely unexplored.

The next generation of large surveys will change that.

6 Discussion & Conclusions

The Panoramic Survey Telescope And Rapid Response System (Pan-STARRS) project is one such ground-based survey. A prototype single-mirror telescope is already operational and taking data; however the actual Pan-STARRS telescope will use four mirrors and should be operational late in 2011 or early in 2012. It will use wide-field, repetitive imaging techniques to scan approximately three-quarters of the sky down to a limiting magnitude of 24, which corresponds to a distance of around 10 Mpc for variable stars at this magnitude. The primary focus of the project is to search for relatively nearby objects which may be potentially hazardous to our solar system, however the nature of the observations means that the importance of Pan-STARRS will reach much further into many different branches of astronomy. The survey will observe the entire available sky several times each month to build up a vast catalogue of objects and the repeated nature of the observations will reveal both object variability and proper motions. I have already shown in this thesis how important variability information is in the study of the Galactic halo by studying the small patch of sky known as Stripe 82 - an area that is not even 1% of that covered by Pan-STARRS. The large extent and high sensitivity of this project is very exciting; the SDSS has produced and continues to produce some very important science and yet it covers only a third of the area that Pan-STARRS will cover and with lower sensitivity, so the prospects for Pan-STARRS are excellent.

The Large Synoptic Survey Telescope (LSST) is another ground-based wide-field survey, primarily targeting the Southern sky, with the stated mission goals of investigating the nature of dark energy, the solar system, optical transients and Galactic structure. It is much further away from completion than Pan-STARRS - with first light planned for 2016 and survey operations expected to begin in 2018 - but it will definitely be worth waiting for. LSST will take data in 6 passbands (the SDSS ugriz bands plus the Y band) down to a limiting magnitude of $V \sim 25$ and it will be able to cover the entirety of the available sky every three nights. The extent of the survey will be less than that of the Pan-STARRS, although it will still eclipse the SDSS coverage, and the depth it will be able to reach will exceed both. Again, the extent and depth of the survey will make it incredibly useful in the study of the Galactic halo, the multiband nature of the observations will greatly aid in the classification of different types of object and the sheer number of observations will enable the measurement of proper motions and make it an ideal dataset in which to search for variable objects.

Another upcoming survey is Gaia, a space telescope, due to be launched in December 2011, that will be positioned at the L2 Lagrange point that is already home to WMAP, Planck and Herschel and where it will also be joined by the JWST. From L2 the entire celestial sphere can be observed during the course of one year and, since the Earth, Moon and Sun all lie within the orbit of the L2 point, the satellite will be able to work uninterrupted. Gaia's mission is to make the largest, most precise, three-dimensional map of our galaxy by surveying around one billion stars in the MW and throughout the LG; each of the one billion objects will be observed down to a magnitude of $V = 20$ approximately 100 times over the predicted five-year lifetime of the project, building up a huge catalogue of astrometry, photometry and spectrometry. Although lacking the depth that Pan-STARRS and LSST will be able to achieve, and even that the SDSS has attained, out at L2, away from the Earth's atmosphere and able to work undisturbed, the data that Gaia collects will be of very high precision, which is vital if we want to push forward in this field. Of course the precision of the measurements will depend upon the brightness of any given object; even for the faintest, the accuracy will be very good and for the brightest objects the accuracy will be quite remarkable. Distances are predicted to be accurate to 300

μas for objects at $V = 20$, improving to $\sim 10\mu\text{as}$ for the brightest objects and proper motions will be accurate to 5 - 150 $\mu\text{as yr}^{-1}$.

What implications will these datasets have for projects like those I have described in my thesis? For a start, the analysis of the Pisces Overdensity I have presented here was limited by both the extent of the SDSS survey and by the faint magnitudes of member stars as Pisces is so far away. Stripe 82 is so thin that we are only seeing a section of Pisces and we cannot tell how far it extends either side of the Stripe. The large distance range we observe in the member stars hints that it is an extended object, but there is no way to be sure without data further away from the plane of the Galaxy. And deeper data would have been very welcome, as it would have allowed us to identify more, fainter members. Pisces has already been targeted for follow-up projects and by the time any of these datasets come along, it is likely that the region around Pisces will have been mapped in better detail and to fainter magnitudes; although this does not mean that these wide-field surveys will be useless. On the contrary, follow-up projects will still only be able to target small, scattered fields in order to probe the extent of the overdensity and spectroscopy will be limited to only a handful of stars, while the all-sky surveys will provide more even and complete coverage of the entire region.

And, of course, it is not only existing structures like Pisces, Hercules-Aquila and Sagittarius that will be detected by such data, although, of course, this is true; more new substructures and streams will be discovered in the halo. Furthermore, we will be able to extend the analyses of the halo density presented in Chapter 3 over a much larger area of the sky. Perhaps we will finally be able to distinguish between substructure and the underlying smooth halo and determine how much of galaxy was formed in situ?

One of the main conclusions from the tracer mass estimator work I presented was that proper motion data for a tracer population can greatly improve the accuracy with which we are able to estimate the mass of their host. At least in theory; simulations showed this to be the case, but our analysis was hampered in this regard by the scarcity of proper motion measurements for the MW satellites, and the large errors generally placed on the measurements that do exist. Another significant source of error for the mass estimates is that we are unable to determine with confidence the velocity anisotropy of the satellite populations or either of the LG spirals. However, there is light on the horizon; Gaia will obtain proper motion data for all of the satellites of the MW and M31 (as well as for many hundreds of thousands of halo stars) and with far better accuracy than we are able to achieve with current studies. This will both allow us to constrain the velocity anisotropy and provide for improved mass estimates and uncertainties.

Another significant source of error in that work is the question of whether anomalous satellites like Leo I, And XII and And XIV should be included in the analysis. The TA work described in Chapter 5 attempted to make sense of And XII and And XIV, but that too was subject to some uncertainty. The galaxies are so faint that only a small number of stars have so far been detected within them, which means that any properties derived are subject to large errors, and no proper motion estimates are possible with current instruments, which means that their velocity anisotropy is unknown. With these limitations, we were forced to adopt a velocity anisotropy that gave a minimum mass estimate for the host system. The data we obtain from Pan-STARRS, LSST and Gaia will help us here once again, enabling us to break the mass-anisotropy degeneracy and providing improved data for the satellites.

So far I have talked about improving the quality of the data that already exists, but that is only

6 Discussion & Conclusions

one way in which these studies will benefit. Increased coverage of the sky to SDSS magnitude limits and deeper will undoubtedly reveal a plethora of new satellites for our study; this will increase the number of objects we are able to use to find mass estimates, tightening the errors still further. In addition, the general properties of the satellites will also be better understood as not only will we have better data for existing objects, but we will increase the sample sizes that we are able to study. Whether or not the common dark halo mass of dSphs (see Section 1.4.4 and Figure 1.5) is able to withstand an influx of new satellites remains to be seen, as does the question of whether the apparent separation of GCs and dSphs in half-light radius is real (see Section 1.4.3 and Figure 1.4). The missing satellite problem (Section 1.1.3) is predicted to be alleviated by discoveries of new galaxies in the little-studied parts of the halo, but it is not clear whether such discoveries will completely solve the problem or only ameliorate the discrepancy.

New satellites and new substructures in the halo, these are the things we expect to find; we don't know how many there are or where exactly they will be, but we know enough to be confident that they are there waiting for us discover them. But what else might be out there?

Looking towards the future, we see three large, deep all-sky surveys which will be coming online soon, giving astronomers a wealth of data to play with; but this data will be nothing without the software to analyse it. The analysis of the data is the key here; programs must be written capable of disseminating the data in a useful format so that it can be manipulated and searched as required. These surveys will produce massive amounts of data in a single night, so the software must be capable of coping with these large amounts of data and must work quickly and efficiently.

Technical challenges notwithstanding, the possibilities that will be opened up when these three large surveys come online are endless and this is an incredibly exciting time to be working in this field. There is so much that can be done with the data that already exists and the prospects for the future are bright so we have every cause to be optimistic.

Here I have concentrated on the importance of these surveys to the field of Galactic Archaeology and the study of the LG, however this does not fully encompass the scope of the surveys. These telescopes will not view only local objects but any object on the sky which is bright enough to be seen by the telescope in question; including objects such as supernovae and quasars. With all the available data, it is not just our own galaxy and its nearest neighbours that can be probed in detail. The formation and evolution of other nearby galaxies can also be investigated, as well as the formation and subsequent evolution of the universe as a whole. These projects will also provide valuable new tests from general relativity and cosmology.

This really is just the tip of the iceberg.

A

Coordinate and velocity calculations

In Section 4.3.4, I describe how radial velocity data may be complemented by proper motion data in order to obtain more accurate mass estimates than can be obtained with radial velocities alone. Table 4.4 presents the proper motions in the equatorial coordinate system for M31 and for the handful of MW and M31 satellites for which proper motions exist. In Section 5.2, I describe the distance and velocity data needed to apply the Timing Argument to M31 and its satellites.

In order to make use of these data, we first need to convert from equatorial to Galactic proper motions; these must then be transformed into transverse velocities and then corrected for solar peculiar motion and the motion of the Local Standard of Rest (LSR) in order to obtain Galactocentric velocities. I will outline this process below.

However, before I continue any further, I must define what I mean by *proper motion*. Throughout this discussion, I adopt the following definitions of proper motion, where μ_α and μ_ℓ have been corrected for declination and latitude respectively.

$$\begin{aligned}\mu_\alpha &= \dot{\alpha} \cos \delta & \mu_\delta &= \dot{\delta} \\ \mu_\ell &= \dot{\ell} \cos \delta & \mu_b &= \dot{b}\end{aligned}$$

A.1 Converting from equatorial to Galactic coordinates

The Galactic coordinate system is defined by three angles: the equatorial position of the North Galactic Pole (NGP) (α_G, δ_G) and the position of the North Celestial Pole (NCP) relative to the great semicircle passing through the NGP and zero Galactic longitude ℓ_C .

In J2000, these take the values:

$$\alpha_G = 192^\circ.86 \quad \delta_G = +27^\circ.13 \quad \ell_C = 122^\circ.93$$

A Coordinate and velocity calculations

Equatorial coordinates (α, δ) and Galactic coordinates (ℓ, b) are related via:

$$\begin{pmatrix} \cos b \cos \ell \\ \cos b \sin \ell \\ \sin b \end{pmatrix} = \mathbf{T} \begin{pmatrix} \cos \delta \cos \alpha \\ \cos \delta \sin \alpha \\ \sin \delta \end{pmatrix} \quad (\text{A.1})$$

where

$$\mathbf{T} = \begin{pmatrix} \cos \ell_c & \sin \ell_c & 0 \\ \sin \ell_c & -\cos \ell_c & 0 \\ 0 & 0 & 1 \end{pmatrix} \begin{pmatrix} -\sin \delta_G & 0 & \cos \delta_G \\ 0 & -1 & 0 \\ \cos \delta_G & 0 & \sin \delta_G \end{pmatrix} \begin{pmatrix} \cos \alpha_G & \sin \alpha_G & 0 \\ \sin \alpha_G & -\cos \alpha_G & 0 \\ 0 & 0 & 1 \end{pmatrix} \quad (\text{A.2})$$

Hence,

$$\cos b \cos \ell = -\cos \ell_c \sin \delta_G \cos \delta \cos(\alpha - \alpha_G) + \sin \ell_c \cos \delta \sin(\alpha - \alpha_G) + \cos \ell_c \cos \delta_G \sin \delta \quad (\text{A.3})$$

$$\cos b \sin \ell = -\sin \ell_c \sin \delta_G \cos \delta \cos(\alpha - \alpha_G) - \cos \ell_c \cos \delta \sin(\alpha - \alpha_G) + \sin \ell_c \cos \delta_G \sin \delta \quad (\text{A.4})$$

$$\sin b = \cos \delta_G \cos \delta \cos(\alpha - \alpha_G) + \sin \delta_G \sin \delta \quad (\text{A.5})$$

Now, we have data μ_α and μ_δ and we require μ_ℓ and μ_b . We start by considering $\sin \ell_c$ (A.3) – $\cos \ell_c$ (A.4):

$$\cos b \sin(\ell_c - \ell) = \cos \delta \sin(\alpha - \alpha_G) \quad (\text{A.6})$$

Differentiating (A.5), we obtain \dot{b} as a function of $\dot{\alpha}$ and $\dot{\delta}$:

$$\dot{b} = \frac{(\sin \delta_G \cos \delta - \cos \delta_G \sin \delta \cos(\ell_c - \ell)) \dot{\delta} - \cos \delta_G \cos \delta \sin(\alpha - \alpha_G) \dot{\alpha}}{\cos b} \quad (\text{A.7})$$

Differentiating (A.6), we obtain $\dot{\ell}$ as a function of \dot{b} , $\dot{\alpha}$ and $\dot{\delta}$:

$$\dot{\ell} = \frac{\sin \delta \sin(\alpha - \alpha_G) \dot{\delta} - \cos \delta \cos(\alpha - \alpha_G) \dot{\alpha} - \sin b \sin(\ell_c - \ell) \dot{b}}{\cos b \sin(\ell_c - \ell)} \quad (\text{A.8})$$

Finally, proper motions are obtained via $\mu_\ell = \dot{\ell} \cos b$ and $\mu_b = \dot{b}$.

A.2 Galactocentric spatial velocities

We wish to use heliocentric line of sight velocities v_{los} (km s^{-1}) and proper motions (μ_ℓ, μ_b) (mas yr^{-1}) to determine full Galactocentric spatial velocities. We start by converting the proper motions into velocities (v_ℓ, v_b) (km s^{-1}):

$$v_\ell = 4.74 \mu_\ell d \quad v_b = 4.74 \mu_b d$$

where d (kpc) is the heliocentric distance. The factor of 4.74 converts AU yr^{-1} to km s^{-1} .

Now we compute the velocities in the Heliocentric Rest Frame (HRF) via

$$\mathbf{v}_{\text{HRF}} = \begin{pmatrix} \cos b \cos \ell & -\sin b \cos \ell & -\sin \ell \\ \cos b \sin \ell & -\sin b \sin \ell & \cos \ell \\ \sin b & \cos b & 0 \end{pmatrix} \begin{pmatrix} v_{\text{los}} \\ v_{\ell} \\ v_b \end{pmatrix} \quad (\text{A.9})$$

We correct for solar peculiar motion and the motion of the Local Standard of Rest (LSR) to obtain the velocity in the Galactocentric Rest Frame (GRF) using

$$\mathbf{v}_{\text{GRF}} = \mathbf{v}_{\text{HRF}} + \mathbf{v}_{\odot} + \mathbf{v}_{\text{LSR}} \quad (\text{A.10})$$

where $\mathbf{v}_{\odot} = (+10 \pm 0.36, +5.25 \pm 0.62, +7.17 \pm 0.38) \text{ km s}^{-1}$ is the solar peculiar motion with respect to the LSR (Dehnen & Binney, 1998) and $\mathbf{v}_{\text{LSR}} = (0, 220, 0) \text{ km s}^{-1}$ is the speed of the LSR. Note that here we assume a right-handed coordinate system.

A.3 M31-centric spatial velocities

The above calculations allow us to calculate the velocity of an object in a frame in which the centre of the Galaxy is at rest. However, this is only of limited use to us. When we consider M31 and its satellites, we often wish to know the velocity of the satellites in a frame in which M31 is at rest (which we will call the M31-centric Rest Frame (MRF)).

We must first correct for peculiar motion and the LSR, using the prescriptions described above to calculate the Galactocentric velocities of M31 and the satellite. We can then correct the velocity of the satellite for the relative motion of M31 and the MW,

$$\mathbf{v}_{\text{MRF,dwarf}} = \mathbf{v}_{\text{GRF,dwarf}} - \mathbf{v}_{\text{GRF,M31}} \quad (\text{A.11})$$

Bibliography

- Aaronson M., 1983, ApJ, 266, L11
- Aaronson M., 1986, in Star-forming Dwarf Galaxies and Related Objects The older stellar population of dwarf galaxies..pp 125–143
- Abadi M. G., Navarro J. F., Steinmetz M., 2006, MNRAS, 365, 747
- Adelman-McCarthy J. K. et al., 2008, ApJS, 175, 297
- Alcock C. et al., 1993, Nature, 365, 621
- Alcock C. et al., 1998, ApJ, 492, 190
- Aparicio A., Carrera R., Martínez-Delgado D., 2001, AJ, 122, 2524
- Armandroff T. E., Olszewski E. W., Pryor C., 1995, AJ, 110, 2131
- Aubourg E. et al., 1993, Nature, 365, 623
- Bahcall J. N., Tremaine S., 1981, ApJ, 244, 805
- Bailey S. I., 1902, Annals of Harvard College Observatory, 38, 1
- Bekki K., Chiba M., 2001, ApJ, 558, 666
- Bell E. F. et al., 2008, ApJ, 680, 295
- Bellazzini M., Ferraro F. R., Origlia L., Pancino E., Monaco L., Oliva E., 2002, AJ, 124, 3222
- Bellazzini M., Gennari N., Ferraro F. R., 2005, MNRAS, 360, 185
- Bellazzini M., Gennari N., Ferraro F. R., Sollima A., 2004, MNRAS, 354, 708
- Belokurov V. et al., 2007, ApJ, 657, L89
- Belokurov V. et al., 2007, ApJ, 658, 337
- Belokurov V. et al., 2008, ApJ, 686, L83
- Belokurov V. et al., 2010, ApJ, 712, L103
- Belokurov V. et al., 2009, MNRAS, 397, 1748
- Belokurov V. et al., 2006, ApJ, 642, L137
- Belokurov V. et al., 2007, ApJ, 654, 897

Bibliography

- Belokurov V. et al., 2006, *ApJ*, 647, L111
- Besla G., Kallivayalil N., Hernquist L., Robertson B., Cox T. J., van der Marel R. P., Alcock C., 2007, *ApJ*, 668, 949
- Binney J., Tremaine S., 1987, *Galactic dynamics*
- Bramich D. M. et al., 2008, *MNRAS*, 386, 887
- Braun R., 1991, *ApJ*, 372, 54
- Brown W. R., Geller M. J., Kenyon S. J., Diaferio A., 2010, *AJ*, 139, 59
- Brunthaler A., Reid M. J., Falcke H., Greenhill L. J., Henkel C., 2005, *Science*, 307, 1440
- Brunthaler A., Reid M. J., Falcke H., Henkel C., Menten K. M., 2007, *A&A*, 462, 101
- Brunthaler A., Reid M. J., Falcke H., Henkel C., Menten K. M., 2008, in Jerjen, H. & Koribalski, B. S. ed., *Galaxies in the Local Volume Proper Motions in the Andromeda Subgroup*.pp 211–+
- Bullock J. S., Johnston K. V., 2005, *ApJ*, 635, 931
- Burstein D., 1979, *ApJ*, 234, 829
- Cáceres C., Catelan M., 2008, *ApJS*, 179, 242
- Carney B. W., Laird J. B., Latham D. W., Aguilar L. A., 1996, *AJ*, 112, 668
- Carollo D. et al., 2007, *Nature*, 450, 1020
- Carrera R., Aparicio A., Martínez-Delgado D., Alonso-García J., 2002, *AJ*, 123, 3199
- Chapman S. C., Ibata R., Lewis G. E., Ferguson A. M. N., Irwin M., McConnachie A., Tanvir N., 2006, *ApJ*, 653, 255
- Chapman S. C. et al., 2007, *ApJ*, 662, L79
- Chiba M., Beers T. C., 2001, *ApJ*, 549, 325
- Chou M. et al., 2007, *ApJ*, 670, 346
- Cioni M., van der Marel R. P., Loup C., Habing H. J., 2000, *A&A*, 359, 601
- Clark D. H., Stephenson F. R., 1977, *The historical supernovae*
- Cole A. A. et al., 1999, *AJ*, 118, 1657
- Coleman M. G., de Jong J. T. A., 2008, *ApJ*, 685, 933
- Coleman M. G. et al., 2007, *ApJ*, 668, L43
- Collinge M. J., Sumi T., Fabrycky D., 2006, *ApJ*, 651, 197
- Collins M. L. M. et al., 2009, *ArXiv e-prints*
- Costa E., Méndez R. A., Pedreros M. H., Moyano M., Gallart C., Noël N., Baume G., Carraro G., 2009, *AJ*, 137, 4339
- Cote P., Mateo M., Olszewski E. W., Cook K. H., 1999, *ApJ*, 526, 147
- Crain R. A. et al., 2009, *MNRAS*, 399, 1773

- Croom S. M., Smith R. J., Boyle B. J., Shanks T., Miller L., Outram P. J., Loaring N. S., 2004, MNRAS, 349, 1397
- Dall’Ora M. et al., 2003, AJ, 126, 197
- de Jong J. T. A., Martin N. F., Rix H., Smith K. W., Jin S., Macciò A. V., 2010, ApJ, 710, 1664
- De Propriis R., Harrison C. D., Mares P. J., CTIO University C., 2010, ArXiv e-prints
- Deason A. J., Belokurov V., Evans N. W., 2010, ArXiv e-prints
- Dehnen W., Binney J. J., 1998, MNRAS, 298, 387
- Diemand J., Kuhlen M., Madau P., 2007, ApJ, 667, 859
- Dilday B. et al., 2008, ApJ, 682, 262
- Drimmel R., Spergel D. N., 2001, ApJ, 556, 181
- Duffau S., Zinn R., Vivas A. K., Carraro G., Méndez R. A., Winnick R., Gallart C., 2006, ApJ, 636, L97
- Eggen O. J., Lynden-Bell D., Sandage A. R., 1962, ApJ, 136, 748
- Einasto J., Lynden-Bell D., 1982, MNRAS, 199, 67
- Elmegreen B. G., 1999, ApJ, 517, 103
- Evans N. W., Hafner R. M., de Zeeuw P. T., 1997, MNRAS, 286, 315
- Evans N. W., Wilkinson M. I., 2000, MNRAS, 316, 929
- Evans N. W., Wilkinson M. I., Guhathakurta P., Grebel E. K., Vogt S. S., 2000, ApJ, 540, L9
- Evans N. W., Wilkinson M. I., Perrett K. M., Bridges T. J., 2003, ApJ, 583, 752
- Fardal M. A., Babul A., Geehan J. J., Guhathakurta P., 2006, MNRAS, 366, 1012
- Fardal M. A., Babul A., Guhathakurta P., Gilbert K. M., Dodge C., 2008, ApJ, 682, L33
- Fardal M. A., Guhathakurta P., Babul A., McConnachie A. W., 2007, MNRAS, 380, 15
- Fellhauer M. et al., 2006, ApJ, 651, 167
- Fellhauer M. et al., 2007, MNRAS, 375, 1171
- Feltzing S., Gilmore G., 2000, A&A, 355, 949
- Ferguson A. M. N., Irwin M. J., Ibata R. A., Lewis G. F., Tanvir N. R., 2002, AJ, 124, 1452
- Freedman W. L. et al., 2001, ApJ, 553, 47
- Frenk C. S., White S. D. M., 1982, MNRAS, 198, 173
- Frieman J. A. et al., 2008, AJ, 135, 338
- Fukugita M., Ichikawa T., Gunn J. E., Doi M., Shimasaku K., Schneider D. P., 1996, AJ, 111, 1748
- Geha M., Willman B., Simon J. D., Strigari L. E., Kirby E. N., Law D. R., Strader J., 2009, ApJ, 692, 1464
- Georgelin Y. M., Georgelin Y. P., 1976, A&A, 49, 57

Bibliography

- Gilbert K. M. et al., 2006, ApJ, 652, 1188
- Gilbert K. M. et al., 2009, ApJ, 705, 1275
- Gilmore G., Reid N., 1983, MNRAS, 202, 1025
- Gilmore G., Wilkinson M. I., Wyse R. F. G., Kleya J. T., Koch A., Evans N. W., Grebel E. K., 2007, ApJ, 663, 948
- Gilmore G., Wyse R. F. G., Norris J. E., 2002, ApJ, 574, L39
- Gott III J. R., Thuan T. X., 1978, ApJ, 223, 426
- Gottesman S. T., Hunter J. H., Boonyasait V., 2002, MNRAS, 337, 34
- Gould A., Kollmeier J. A., 2004, ApJS, 152, 103
- Grillmair C. J., 2006, ApJ, 645, L37
- Grillmair C. J., 2009, ApJ, 693, 1118
- Guhathakurta P., Ostheimer J. C., Gilbert K. M., Rich R. M., Majewski S. R., Kalirai J. S., Reitzel D. B., Patterson R. J., 2005, ArXiv Astrophysics e-prints
- Gunn J. E. et al., 1998, AJ, 116, 3040
- Gunn J. E. et al., 2006, AJ, 131, 2332
- Harris J., Zaritsky D., 2006, AJ, 131, 2514
- Hartwick F. D. A., 1987, in G. Gilmore & B. Carswell ed., NATO ASIC Proc. 207: The Galaxy The structure of the Galactic halo. pp 281–290
- Heisler J., Tremaine S., Bahcall J. N., 1985, ApJ, 298, 8
- Helmi A., 2004, ApJ, 610, L97
- Helmi A., White S. D. M., 1999, MNRAS, 307, 495
- Hodge P., 1989, ARA&A, 27, 139
- Hogg D. W., Finkbeiner D. P., Schlegel D. J., Gunn J. E., 2001, AJ, 122, 2129
- Hubble E. P., 1936, Realm of the Nebulae
- Hurley-Keller D., Mateo M., Nemec J., 1998, AJ, 115, 1840
- Huxor A. P., Tanvir N. R., Irwin M. J., Ibata R., Collett J. L., Ferguson A. M. N., Bridges T., Lewis G. F., 2005, MNRAS, 360, 1007
- Ibata R., Irwin M., Lewis G., Ferguson A. M. N., Tanvir N., 2001, Nature, 412, 49
- Ibata R., Martin N. F., Irwin M., Chapman S., Ferguson A. M. N., Lewis G. F., McConnachie A. W., 2007, ApJ, 671, 1591
- Ibata R. A., Gilmore G., Irwin M. J., 1995, MNRAS, 277, 781
- Ibata R. A., Wyse R. F. G., Gilmore G., Irwin M. J., Suntzeff N. B., 1997, AJ, 113, 634

- Irwin M. J. et al., 2007, ApJ, 656, L13
- Irwin M. J., Bunclark P. S., Bridgeland M. T., McMahon R. G., 1990, MNRAS, 244, 16P
- Irwin M. J., Ferguson A. M. N., Huxor A. P., Tanvir N. R., Ibata R. A., Lewis G. F., 2008, ApJ, 676, L17
- Ivezic Ž. et al., 2000, AJ, 120, 963
- Ivezic Z., Lupton R., Schlegel D., Johnston D., Gunn J., Knapp J., Strauss M., Rockosi C., 2004, in Clemens D., Shah R., Brainerd T., eds, *Milky Way Surveys: The Structure and Evolution of our Galaxy* Vol. 317 of *Astronomical Society of the Pacific Conference Series*, *Reaching to the Edge of the Milky Way Halo with SDSS*.pp 179–+
- Ivezic Z. et al., 2004, *Astronomische Nachrichten*, 325, 583
- Ivezic Ž. et al., 2007, AJ, 134, 973
- Ivezic Z., Vivas A. K., Lupton R. H., Zinn R., 2005, AJ, 129, 1096
- Jablonka P., Martin P., Arimoto N., 1996, AJ, 112, 1415
- Jin S., Lynden-Bell D., 2007, MNRAS, 378, L64
- Johnston K. V., Law D. R., Majewski S. R., 2005, ApJ, 619, 800
- Jurcsik J., Kovacs G., 1996, A&A, 312, 111
- Juric M. et al., 2008, ApJ, 673, 864
- Kahn F. D., Woltjer L., 1959, ApJ, 130, 705
- Kalirai J. S. et al., 2010, ApJ, 711, 671
- Kalirai J. S. et al., 2006, ApJ, 648, 389
- Kalirai J. S. et al., 2009, ApJ, 705, 1043
- Kallivayalil N., Besla G., Sanderson R., Alcock C., 2009, ApJ, 700, 924
- Kaluzny J., Kubiak M., Szymanski M., Udalski A., Krzeminski W., Mateo M., 1995, A&AS, 112, 407
- Karachentsev I. D., Karachentseva V. E., Huchtmeier W. K., Makarov D. I., 2004, AJ, 127, 2031
- Karachentsev I. D., Kashibadze O. G., Makarov D. I., Tully R. B., 2009, MNRAS, 393, 1265
- Kauffmann G., White S. D. M., Guiderdoni B., 1993, MNRAS, 264, 201
- Keller S. C., da Costa G. S., Prior S. L., 2009, MNRAS, 394, 1045
- Keller S. C., Murphy S., Prior S., Da Costa G., Schmidt B., 2008, ApJ, 678, 851
- Kholopov P. N. et al., 1996, *VizieR Online Data Catalog*, 2139, 0
- Kilic M. et al., 2006, AJ, 131, 582
- King I., 1962, AJ, 67, 471
- Kinman T. D., Cacciari C., Bragaglia A., Buzzoni A., Spagna A., 2007, MNRAS, 375, 1381

Bibliography

- Kleyna J. T., Wilkinson M. I., Evans N. W., Gilmore G., 2004, MNRAS, 354, L66
- Klypin A., Gottlöber S., Kravtsov A. V., Khokhlov A. M., 1999, ApJ, 516, 530
- Klypin A., Kravtsov A. V., Valenzuela O., Prada F., 1999, ApJ, 522, 82
- Klypin A., Zhao H., Somerville R. S., 2002, ApJ, 573, 597
- Koch A., Kleyna J. T., Wilkinson M. I., Grebel E. K., Gilmore G. F., Evans N. W., Wyse R. F. G., Harbeck D. R., 2007, AJ, 134, 566
- Koch A., Wilkinson M. I., Kleyna J. T., Gilmore G. F., Grebel E. K., Mackey A. D., Evans N. W., Wyse R. F. G., 2007, ApJ, 657, 241
- Koch A. et al., 2009, ApJ, 690, 453
- Kochanek C. S., 1996, ApJ, 457, 228
- Kollmeier J. A. et al., 2009, ApJ, 705, L158
- Koposov S. et al., 2008, ApJ, 686, 279
- Kroeker T. L., Carlberg R. G., 1991, ApJ, 376, 1
- Kroupa P., Theis C., Boily C. M., 2005, A&A, 431, 517
- Kuijken K., Rich R. M., 2002, AJ, 124, 2054
- Kulesa A. S., Lynden-Bell D., 1992, MNRAS, 255, 105
- Lafler J., Kinman T. D., 1965, ApJS, 11, 216
- Larson D. et al., 2010, ArXiv e-prints
- Law D. R., Johnston K. V., Majewski S. R., 2005, ApJ, 619, 807
- Law D. R., Majewski S. R., Johnston K. V., 2009, ApJ, 703, L67
- Lee Y. S. et al., 2008, AJ, 136, 2022
- Letarte B. et al., 2009, MNRAS, 400, 1472
- Li Y., Helmi A., 2008, MNRAS, 385, 1365
- Li Y., White S. D. M., 2008, MNRAS, 384, 1459
- Little B., Tremaine S., 1987, ApJ, 320, 493
- Lupton R. H., Gunn J. E., Szalay A. S., 1999, AJ, 118, 1406
- Lynden-Bell D., 1982, The Observatory, 102, 202
- Lynden-Bell D., 1999, in P. Whitelock & R. Cannon ed., The Stellar Content of Local Group Galaxies Vol. 192 of IAU Symposium, Local Group Dynamics, pp 39–+
- Lynden-Bell D., Frenk C. S., 1981, The Observatory, 101, 200
- Lynden-Bell D., Lynden-Bell R. M., 1995, MNRAS, 275, 429

- Mackey A. D. et al., 2006, ApJ, 653, L105
- Madau P., 2007, ArXiv e-prints
- Majewski S. R., 1994, ApJ, 431, L17
- Majewski S. R. et al., 2007, ApJ, 670, L9
- Majewski S. R. et al., 2004, AJ, 128, 245
- Majewski S. R., Skrutskie M. F., Weinberg M. D., Ostheimer J. C., 2003, ApJ, 599, 1082
- Martin N. F., de Jong J. T. A., Rix H., 2008, ApJ, 684, 1075
- Martin N. F., Ibata R. A., Bellazzini M., Irwin M. J., Lewis G. F., Dehnen W., 2004, MNRAS, 348, 12
- Martin N. F., Ibata R. A., Chapman S. C., Irwin M., Lewis G. F., 2007, MNRAS, 380, 281
- Martin N. F., Ibata R. A., Irwin M. J., Chapman S., Lewis G. F., Ferguson A. M. N., Tanvir N., McConnachie A. W., 2006, MNRAS, 371, 1983
- Martin N. F. et al., 2009, ApJ, 705, 758
- Mateo M., Olszewski E. W., Pryor C., Welch D. L., Fischer P., 1993, AJ, 105, 510
- Mateo M. L., 1998, ARA&A, 36, 435
- Mateu C., Vivas A. K., Zinn R., Miller L. R., Abad C., 2009, AJ, 137, 4412
- McConnachie A. W. et al., 2008, ApJ, 688, 1009
- McConnachie A. W., Irwin M. J., 2006a, MNRAS, 365, 1263
- McConnachie A. W., Irwin M. J., 2006b, MNRAS, 365, 902
- McConnachie A. W., Irwin M. J., Ferguson A. M. N., Ibata R. A., Lewis G. F., Tanvir N., 2005, MNRAS, 356, 979
- McConnachie A. W. et al., 2009, Nature, 461, 66
- Miceli A. et al., 2008, ApJ, 678, 865
- Mishra R., 1985, MNRAS, 212, 163
- Monet D. G. et al., 2003, AJ, 125, 984
- Moody R., Schmidt B., Alcock C., Goldader J., Axelrod T., Cook K. H., Marshall S., 2003, Earth Moon and Planets, 92, 125
- Moore B., Ghigna S., Governato F., Lake G., Quinn T., Stadel J., Tozzi P., 1999, ApJ, 524, L19
- Moore B., Katz N., Lake G., 1996, ApJ, 457, 455
- Morgan S. M., Wahl J. N., Wieckhorst R. M., 2007, MNRAS, 374, 1421
- Morrison H. L. et al., 2009, ApJ, 694, 130
- Morrison H. L., Mateo M., Olszewski E. W., Harding P., Dohm-Palmer R. C., Freeman K. C., Norris J. E., Morita M., 2000, AJ, 119, 2254

Bibliography

- Munn J. A. et al., 2004, *AJ*, 127, 3034
- Navarro J. F., Frenk C. S., White S. D. M., 1996, *ApJ*, 462, 563
- Newberg H. J., Willett B. A., Yanny B., Xu Y., 2010, *ApJ*, 711, 32
- Newberg H. J. et al., 2002, *ApJ*, 569, 245
- Newberg H. J., Yanny B., Willett B. A., 2009, *ApJ*, 700, L61
- Nicastro F. et al., 2003, *Nature*, 421, 719
- Niederste-Ostholt M., Belokurov V., Evans N. W., Peñarrubia J., 2010, *ApJ*, 712, 516
- Odenkirchen M., Grebel E. K., Dehnen W., Rix H., Cudworth K. M., 2002, *AJ*, 124, 1497
- Ortolani S., Renzini A., Gilmozzi R., Marconi G., Barbu B., Bica E., Rich R. M., 1995, *Nature*, 377, 701
- Ostriker J. P., Steinhardt P., 2003, *Science*, 300, 1909
- Paczynski B., 2000, *PASP*, 112, 1281
- Paczynski B., 2001, in Banday A. J., Zaroubi S., Bartelmann M., eds, *Mining the Sky Massive Variability Searches: the Past, Present and Future*.pp 481–+
- Palma C., Majewski S. R., Johnston K. V., 2002, *ApJ*, 564, 736
- Peñarrubia J. et al., 2005, *ApJ*, 626, 128
- Peñarrubia J., Navarro J. F., McConnachie A. W., 2008, *ApJ*, 673, 226
- Perlmutter S. et al., The Supernova Cosmology Project 1999, *ApJ*, 517, 565
- Piatek S., Pryor C., Bristow P., Olszewski E. W., Harris H. C., Mateo M., Minniti D., Tinney C. G., 2005, *AJ*, 130, 95
- Piatek S., Pryor C., Bristow P., Olszewski E. W., Harris H. C., Mateo M., Minniti D., Tinney C. G., 2006, *AJ*, 131, 1445
- Piatek S., Pryor C., Bristow P., Olszewski E. W., Harris H. C., Mateo M., Minniti D., Tinney C. G., 2007, *AJ*, 133, 818
- Piatek S., Pryor C., Olszewski E. W., 2008, *AJ*, 135, 1024
- Piatek S. et al., 2002, *AJ*, 124, 3198
- Piatek S., Pryor C., Olszewski E. W., Harris H. C., Mateo M., Minniti D., Tinney C. G., 2003, *AJ*, 126, 2346
- Pickering E. C., 1901, *Astronomische Nachrichten*, 154, 423
- Pier J. R., Munn J. A., Hindsley R. B., Hennessy G. S., Kent S. M., Lupton R. H., Ivezić Ž., 2003, *AJ*, 125, 1559
- Press W. H., Flannery B. P., Teukolsky S. A., Vetterling W. T., 1989, *Numerical recipes in C. The art of scientific computing*
- Preston G. W., Shectman S. A., Beers T. C., 1991, *ApJ*, 375, 121
- Queloz D., Dubath P., Pasquini L., 1995, *A&A*, 300, 31
- Raychaudhury S., Lynden-Bell D., 1989, *MNRAS*, 240, 195

- Reid M. J. et al., 2009, ApJ, 700, 137
- Richardson J. C. et al., 2009, MNRAS, 396, 1842
- Robin A. C. et al., 2007, ApJS, 172, 545
- Rohlf K., Kreitschmann J., 1988, A&A, 201, 51
- Saha A., 1985, ApJ, 289, 310
- Sakai S., Madore B. F., Freedman W. L., 1999, ApJ, 511, 671
- Sales L. V. et al., 2008, MNRAS, 389, 1391
- Sales L. V., Navarro J. F., Abadi M. G., Steinmetz M., 2007, MNRAS, 379, 1475
- Sarajedini A., Jablonka P., 2005, AJ, 130, 1627
- Saviane I., Held E. V., Bertelli G., 2000, A&A, 355, 56
- Schmidt B. P. et al., 1998, ApJ, 507, 46
- Scholz R., Irwin M. J., 1994, in H. T. MacGillivray ed., Astronomy from Wide-Field Imaging Vol. 161 of IAU Symposium, Absolute Proper Motions of the Dwarf Spheroidal Galaxies in Draco and Ursa Minor. pp 535–+
- Schweitzer A. E., Cudworth K. M., Majewski S. R., Suntzeff N. B., 1995, AJ, 110, 2747
- Searle L., Zinn R., 1978, ApJ, 225, 357
- Seigar M. S., Barth A. J., Bullock J. S., 2008, MNRAS, 389, 1911
- Sesar B. et al., 2010, ApJ, 708, 717
- Sesar B. et al., 2007, AJ, 134, 2236
- Sesar B., Vivas A. K., Duffau S., Ivezić Ž., 2010, ApJ, 717, 133
- Simon J. D., Geha M., 2007, ApJ, 670, 313
- Skrutskie M. F. et al., 2006, AJ, 131, 1163
- Smith H. A., 1995, RR Lyrae stars
- Smith J. A. et al., 2002, AJ, 123, 2121
- Smith M. C. et al., 2009, MNRAS, 399, 1223
- Smith M. C., Wyn Evans N., An J. H., 2009, ApJ, 698, 1110
- Sohn S. T. et al., 2007, ApJ, 663, 960
- Sommer-Larsen J., Zhen C., 1990, MNRAS, 242, 10
- Spergel D. N. et al., 2007, ApJS, 170, 377
- Starkenburger E. et al., 2009, ApJ, 698, 567
- Stetson P. B., 1996, PASP, 108, 851

Bibliography

- Stoughton C. et al., 2002, AJ, 123, 485
- Strigari L. E., Bullock J. S., Kaplinghat M., Simon J. D., Geha M., Willman B., Walker M. G., 2008, Nature, 454, 1096
- Summers F. J., Davis M., Evrard A. E., 1995, ApJ, 454, 1
- Terndrup D. M., 1988, AJ, 96, 884
- Tolstoy E. et al., 2004, ApJ, 617, L119
- Trimble V., Aschwanden M. J., Hansen C. J., 2007, Space Science Reviews, 132, 1
- Tsikoudi V., 1979, ApJ, 234, 842
- Udalski A., Szymanski M., Kaluzny J., Kubiak M., Mateo M., 1992, Acta Astronomica, 42, 253
- van den Bergh S., 1998, AJ, 116, 1688
- van den Bergh S., 2006, AJ, 131, 304
- van den Bergh S., 2008, MNRAS, 385, L20
- van der Kruit P. C., Searle L., 1981, A&A, 95, 105
- van der Marel R. P., Alves D. R., Hardy E., Suntzeff N. B., 2002, AJ, 124, 2639
- van der Marel R. P., Guhathakurta P., 2008, ApJ, 678, 187
- Vidrih S. et al., 2007, MNRAS, 382, 515
- Vivas A. K., Jaffé Y. L., Zinn R., Winnick R., Duffau S., Mateu C., 2008, AJ, 136, 1645
- Vivas A. K., Zinn R., 2006, AJ, 132, 714
- Vivas A. K. et al., 2004, AJ, 127, 1158
- Vivas A. K., Zinn R., Gallart C., 2005, AJ, 129, 189
- Walker A. R., Terndrup D. M., 1991, ApJ, 378, 119
- Walker M. G., Mateo M., Olszewski E. W., 2008, ApJ, 688, L75
- Walker M. G., Mateo M., Olszewski E. W., Bernstein R., Wang X., Woodroffe M., 2006, AJ, 131, 2114
- Walker M. G., Mateo M., Olszewski E. W., Pal J. K., Sen B., Woodroffe M., 2006, ApJ, 642, L41
- Walker M. G., Mateo M., Olszewski E. W., Peñarrubia J., Wyn Evans N., Gilmore G., 2009, ApJ, 704, 1274
- Walsh S. M., Jerjen H., Willman B., 2007, ApJ, 662, L83
- Watkins L. L., Evans N. W., An J., 2010, ArXiv e-prints
- Watkins L. L. et al., 2009, MNRAS, 398, 1757
- Wetterer C. J., McGraw J. T., 1996, AJ, 112, 1046
- White S. D. M., 1976, MNRAS, 177, 717
- White S. D. M., 1981, MNRAS, 195, 1037

- White S. D. M., Rees M. J., 1978, MNRAS, 183, 341
- Wilkinson M. I., Evans N. W., 1999, MNRAS, 310, 645
- Willman B. et al., 2005, ApJ, 626, L85
- Wolf J., Martinez G. D., Bullock J. S., Kaplinghat M., Geha M., Muñoz R. R., Simon J. D., Avedo F. E., 2010, MNRAS, 406, 1220
- Xue X. X. et al., 2008, ApJ, 684, 1143
- Yanny B. et al., 2003, ApJ, 588, 824
- Yanny B. et al., 2009, ApJ, 700, 1282
- Yanny B. et al., 2000, ApJ, 540, 825
- York D. G. et al., 2000, AJ, 120, 1579
- Zaritsky D., Olszewski E. W., Schommer R. A., Peterson R. C., Aaronson M., 1989, ApJ, 345, 759
- Zinn R., 1993, in G. H. Smith & J. P. Brodie ed., The Globular Cluster-Galaxy Connection Vol. 48 of Astronomical Society of the Pacific Conference Series, The Galactic Halo Cluster Systems: Evidence for Accretion. pp 38–+
- Zucker D. B. et al., 2006, ApJ, 650, L41
- Zucker D. B. et al., 2006, ApJ, 643, L103
- Zucker D. B. et al., 2004, ApJ, 612, L121
- Zucker D. B. et al., 2007, ApJ, 659, L21
- Zwicky F., 1937, ApJ, 86, 217

Nomenclature

Constants

v_{LSR} velocity of the LSR, (0, 220, 0) km s^{-1}

v_{\odot} solar peculiar motion with respect to the LSR, $(+10 \pm 0.36, +5.25 \pm 0.62, +7.17 \pm 0.38)$ km s^{-1}
(Dehnen & Binney, 1998)

Acronyms

2MASS Two-Micron All-Sky Survey

And XII Andromeda XII dSph galaxy

And XIV Andromeda XIV dSph galaxy

BHB Blue horizontal branch

CFHT Canada-France-Hawaii Telescope

dE Dwarf elliptical galaxy

dIrr Dwarf irregular galaxy

dSph Dwarf spheroidal galaxy

EC Extended cluster

GC Globular cluster

GRF Galactic Rest Frame

HLC Higher level catalogue

HRF Heliocentric Rest Frame

HST Hubble Space Telescope

HVC High Velocity Cloud

ISM Interstellar medium

LG Local Group

LMC Large Magellanic cloud

Nomenclature

LMCC	Light-motion-curve catalogue
LSR	Local standard of rest
LSST	Large Synoptic Survey Telescope
M31	Andromeda galaxy
M33	Traingulum galaxy
MDF	Metallicity distribution function
MSTO	Main sequence turn off
MW	Milky Way
NCP	North Celestial Pole
NGP	North Galactic Pole
NIR	Near infrared
Pan-STARRS	Panoramic Survey Telescope And Rapid Response System
PAndAS	Pan-Andromeda Archaeological Survey
PN	Planetary Nebula
RRab	ab-type RR Lyrae
RRc	c-type RR Lyrae
SDSS	Sloan Digital Sky Survey
Sgr	Sagittarius dSph galaxy
SMC	Small Magellanic cloud
SPLASH	Spectroscopic and Photometric Landscape of Andromeda's Stellar Halo

List of Tables

2.1	The distribution of candidate variable sources in the $g - r$ versus $u - g$ diagram.	41
3.1	The means and dispersions in the properties of the RR Lyrae variables split according to RRab and RRc types.	53
3.2	Properties of the RR Lyraes associated with substructures.	57
4.1	Data table for the satellites of the MW.	76
4.2	Data table for the satellites of M31.	77
4.3	Enclosed mass within 100, 200 and 300 kpc for MW and M31.	78
4.4	Table of proper motion data for the satellites of the MW and M31.	82

List of Figures

1.1	Sgr stream from 2MASS.	12
1.2	The “field of streams”	13
1.3	The halos of M31 and M33 as mapped by PAndAS.	21
1.4	Absolute magnitude versus half-light radius for dSphs and GCs.	25
1.5	Mass-to-light ratios versus absolute magnitudes for a number of LG dSphs.	27
2.1	SDSS Stripe 82 coverage in Galactic coordinates.	34
2.2	Left: Cumulative distribution of mean object type in the HLC. Right: Cumulative distribution of reduced χ^2 for g and r bands for all stellar objects.	35
2.3	Density plot of reduced χ^2_g against Stetson index L_g for the stellar catalogue.	36
2.4	A sample of folded lightcurves.	37
2.5	g versus $u - g$ colour magnitude diagrams for the high-quality stellar sample and the variable sub-sample.	38
2.6	Reduced proper motions diagrams for the high-quality stellar sample and the variable sub-sample.	38
2.7	Colour-colour plots, colour coded to discriminate different classes of variable object.	40
2.8	Upper: number of variable objects versus right ascension. Lower: The spatial distribution of the variable subsample in Stripe 82.	41
3.1	Lomb-Scargle period estimates in the g and r bands for the candidate RR Lyraes.	46
3.2	Sample periodogram spectrum.	47
3.3	Distribution of periods for the RR Lyrae candidates.	48
3.4	Period versus the combined g and r band amplitudes.	49
3.5	The performance of the photometric metallicity relationships.	50
3.6	The RR Lyrae candidate selection boxes in the $u - g$ versus $g - r$ plane.	51
3.7	The spatial distribution of the ab-type and the c-type RR Lyraes.	54
3.8	Top: The fraction of Galactic volume probed by the RR Lyraes in Stripe 82 as function of Galactocentric distance. Bottom: The cumulative number of RR Lyraes within radius r in Stripe 82.	54
3.9	The distributions of distances and metallicities of RR Lyraes in the Hercules-Aquila Cloud, Sagittarius Stream and the Pisces Overdensity.	55
3.10	The number density of RR Lyraes in the plane of Galactic longitude versus r magnitude.	56
3.11	The density distributions of RR Lyrae candidates projected onto the principal planes of Galactocentric (x, y, z) coordinates.	57

List of Figures

3.12	Top: The distributions of main sequence turn-off stars in Stripe 82 shown in the plane of right ascension versus heliocentric distance. Middle: The velocity distribution of all stars with $g - i < 1$ with SDSS spectra. Bottom: As middle, with the distribution colour-coded according to metallicity.	59
3.13	The distributions of BHB and blue straggler stars in Stripe 82 shown in the plane of right ascension versus heliocentric distance.	60
4.1	Distribution of mass estimate as a fraction of the true mass for 1000 Monte Carlo realisations, assuming that parameters α , β and γ are known exactly.	71
4.2	The best-fit value of the potential power-law index α to an NFW potential.	73
4.3	Cumulative numbers of satellite $N(< r)$ for the MW and M31.	74
4.4	The sensitivity of the estimated mass on the anisotropy parameter β	75
4.5	The fractional contribution each satellite makes to the mean mass estimator for the MW and M31.	79
4.6	Distribution of velocity anisotropy obtained from simultaneous mass and velocity anisotropy fitting.	81
4.7	Distribution of mass estimates as a fraction of true mass for Monte Carlo simulations for which some satellites have proper motion data.	84
4.8	The fractional contribution each satellite with proper motions makes to the mean mass estimate for the MW.	84
5.1	And XII. Left panel: t as a function of η . Middle panel: The effect of τ on t versus η . Right panel: Contours of mass in plane of $\ln(\tau)$ and ξ	95
5.2	And XII. Left panel: apocenter, semi-major axis and pericenter as a function of η . Top right: Minimum mass estimate as a function of η . Middle right: orbital period P as a function of η . Bottom right: eccentricity as a function of η	96
5.3	Same as Figure 5.1 for And XIV.	97
5.4	Same as Figure 5.2 for And XIV.	97
5.5	Distribution of line-of-sight velocities from the Monte Carlo simulations.	99
5.6	Contours of mean separation (left) and ratio of And XII-like satellites to And XIV-like satellites (right) with changing a and e distributions.	100
5.7	Top left: Line-of-sight velocity distribution for the M31 population. Top-right and lower panels: the same for simulations of group infall.	101
5.8	Same as Figure 5.1 for Leo I.	102
5.9	Same as Figure 5.2 for Leo I.	103